Atomic-layer-deposited TiOx and TiOx:Nb as candidate electron-selective passivating contact materials for c-Si solar cells

Berghuis, Willem-Jan H.

Award date:
2018

Technische Universiteit
Eindhoven
University of Technology

Atomic-layer-deposited TiO_x and TiO_x:Nb as candidate electron-selective passivating contact materials for c-Si solar cells

W.J.H. Berghuis

Eindhoven University of Technology (TUe),
Department of Applied Physics,
Plasma and Materials Processing

Supervised by:
Dr.ir. J. (Jimmy) Melskens (TUe)
Prof.dr.ir. W.M.M. (Erwin) Kessels (TUe)

Eindhoven, 26-1-2018

Abstract

To increase the efficiency of crystalline silicon solar cells it is crucial to reduce the recombination losses at the contacts. A new and promising way to reduce these losses are passivating contacts with metal oxides like titanium oxide (TiO_x). A passivating contact should provide a high level of c-Si surface passivation (assessed by the surface recombination velocity ($S_{eff,max}$)) and a low contact resistivity (ρ_c). In this work, the important factors and mechanisms for these two parameters are investigated for a few nanometers of atomic-layer-deposited (ALD) TiO_x. Secondly, doping of TiO_x with niobium (Nb) by ALD has been developed and explored as a new route to improve the c-Si surface passivation and ρ_c.

It is found from an extensive set of experiments that the c-Si surface passivation by 3-5 nm TiO_x is a combination of chemical passivation and field-effect passivation. The latter is originating from a large induced upward band bending in c-Si(n). A post-deposition forming gas anneal proves to be essential to activate the chemical passivation and achieve the high level of passivation ($S_{eff,max}$ as low as 10.7 cm/s). The Si surface treatment prior to ALD of TiO_x is another key factor for the passivation: a so called RCA-clean provides significantly better passivation than nitric acid oxidation of silicon (NAOS), while the passivation of hydrofluoric acid (HF) cleaned silicon depends strongly on the ALD temperature. Rectifying contact behavior is found to increase for thicker TiO_x layers and higher ALD temperatures, leading to a high ρ_c. The origin of this behavior is thought to originate from increased upward band bending in the c-Si(n). A post-deposition forming gas anneal turned also out to be key in transforming this rectifying behavior to low Ohmic behavior ($\rho_c \leq 10^{-2}$ Ω·cm^2).

Controlled Nb doping of TiO_x by ALD has been achieved by alternating cycles TiO_x with NbO_x cycles in a supercycle fashion. The Nb doping in 30 nm thick TiO_x:Nb films is activated during a 300 °C forming gas anneal. This activation is attributed to the phase transition from amorphous to crystalline anatase TiO_x upon annealing. By increasing the Nb-fraction (NbF_{XPS}) from NbF_{XPS} = 0 to NbF_{XPS} = 0.067, a change in resistivity (ρ) and electron concentration (n_e) of $\rho \approx 1{\cdot}10^{-1}$ to $9{\cdot}10^{-3}$ Ω·cm and $n_e = 9{\cdot}10^{19}$ to $1.0{\cdot}10^{21}$ cm^{-3} is achieved, respectively. Preliminary results have shown that the passivation of 1-5 nm of TiO_x:Nb is not affected by the doping, while the contact resistivity increases with doping. The latter unexpected behavior is attributed to the high resistive and persisting amorphous character of the 1-5 nm thick TiO_x:Nb layers compared to the 30 nm thick layers. For future work, it would be promising to investigate thicker crystalline anatase TiO_x:Nb films or to attempt to crystallize 1-5 nm films by applying higher anneal temperatures.

Contents

Chapter 1

General introduction

1.1 Passivating contacts with metal oxides for crystalline silicon solar cells

One of today´s big challenges is the replacement of fossil energy sources with alternative energy sources. These new energy sources should provide future generations with sufficient energy without contributing to global warming and environmental damage. A sustainable way to produce electricity is by using solar cells (photovoltaic cells). The contribution of this energy source in the world wide energy production is rising [1],[2]. Regarding the current technological developments, investments [3] and application possibilities (installations on roofs, roads, deserts), it can be concluded that solar cells have a very high potential as sustainable energy source. The current generation commercial solar cell modules has an average efficiency of about 16 to 17 % [4], while the maximum theoretical efficiency for crystalline silicon (c-Si) solar cells is 29.4 % [5]. There are multiple reasons for the efficiency gap between this theoretical efficiency limit and the current generation solar cells, but one of the most important reasons is recombination losses of generated electron-hole pairs at the contacts. The rear contact structure of conventional c-Si solar cells is realized by a screen-printed aluminum metallization. This approach leads to a doped region of Si near the aluminum and direct contact of the silicon and aluminum. The direct contact of aluminum with the c-Si introduces a nearly continuous range of energy states in the bandgap of the c-Si at the c-Si/ aluminum interface. Energy states in the bandgap and especially those near the middle of the bandgap are notorious recombination sites for electron-hole pairs [6]. Furthermore, the doped Si region has a high carrier concentrations, which leads to a significant recombination by multi-particle recombination processes, also known as Auger recombination.

In the quest for higher solar cell conversion efficiencies, two different strategies can be distinguished to reduce these recombination losses at the contacts: lowering the metal contact area (strategy 1) or separation of the silicon and metal by a carrier-selective passivating layer (strategy 2). A combination of both strategies is also possible. The first strategy involves cells in which the silicon surface is largely covered with a passivating layer (with relatively low recombination losses per area) and only partly with the highly recombinative metal contacts (which still have a high recombination per area). Although the fundamental problem of the recombination at the silicon-metal interface is not solved in this way, the total recombination losses per area are reduced and hence better cell performance can be achieved. There are different cell designs using this principle including the *Passivated Emitter and Rear Cell* (PERC), *Passivated Emitter Rear Totally diffused* (PERT) and the *Passivated Emitter with Rear Locally diffused* (PERL) (see Figure 1.1). The latter reaches efficiencies of nearly 25% [7] on small lab-scale solar cells, while industrial large-area n-PERT cells

have already reached an efficiency of 23.45% [8]. This strategy clearly enables high conversion energies, but reducing the metal contact area involves a smaller current path for the extracted current, which means a higher resistance and hence higher Ohmic losses. The latter implies that there is a fundamental trade-off between reduced electron-hole recombination at the silicon surface and contact resistivity, limiting further improvements. This is not the case for the second strategy: inserting a carrier-selective passivating layer between the metal contact and the silicon. Such an interlayer consist of a material (stack) that reduces the recombination of electrons and holes and preferably also provides carrier selectivity. This reduction of recombination of electrons and holes at the silicon surface is referred to as *surface passivation* in the field of solar cells. An example of a carrier-selective passivating layer is a thin layer of n- or p-type hydrogenated amorphous silicon (a-Si:H) on top of a thin layer of intrinsic hydrogenated amorphous silicon (i a-Si:H) (see Figure 1.2). The intrinsic layer provides the passivation and the n- or p-type a-Si:H provides carrier selectivity. This stack is used in the current efficiency record for a practical size crystalline silicon PV cell, which reached an efficiency of 26.6 % in 2016[9]. Hydrogenated amorphous silicon is a very successful contact material, but not the only material option. A second type of material used as (carrier-selective-)passivating layer is n- or p-type poly crystalline silicon (poly-Si). Between the n- or p-type poly crystalline silicon and the silicon wafer, a silicon oxide layer is necessary to enable the carrier-selective-passivating properties of the material. The combination with a silicon oxide interlayer is used in cells reaching efficiencies up to 25.7% [8].

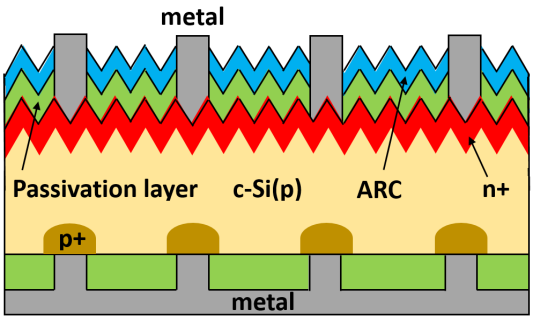

Figure 1.1: Example of a schematic representation of a Passivated Emitter with Rear Locally diffused solar cell (PERL). This is an example of reduced recombination losses by strategy 1. (ARC stands for antireflective coating)

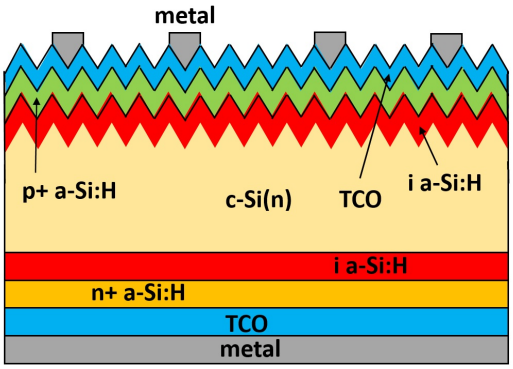

Figure 1.2: Example of a schematic representation of a typical a-Si:H heterojunction solar cell. This is an example of reduced recombination losses by strategy 2. (TCO stands for Transparent Conductive Oxide)

Both a-Si:H and poly-Si (in combination with SiO_x) provide excellent passivation and low contact resistivity leading to high cell efficiencies, but cells based on these materials suffer from optical losses. Additionally, a-Si:H is thermally not very stable, limiting processing temperatures to approximately 200 °C [10]. Since the parasitic absorption losses of the above-mentioned materials is becoming an important limiting factor, a third material class option for a carrier-selective passivating layer is attracting more attention: metal oxides. Metal oxides provide a more transparent material option due to their high bandgaps, thereby reducing the absorption losses associated with a-Si:H and poly-Si. The relatively simple and potentially inexpensive processing of metal oxide layers is another asset for this type of material. In the last years, multiple metal oxides (mainly deposited by atomic layer deposition (ALD)) have proven their potential by providing impressive

cell efficiencies. Solar cells with molybdenum oxide (MoO_x) as hole-selective contact have reached efficiencies up to 22.5% [11] and ALD titanium oxide (TiO_x) as electron-selective contact resulted in cell efficiencies up to 22.1% [12]. To fully exploit the transparent properties of metal oxides like TiO_x and boost cell efficiencies, the contact resistivity and the passivation should approach the same levels as materials like a-Si:H and poly-Si. The latter is the main challenge for metal oxides like TiO_x and will be key to their future success in enabling higher solar cell efficiency.

1.2 Atomic layer deposition for passivating contacts in c-Si solar cells

Atomic layer deposition (ALD) is a material deposition technique that enables the deposition of ultrathin layers of material. A key feature of ALD is sub-nanometer thickness control, which enables the deposition of ultrathin layers which are typically only a few nanometers thick. The technique has furthermore the advantage of high uniformity over large areas and complex 3D structures. This means that the film properties and film thickness show relatively small variations over the area ($< 2.5\%$ thickness variation for a 200 nm thick film [13]) or 3D structures ($< 5\%$ variation of the film thickness in trench structures [13]). The temperature at which the ALD process can take place can be lower than 100 °C [14], which allows processing of temperature sensitive structures. These features of ALD make it an excellent deposition technique for passivating contact materials in c-Si solar cells. A well-known example that demonstrates the suitability of ALD is the excellent c-Si surface passivation provided by a few nanometers ALD Al_2O_3 [15].

1.3 Research goals and outline of the work

In the previous sections it is explained that metal oxides can be an interesting candidate as carrier-selective passivating contact material. A relatively new electron-selective metal oxide for passivating contacts is TiO_x deposited with ALD [16], [17]. For a passivating contact both the provided c-Si surface passivation and the contact resistivity are important. Currently there are several studies showing experimental results for the passivating qualities and contact resistivity of TiO_x [18], [19], [20], [21], [17] . Furthermore some good solar cell results have been achieved with a record efficiency of 22.1% by Yang et al. in 2017 [12]. A more profound understanding of TiO_x as passivating contact is however still limited. The first aim of this work is therefore to improve understanding of TiO_x by identifying the important factors and mechanism for the c-Si surface passivation and contact resistivity of ALD TiO_x .

In the field of semiconductors and solar cells, it is well known that controlled doping of a material enables a certain degree of control over the material's work function and thereby control and improvement over several of its electrical properties [6]. Extrinsically doped TiO_x can therefore be a very promising material as electron-selective passivating contact for c-Si solar cells. However, until now only undoped TiO_x has been investigated for this application. The second aim of this work is to develop and investigation ALD niobium-doped TiO_x as new tunable electron-selective passivating contact material.

In short, the research goals of this work are:

1) Identifying the important factors and mechanism for the c-Si surface passivation and contact resistivity of ALD TiO_x

2) Development and investigation of ALD TiO_x:Nb as new tunable electron-selective passivating contact material

The report structure adopted to address these research goals consists of five chapters. The chapter following this introduction covers the necessary basics to understand the presented work. Next is a literature review of TiO_x. This chapter discusses what is already known about the passivation and contact resistivity of TiO_x and what is still unclear and needs to be investigated. The unaddressed TiO_x topics pointed out in the literature review serve as a base for the experimental research, which is presented in chapter 4. At the end of chapter 4, there is a conclusion which addresses the first research goal. Chapter 5 focuses on the second goal of this work: the development and investigation of niobium-doped titanium oxide. A general conclusion with recommendations for future work is provided in the last chapter.

Chapter 2

Basics of passivating contacts

2.1 Working principle of a c-Si solar cells with passivating contacts

This section explains the basic working principle of carrier-selective passivating contacts in c-Si solar cells. The solar cell structure of Figure 2.1 will be used for this discussion.

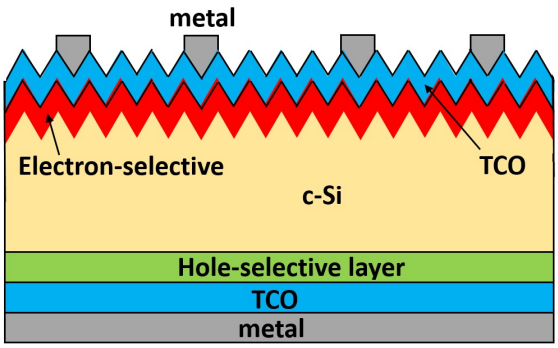

Figure 2.1: Schematic representation of a solar cell configuration in which metal oxides can be used for the carrier-selective layers. Note that there are multiple other configurations possible in which classical techniques (heavily doped regions) and new techniques (passivating contacts) are combined (see for example [12] and [19]).

The core of the solar cell consists of a 200 to 500 μm thick silicon wafer (n-type or p-type). In this wafer, electron-hole pairs are created by the incident light. In order to create an electrical power source, the holes and electrons need to be separated from each other. This task is performed by the carrier-selective passivating layers, present on both sides of the silicon wafer (see Figure 2.1). One of the layers, the electron-selective layer, has a very high conductivity for electrons and a high resistivity for holes. The electrons can therefore easily pass this layer and accumulate at the metal contact to form the negative contact of the solar cell. Possible materials for this layer are for example n-type amorphous silicon (a-Si:H(n)), n-type poly silicon (poly-Si(n)) and certain metal

oxides like TiO_x. The other layer, the hole-selective layer, has a high conductivity for holes and high resistivity for electrons, thereby forming a positive contact at the other side of the solar cell. Possible materials for this layer include a-Si:H(p), poly-Si(p) and certain metal oxides like MoO_x. Recombination of electrons and holes in the solar cells must be prevented since every electron that recombines can not flow through the external load to perform work. A very important source of recombination are the defects at the surface of the silicon wafer. The carrier-selective layers have therefore a second task: reducing this recombination. The latter is referred to as passivation.

Between the carrier-selective layer at the front of the solar cell and the metal contact grid, a transparent conductive layer is found. Due to the relatively high conductivity of this layer compared to the often very thin and resistive carrier-selective layer, the transparent conductive layer provides the necessary lateral conduction from the carrier-selective layer to the fingers of the metal grid. The second funtion of the transparent conductive layer is to increase the amount of light that enters the silicon wafer by acting as an anti-reflection coating. Commonly used materials for this layer include doped zinc oxide and indium tin oxide. These kind of materials are often referred to as transparent conductive oxides (TCOs). In the ideal case, a similar structure is found at the rear side. However, with regard to the manufacturing and costs of the solar cell, a more simple configuration is often chosen: a fully metallized rear.

2.2 Requirements for a carrier-selective passivating layer

An important requirement for a carrier-selective passivating layer is passivation. Since charge carriers recombine mainly at the surface, there is a diffusion driven flow of these charge carriers to this surface: the recombination current J_0 ($fAcm^{-2}$). This recombination current is a measure for the surface passivation and should be as low as possible. The first requirement for the carrier-selective passivating layer is thus a low J_0. When the conductivity for electrons and holes is insufficiently asymmetric in the carrier-selective layer, a substantial amount of both carrier type reaches the metal and the recombination losses (J_0) increase significantly. The recombination current after metallization does therefore not only contain information about the passivation level, but also about the carrier-selectivity of the layer.

The carrier selectivity depends only on the ratio of conductivity that electrons and holes experience. However, the absolute values of the conductivity are also important. The conductivity for electrons in the electron-selective layer for example should be as high as possible, since no electrical power should be dissipated . The latter is not covered by a conductivity ratio. A second parameter is therefore needed to determine the effect of the carrier-selective passivating contact on the efficiency of the solar cell: the contact resistivity $\rho_{contact}$ ($\Omega \cdot cm^2$) (or ρ_c) . This is the resistivity the current experiences flowing from the silicon to the metal contact. Both the recombination current J_0 and the contact resistivity ρ_c together determine the quality of the carrier-selective contact [10]. The effect of both parameters on the efficiency can be seen in Figure 2.2 [10]. This plot shows the maximal theoretical efficiency for a solar cell with one perfectly lossless front and one carrier-selective passivating rear contact defined by J_0 and $\rho_{contact}$. Note that for values of the contact resistivity $\rho_{contact}$ below 0.1 $\Omega \cdot cm^2$, the efficiciency gain becomes very small.

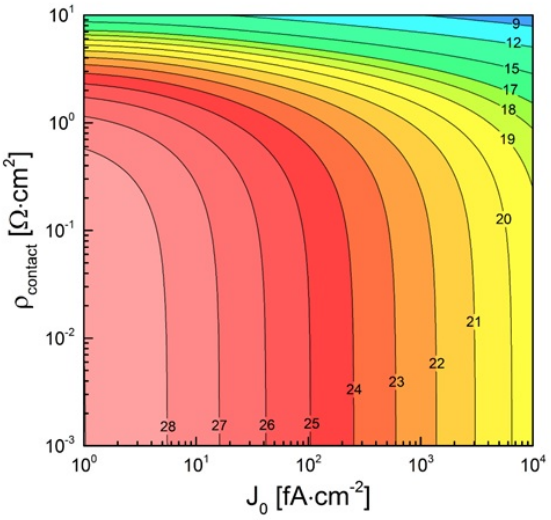

Figure 2.2: This figure shows the maximal theoretical efficiency for a solar cell with an ideal front contact and a carrier-selective passivating rear contact defined by J_0 and $\rho_{contact}$. The corresponding maximum conversion efficiency is indicated by iso-efficiency lines. The figure is the result of a simulation with Quokka software [10].

When the carrier-selective layer is applied at the front side of the solar cell, two additional rewuirements arise. First of all, the layer has to be transparent. Transparency can be assessed by the extinction coefficient k (a.u.) of the layer, which is a measure for the attenuation of an electromagnetic wave when it travels through a material. Secondly, the refractive index of this layer has preferably a value between the refractive index of the anti-reflecting coating and refractive index of the silicon wafer in order to minimize optical reflection losses.

In short, the requirements for a carrier-selective passivating layer in a highly efficient solar cell are:

1) A low recombination current J_0 (fAcm^{-2})

2) A low contact resistivity $\rho_{contact}$ (Ω·cm^2)

3) A low extinction coefficient k (a.u.)

2.3 Crystalline silicon surface passivation

As explained in the previous section, each electron-hole pair that is generated by the incident light and recombines before it is extracted to the solar cell's contacts, is a loss of charge that could have potentially flown through an external load to perform work. This section explains the role of the surface in the recombination of electron-hole pairs. Furthermore, two strategies will be discussed to reduce these recombination losses; i.e. provide surface passivation.

Defect states with energies in the bandgap of the silicon are very effective recombination centers for electrons and holes [6]. At the surface of a crystalline silicon lattice, unsatisfied covalent silicon bonds (silicon dangling bonds) and adsorbed impurity molecules (like oxygen and water), create a large concentration of these energy states (see Figure 5.34). The silicon surface is therefore a very effective recombination site for electron-hole pairs[6]. Reduction of this surface recombination is therefore vital to decrease the loss of electron-hole pairs and achieve high-efficiency solar cells [15].

There are essentially two ways to decrease the recombination losses at silicon surface [15]. The first way is to decrease the number of defects at the silicon surface (energy states in the silicon bandgap). This strategy is referred to as chemical passivation. The second way is to establish a strong reduction of either the hole or electron concentration at the c-Si surface. In this way there are too few electrons or holes at the c-Si surface for effective recombination of both. This strategy is called field-effect passivation. The following part will discuss these mechanisms in some more detail.

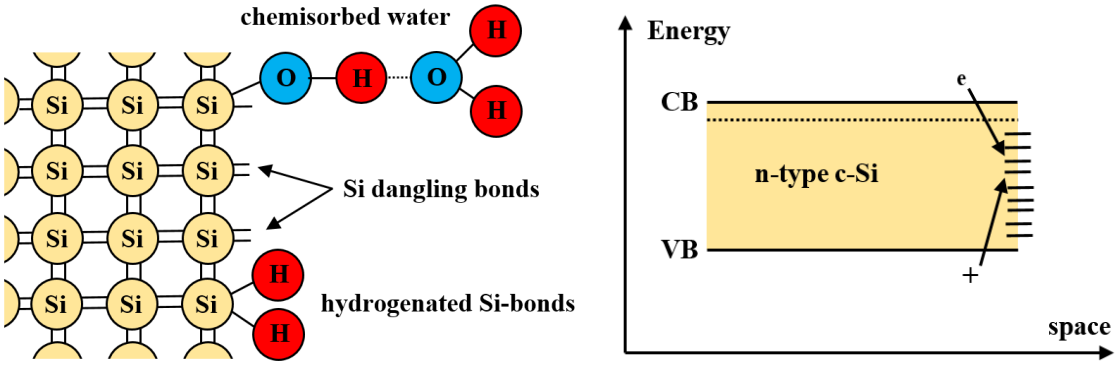

Figure 2.3: Left: schematic representation of the silicon lattice. Silicon dangling bonds and adsorbed impurity molecules (like oxygen and water) at the surface form energy states in the bandgap of silicon, which form effective recombination centers. The latter can be seen in the figure on the right, which represents the energy-space diagram of the c-Si lattice. CB and VB stand for the conduction and valence band respectively. The Fermi-level is indicated by the dashed line, electrons by e and holes by $+$. Defect states from Si-dangling bonds can be neutralized by bonding them to hydrogen. This is shown by two hydrogenated Si-bonds in the figure on the left.

Chemical passivation can be achieved by capping the c-Si surface with a material that establishes a low level of defect states at the silicon interface and that exhibits low or asymmetric conductivity for electrons and holes. The first requirement ensures a low recombination at the silicon/capping interface and the second requirement prevents a flow of both electrons and holes to the surface of

the cover layer, where effective recombination can still take place. To establish a low defect density at the silicon surface, hydrogen plays an important role. Hydrogen can bond to silicon dangling bonds and thereby neutralize these effective recombination centers. This mechanism, referred to as hydrogenation [22], is demonstrated by Figures 5.34 and 2.4. The hydrogen for hydrogenation can come from hydrogen contained in the cover layer itself, but can also diffuse in the cover layer from an additional capping layer (that contains hydrogen) or from an ambient containing hydrogen. For hydrogenation energy is required, which is provided in a thermal way by subjecting the silicon with capping layer to a heat treatment. Such a treatment is called annealing. A low conductivity of the capping material corresponds to a Fermi-level in the middle of the bandgap. Asymmetric conductivity can be achieved by a Fermi-level that is close to either the conduction band or valence band of the capping material (e.g. a strongly doped semiconductor like doped a-Si:H).

Field-effect passivation can be established in several ways including the presence of a relatively high or low work function material near the silicon surface (a capping material like highly doped ZnO or highly doped a-Si:H), heavy doping of the silicon near the surface or by fixed charge in the adjacent capping layer (e.g. Al_2O_3). Field effect passivation, which is illustrated by band bending, is depicted by number 1 in Figure 2.4.

Note that the passivation provided by a material does not have to be governed only by one of these mechanisms, but can also be determined by a combination of both mechanisms (e.g. doped a-Si:H and Al_2O_3).

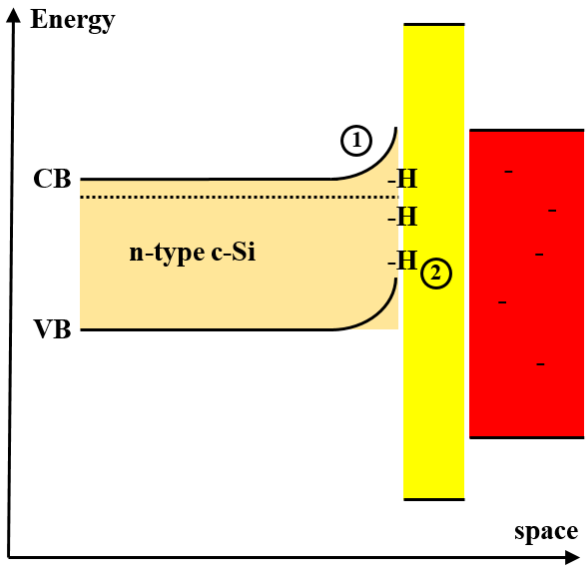

Figure 2.4: Band diagram of a c-Si lattice passivated by a high bandgap material capped with a material containing negative fixed charge. Both chemical passivation (2) and field-effect passivation (1) are indicated.

2.4 Contact resistivity

In a solar cell, electrons and holes are collected at two different electrodes to create an electrical power source. Extraction of the carriers from the silicon to the electrode should cost little to no energy to keep the solar cell efficiency high. A measure for the energy loss of the carrier extraction is the contact resistivity. More specifically, the contact resistivity ρ_c as used in this work, is the resistance that carriers experience when flowing from the silicon to the metal contact. The contact resistivity can involve multiple contributions. Considering the case of the contact resistivity for a c-Si/interlayer/metal stack (see Figure 2.5), the contact resistivity involves a contribution of the resistance of both the Si/interlayer (R_1) and interlayer/metal interface (R_3) plus the bulk resistivity of the interlayer (R_2).

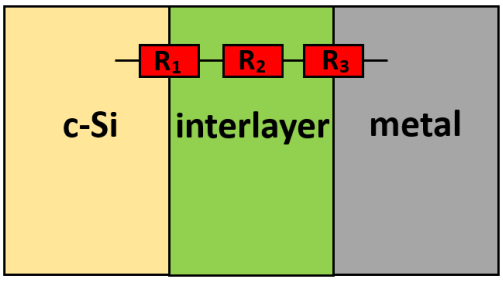

Figure 2.5: Schematic representation of a c-Si/interlayer/metal stack. The contact resistivity, i.e. the resistance the current experiences flowing from the c-Si to the metal contact, is indicated by R_1, R_2 and R_3.

To understand the resistance that can arise at the interface of two materials, one needs to know that resistivity ρ is inversely proportional to the conductivity σ and that conductivity equals the product of the carrier concentration n, carrier mobility μ, and elementary charge e:

$$\rho = \frac{1}{\sigma} = \frac{1}{e \cdot \mu \cdot n}. \tag{2.1}$$

The first reason for the resistance experienced by the current at a material interface, is caused by a local depletion of the free carriers near that interface. As a consequence of the need for electrochemical equilibrium between two materials (alignment of the Fermi levels), significant band bending in the materials can take place near the interface. The consequences of the band bending will be further explained using an interface with n-type silicon as example. For n-type silicon, the Fermi level is positioned in the upper half of the bandgap and the majority carriers are electrons (see the dashed line in Figure 2.6). Downward band bending of the conduction and valence band will result in a smaller energetic distance between the conduction band energy level and the Fermi level, meaning a higher electron concentration. From Equation 2.1, it is clear that a higher carrier concentration n near the interface means an enhanced conductivity in the silicon near the interface compared to the bulk (see Figure 2.6a). For such an interface, no additional resistance is expected. Since this region has a relatively low resistivity compared to the other parts of the stack near the interface, the relative voltage drop over this region is very small and the band bending of such a contact is therefore expected to be unaffected by the applied voltage. The expected behavior is

therefore expected to be linear and symmetric as a function of the applied voltage (Ohmic behavior). This behavior is illustrated by curve a in Figure 2.7. Upward band bending will however result in the opposite: depletion of the electrons near the interface. The latter implies reduced conductivity in the n-type silicon near the interface compared to the bulk and hence an additional resistance (see Figure 2.6b). Assuming that the interlayer provides a similar resistance as the silicon bulk, this depletion region has a relatively high resistance compared to the interlayer and bulk. This means that a significant part of an applied voltage over the c-Si/interlayer stack will be over this depletion region, affecting the band bending in the region. If a so-called forward voltage bias is applied, the n-type silicon is connected to the negative terminal of the power source and the metal to the positive one. With forward bias, the band bending can be reduced and hence the carrier concentration and therefore conduction of the silicon near the interface is increased. At the moment that the upward band bending is neutralized, the conductivity rapidly increases, visible as a sudden increase in the steepness of curve b in Figure 2.7. Note however that although the resistivity becomes low, there is a voltage drop over the interface to establish this low resistivity. A voltage drop means a direct loss of the electron energy, hence the voltage of the solar cell. For the case that a reverse bias voltage is applied, more carrier depletion near the interface take place, decreasing the conductivity. It may be clear from curve b in Figure 2.7 that an interface like this shows asymmetric and non-linear behavior with the applied voltage; this type of behavior is often referred to as rectifying. For n-type silicon downward band bending near the silicon interface (Ohmic contact behaviour) is desired to have carrier extraction without energy loss.

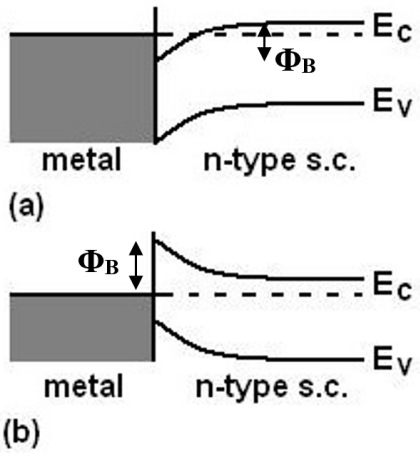

Figure 2.6: Schematic representation of band bending at a metal-semiconductor interface. Φ_B the is the energy barrier height, a measure for the resistance of the interface. Adapted from [23].

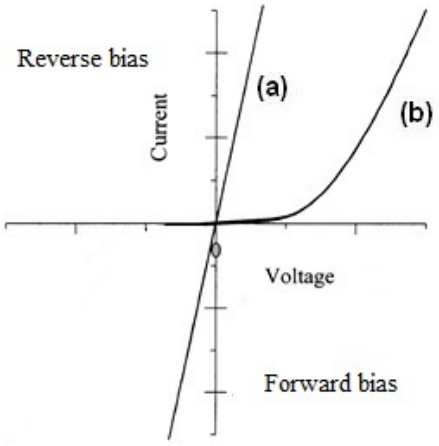

Figure 2.7: I-V curves for an Ohmic contact (a) and for a rectifying contact (b). Adapted from [24].

A second reason for resistance to arise at a semiconductor-metal interface is an energy offset between the conduction band of the semiconductor and the work function of the metal. The electrons that pass the interface must overcome this energy barrier: the current experiences resistance. Both the height of the band bending and the offset between the conduction band and metal work function form the total energy barrier electrons experience; i.e. a key metric for the interface resistance. The simplest model to estimate this energy barrier height Φ_B is the Schottky-Mott rule [6]:

$$\Phi_B = \Phi_M - \chi_{SC}, \tag{2.2}$$

where is Φ_B the barrier height (see Figure 2.6), Φ_M is the work function of the metal and χ_{SC} the electron affinity of the semiconductor. A metal work function lower than the electron affinity of the semiconductor induces downward band bending and hence an Ohmic contact can be established. The reality proves however to be more complex and a metal interface with n-type silicon often results in upward band bending (rule of thumb: the band bending is 2/3 of the bandgap for n-type semiconductors [25]) and the dependence on the metal work function is much smaller ($\sim$0.3) than predicted by the Schottky-Mott rule ($\sim$1) [26]. The result is rectifying contact behavior instead of Ohmic behaviour. This phenomenon is referred to as Fermi level pinning. Multiple theories have been proposed to explain this behavior. One explanation that is often used, is that the decaying tails of the wave functions of the metal atoms penetrate the semiconductor and introduce metal induced gap states (MIGS) in the bandgap of the semiconductor [27]. Occupation of these states introduces charge at the interface leading to band bending in the silicon. To reduce Fermi level pinning, the wave functions should decay before they enter the silicon. This can be established by physically separating the silicon from the metal by an interlayer. The required thickness of this interlayer is in the order of a few nanometers and depends on the material properties. The Fermi level de-pinning is more efficient for interlayer materials with a high bandgap and high lattice constant [28]. The requirement of a high lattice constant applies of course only for crystalline materials. Once the Fermi level is de-pinned, the barrier height Φ_B is no longer dominated by the MIGS, but by the difference in the metal work function Φ_M and the electron affinity of the semiconductor χ_{SC} [28] as the Schottky-Mott rule describes.

For a semiconductor-semiconductor interface, a second reason for resistance at the interface is an offset between the conduction bands. This is offset ΔE_C is predicted by Anderson's rule [29]:

$$\Delta E_C = \chi_{SC1} - \chi_{SC2}, \tag{2.3}$$

where χ_{SC1} and χ_{SC2} are the electron affinities of the two semiconductors forming the interface.

The conduction of the interlayer (in a silicon-interlayer-metal stack) can occur by movement of electrons in the conduction band and holes in the valence band, just like the conduction mechanism in metals and semiconductors. If the used interlayer concerns an insulator type of material (often an oxide), this mechanism results however in very low conductivity and a very high resistance is expected. The current-voltage characteristic for a thin oxide layer with a conduction band offset of E_B can be described by Schottky emission. In this mechanism thermal energy is used to excite the electron in the conduction band of the interlayer and there it is consequently propelled by the electric field (see Figure 2.8). For a few nanometer thick insulating layers, current can however also be established by tunneling (see Figure 2.8). This tunneling current has a strong dependence on both the barrier height (mainly the offset between the conduction band of the silicon and the interlayer) and the width of the interlayer. Tunneling through the insulator can occur in one step (direct tunneling) or in multiple steps (via defects states for example). The latter is called indirect or Poole-Frenkel (PF) tunneling [30].

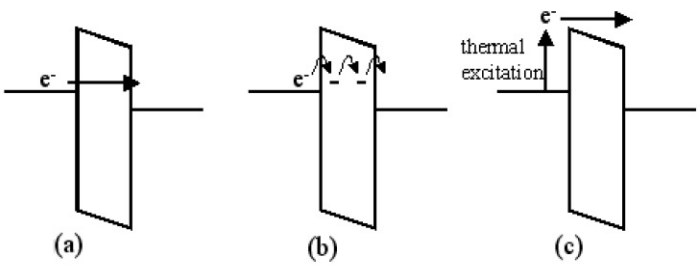

Figure 2.8: Current through an insulator by direct (PF) tunneling (a), indirect (PF) tunneling (b) and Schottky emission (c). [30]

Chapter 3

Basics of atomic layer deposition

3.1 Growth of ultrathin layers by atomic layer deposition

ALD materials are grown by a repeating cycle in which a sub-monolayer of material is deposited by exposing the surface to various vapor gas-phase species in alternating, separated doses [14]. A schematic overview of an ALD process is given in Figure 3.1. A typical cycle consists of the dosing of a precursor, a molecule that is made up of a metal center surrounded by chemical functional groups called ligands. During the dosing step, the precursor adsorbs at the surface. The dosing of the precursor takes place until saturation is reached, which means that no more adsorption can take place. This process is therefore self-limiting. In Figure 3.1 this step is schematically shown in the top left figure: 1st Half-cycle. The second step is removing the unadsorbed precursor that is still present in the reactor chamber; this step is called the purge step (see top right image in Figure 3.1). A third step involves dosing of a molecule called the co-reactant which reacts with the ligands of the adsorbed precursor. The reaction of the co-reactant molecule (which is often a small molecule like water or oxygen) with the ligands adds a second component to the film (where required) and reforms the original surface group [14] which enables the adsorption of new precursor molecules at the start of the next cycle. The reaction ends when all absorbed precursor has reacted with the co-reactant. This process is therefore also self-limiting. In Figure 3.1 this step is illustrated by the 2nd half-cycle. The ALD cycle ends with a removal of the co-reactant. This last purge step is illustrated in the bottom right image of Figure 3.1. A repetition of many cycles leads to the growth of a film, which is very controlled due to the self-limiting character of the reactions involved.

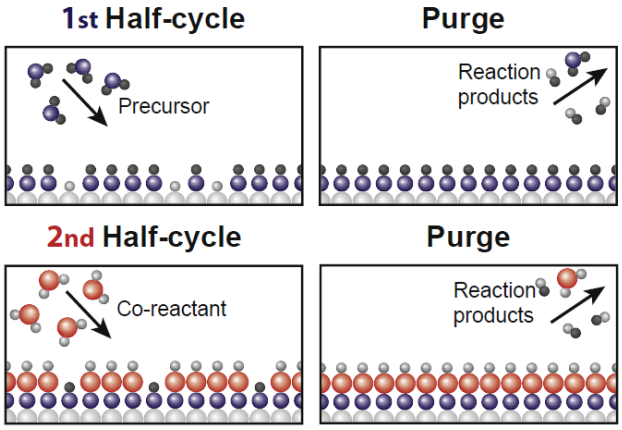

Figure 3.1: Schematic representation of an ALD cycle [14].

Chapter 4

A literature overview of titanium oxide

In the last few years, multiple studies have appeared about ALD TiO_x in the context of passivating contacts for c-Si solar cells. These studies focus mainly on presenting solar cell performance and experimental results of the passivating qualities, contact resistivity. An overview and more profound understanding of the factors that are important for the passivation and contact resistivity of a passivating contact based on TiO_x is however limited. Especially the effect and understanding of those factors related to the TiO_x material properties is not completely clear yet. The goal of this literature review is to establish a better understanding of TiO_x as electron-selective passivating contact material. For this purpose an overview of the factors that are important for the c-Si surface passivation and contact resistivity is provided. Furhermore, unaddressed issues and topics in literature with regard to the passivation and contact resistivity are pointed out.

This chapter is divided in two parts. The first part focuses on the TiO_x material properties and challenges that are important for the c-Si surface passivation while the second part focuses on the contact resistivity.

4.1 Surface passivation

An overview of reported c-Si passivation schemes with TiO_x can be found in Table 4.1. As measure for the passivation level, the effective surface recombination velocity ($S_{eff,max}$) is chosen. As mentioned in the beginning of this chapter, the key factors and TiO_x material properties associated with the reported effective surface recombination velocity values are discussed in this section.

Liao et al. [17] studied the c-Si passivation of 60 nm TiO_x films deposited on HF-cleaned c-Si (see Figure 4.1A). Three important factors for the passivation are found in that study. First of all, a post-deposition anneal of the TiO_x films at 200-250 °C in N_2 ambient reduced the recombination velocity from $S_{eff,max}$= 38 cm/s to $S_{eff,max}$= 11 cm/s. Numerous studies report similar improvements upon annealing [18], [31], [19], [32], [33], thereby proving the beneficial effect of a post-deposition treatment. Secondly, light soaking of the annealed TiO_x improved the passivation: a recombination velocity as low as $S_{eff,max}$= 2.8 cm/s has been obtained. The passivation improvement upon light soaking is reported to be a lasting effect (up to eight months). The reason behind the improvement is assigned to traps in the TiO_x occupied by electrons injected from the silicon with aid of light. Light soaking is thus assumed to increase or introduce field-effect passivation. A

recent paper by Matsui et al. [20] reported large upward band bending in n-type silicon induced by thermal ALD TiO_x, another indication of field-effect passivation. Other papers about field-effect passivation of ALD TiO_x are rare. A third finding of the study is that crystalline TiO_x films seems to be detrimental to passivation. This finding is supported by the work of Plakhotnyuk et al. [32]. The detrimental effect might be attributed to a higher Si - TiO_x interface defect density or maybe due to a larger loss of hydrogen in crystalline TiO_x when compared to amorphous TiO_x. The mechanism responsable for hydrogen loss in crystalline TiO_x could be similar to the hydrogen loss in crystalline ZnO, which occurs through the grain boundaries of the crystal [34]. In the ZnO study by Van de Loo. [34], a sacrificial ALD aluminum oxide capping layer on the ZnO prevented the loss of hydrogen and significantly improved the passivation quality. It could therefore be interesting to investigate such a sacrificial ALD aluminum oxide capping for crystalline TiO_x films (see Figure 4.1B for the sample structures).

Another interesting material stack that involves TiO_x for c-Si passivation, is reported by Boccard et al. [35]. They investigated a material stack consisting of a textured c-Si wafer, covered with 6 nm intrinsic hydrogenated amorphous silicon (a-Si:H(i)) which was capped with 7.5 nm TiO_x (see Figure 4.1C). This stack provides excellent passivation: they measured lifetimes as high as 2.9 ms. Note that a significant part of the passivation is likely to originate from the excellent chemical passivation that a-Si:H(i) can generally provide [36].

Next to the combination of c-Si with TiO_x and an a-Si:H(i) interlayer, Table 4.1 yields also several results for c-Si and TiO_x with differently grown silicon oxide interlayers (with a thickness ranging between 1 and 2 nm). First of all, Yang et al. [18] investigated the passivation of a c-Si wafer with a thermally grown silicon oxide layer in combination with TiO_x. This yielded a good, but slightly lower passivation level ($S_{\text{eff,max}}$ = 14 cm/s) compared to HF-cleaned silicon ($S_{\text{eff,max}}$ = 11 cm/s). An important benefit of the thermally grown silicon oxide is however the improved thermal stability of the passivation. Secondly, a silicon oxide layer grown by nitric acid oxidation of silicon (NAOS) has been explored, showing a fair level of passivation ($S_{\text{eff,max}}$ = 17.5 cm/s) [33]. A third way that has been used to grow a silicon oxide layer is by storing a bare silicon surface in air. A silicon oxide interlayer grown in this way yielded a recombination velocity as low as $S_{\text{eff,max}}$= 10 cm/s, which means an excellent level of passivating. It can thus be concluded that TiO_x can provide good passivation on both bare silicon (HF-cleaned silicon) and silicon with a silicon oxide. It would be nteresting to further investigate the differences in performance between differently grown silicon oxide interlayers and to check the thermal stability of the passivation compared to HF-cleaned silicon. A last intersting finding concerning SiO_x is reported by Scheerder et al. [33]. They showed with the help of a transmission electron microscopy (TEM) analysis that the deposition of TiO_x on bare silicon with the TTIP precursor forms a silicon oxide interlayer during the thermal ALD process. Annealing of a TiO_x film deposited on bare silicon is also reported to grow a silicon oxide interlayer [37]. Especially with regard to the high passivation obtain by Scheerder et al., a more profound look at the formation of such an interlayer would be an interesting research topic. More specifically, it would be intersting to investigate wether there is always a SiO_x interlayer between c-Si and TiO_x, even for TiO_x on HF-cleaned c-Si.

Concerning the ALD preparation of the TiO_x films, it can be stated that all reported precursors (tetrakis-dimethylamido titanium (TDMAT), titanium(IV)tetrachloride ($TiCl_4$) and titanium(IV)isopropoxide (TTIP)) can provide well passivating TiO_x films with recombination velocities as low as $S_{\text{eff,max}} \leq 11$ cm/s (see Table 4.1). The used ALD deposition temperature varies for $TiCl_4$, TTIP, TDMAT and is respectively reported to be 75-100°C, 200-250°C and ± 200°C. Next to thermal ALD, there is plasma-enhanced ALD (PEALD). Scheerder et al. [33] explored PEALD for TiO_x passivation and found lower passivation levels when compared to thermal ALD. This may be attributed to damage of the c-Si surface from ultraviolet light and high energetic particles from the plasma striking the surface. Additional research about the passivating qualities

of PEALD TiO_x is however required to be conclusive.

As mentioned in the introduction of this chapter, the effect of the TiO_x material properties, like the stoichiometry (oxygen to titanium ratio), impurity content, density and the associated electrical properties (e.g. electrical resistivity, electron concentration) have not been thoroughly addressed in literature, although this is of great interest when aiming to achieve excellent surface passivation of c-Si.

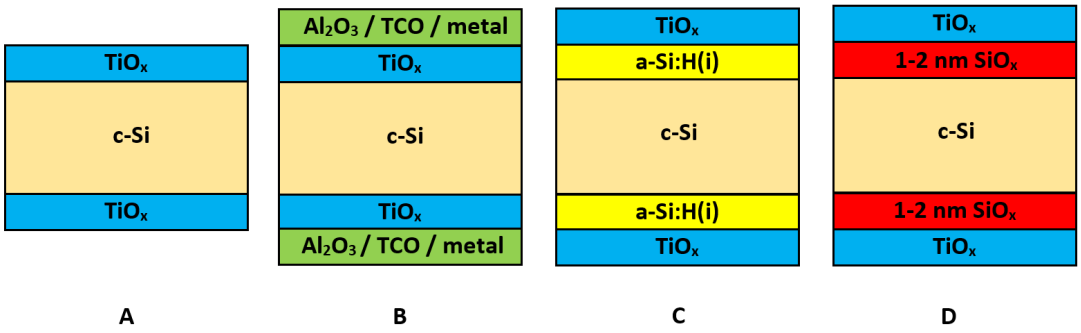

Figure 4.1: Different configurations in which TiO_x could be used to provide c-Si surface passivation.

4.2 Contact resistivity

Besides passivation, the contact resistivity is an important parameter for a carrier-selective passivating contact (see Section 2). Several groups investigated the contact resistivity of TiO_x by following the approach of Cox and Strack [38] (see Section 5.2.4). An overview of the reported contact resistivity (ρ_c) values can be found in Table 4.2.

Allen et al. found a very low contact resistivity for c-Si/TiO_x/Ca stacks. Values of 5 mΩcm^2 and 27 mΩcm^2 were found for 3.5 nm and 5.5 nm thick TiO_x films respectively [19]. Remarkably, they found rectifying behavior when they used aluminum as contact material [19], [39]. An estimation of the contact resistivity for 3.5 nm TiO_x with aluminum resulted in a value of 150 mΩcm^2, which is almost two orders of magnitude larger in comparison to calcium. An explanation is provided by a TEM analysis which shows a significant oxygen reduction of the TiO_x by the calcium contact. The resulting substoichiometric TiO_x is assumed to be crucial for the realization of the low Ohmic contacts. Since calcium (work function ~2.9 eV Allenpc) has the property to oxidize more easily than aluminum (work function ~4 eV [16]), Ca is argued to cause a larger reduction of the TiO_x an hence yield a lower contact resistivity. From literature it is known that reduced TiO_x shows much higher conductivity [40], [41] and therefore it may reduce the bulk contribution of the TiO_x in the total contact resistivity. Two other proposed explanations are an improved band alignment of TiO_x with the silicon and a reduced potential barrier at the Si - TiO_x interface. Besides the argumentation of Allen et al. that calcium can cause a stronger oxygen reduction of TiO_x than aluminum, the lower work function of the calcium may also introduce a larger downward band bending in the silicon, thereby creating a better Ohmic contact than a higher work function metal like aluminum. The importance of this effect is for example emphasized by the work of Matsui et al. [20], which will be discussed later on.

Yang et al. have also reported contact resistivity values using aluminum as contact material. The values range between 25 mΩcm^2 and 0.1 Ωcm^2 for TiO_x films ranging from 2.5 nm to 5.5 nm [18]. These values show a large increase of the contact resistivity with the TiO_x thickness, which therefore seems to be an important factor for the contact resistivity. A second important factor that is pointed out in this paper is the beneficial effect of a post-deposition forming gas anneal at 250 °C. This annealing reduced the contact resistivity by nearly an order of magnitude. Yang et al. conclude with the help of a TEM analysis, like Allen et al., that an oxygen reduction of the TiO_x takes place upon annealing. This is assumed to be the cause of the lower contact resistivity.

From the work of Yang et al. and Allen et al., it becomes clear that the contact material adjacent to the TiO_x layer can play an important role in the contact resistivity value. Boccard et al. [35] compared different TiO_x contact materials by studying several solar cells with both Al and indium tin oxide (ITO) on top of a TiO_x layer. It was observed that the ITO (work function ~4.8 eV) devices had a poor performance, probably due to the high work function of the ITO, which created a barrier for electron extraction. Matsui et al. [20] measured the open circuit voltage of solar cells with TiO_x in combination with different contact materials (Al, Ti, Pd, ITO). They found a clear increase of the open circuit voltage with a decrease of the work function of the contact material. Based on this observation they note that even with the presence of the few nanometers thick TiO_x interlayer, the work function may induce band bending in the silicon.

From the work of Allen et al. [19], Yang et al. [18], Boccard et al. [35] and Matsui et al. [20] it can be concluded that the contacting material of the TiO_x is very important when aiming for an electron-selective TiO_x-based contact. The reason for this importance might be attributed to the role of the contacting material in the oxygen reduction of TiO_x, which is reported to be very important for creating a low Ohmic contact. Secondly, the data from these four papers seems to suggest a correlation between the work function and the contact resistivity. Low work function contact materials should induce downward band bending in the silicon, which could create an Ohmic contact. A more profound investigation of these two presumed effect could prove very useful in improving the performance of a passivating contact based on TiO_x.

Except for the stoichiometry, the role of the material properties of the TiO_x (impurity content, density) has not been investigated. Furthermore, the effects of the ALD temperature and the effect of plasma-enhanced ALD process on the contact resistivity are not yet clear.

4.3 Research topics for future work

This section presents an overview of the suggestions for future work based on the findings described in sections 3.1 and 3.2:

1) Investigation of the role of the Si - TiO_x interface on the passivating qualities (and the thermal stability of the passivation). More specifically: exploring the properties, passivation level, and passivation stability of TiO_x on both HF-cleaned silicon and on silicon with differently grown silicon oxide layers.

2) Clarification of the role of field-effect passivation in the passivation of c-Si with TiO_x

3) Investigation of the effect of the TiO_x material properties (e.g. stoichiometry (oxygen to titanium ratio), impurity content, density, electric properties) on the passivation and

contact resistivity of TiO_x/c-Si

4) Exploriation of the passivating qualities of material stack with TiO_x relevant for solar cell applications. Examples include Si - TiO_x - metal and Si - TiO_x - TCO stacks.

5) Is it possible to achieve higher levels of passivation with crystalline TiO_x when a sacrificial aluminum oxide capping layer is applied

6) For a low contact resistivity it seems necessary to reduce the oxygen content from the TiO_x, by applying a low working metal and or a forming gas anneal. It would be interesting is to understand more about the role and mechanism of both the work function and the forming gas anneal.

Table 4.1: Literature overview of the passivation of ALD TiO_x on non-textured n-type c-Si (unless reported differently). GPC stands for the TiO_x film growth per ALD cycle. T_{dep} refers to the ALD temperature. The resistivity of the silicon substrate is indicated by $\rho_{c\text{-}Si}$.

Ti precursor	GPC (Å/cycle)	T_{dep} (°C)	Thickness (nm)	Stack	$\rho_{c\text{-}Si}$ (Ω·cm)	$S_{eff,max}$ (cm/s)	Remark	Ref.
$TiCl_4$	0.6	100	60	c-Si/TiO_x	2.5	2.8	Light soaking	[17]
TTIP	0.16	200	5.2	c-Si/TiO_x	1-5	7	SiO_x interlayer forms during ALD	[33]
TTIP	0.35	230	5.5	c-Si/TiO_x	1	10	RCA oxide	[31]
$TiCl_4$	0.7	75	5.5	c-Si/TiO_x	1	11	-	[18]
$TiCl_4$	0.6	100	60	c-Si/TiO_x	2.5	11	-	[17]
$TiCl_4$	0.7	75	3.0	c-Si/TiO_x	1	15	Used in current TiO_x record cell of $\eta \approx 22.1\%$	[18]
TTIP	-	230	10.5	c-Si/TiO_x	-	15	-	[19]
TDMAT	0.16	200	11	c-Si/TiO_x	1-5	15.6	-	[33]
$TiCl_4$	0.54	80	10	c-Si/TiO_x	5	44	P-type c-Si	[32]
TTIP	-	230	3.5	c-Si/TiO_x	-	66.7	Used in TiO_x cell with $\eta \approx 21.8\%$	[19]
TDMAT	-	215	5	c-Si/SiO_x/TiO_x	1.3	10	Native SiO_x grown over 4 months	[21]
$TiCl_4$	0.7	75	3.5	c-Si/SiO_x/TiO_x	1	14	1.2nm Thermal SiO_x (700°C)	[18]
TTIP	0.4	250	4	c-Si/SiO_x/TiO_x	1-5	17.5	PEALD 1-2 nm NAOS SiO_x	[33]
TTIP	0.16	200	7.5	c-Si/SiO_x/TiO_x	1-5	23.3	1-2nm NAOS SiO_x	[33]
$Ti(Cp^{Me})(NMe_2)_3$	0.8	50	5	c-Si/SiO_x/TiO_x	1-5	38.9	PEALD 1-2 nm NAOS SiO_x	[33]
$TiCl_4$	0.45	100	10	c-Si/SiO_x/TiO_x	5	44	1.38 nm NAOS SiO_x p-type c-Si	[32]
TTIP	0.4	250	5	c-Si/SiO_x/TiO_x/Al_2O_3	1-5	15.6	PEALD 1-2 nm NAOS SiO_x Al_2O_3 capping	[33]
$TiCl_4$	0.54	80	10	c-Si/Al_2O_3/TiO_x	5	17.5	1 nm ALD Al_2O_3 p-type c-Si	[32]
TTIP	0.35	230	7.5	c-Si/a-Si:H/TiO_x	3	2.9	-	[35]

Table 4.2: Literature overview of the contact resistivity of TiO_x on non-textured n-type c-Si. GPC stands for the TiO_x film growth per ALD cycle. T_{dep} refers to the ALD temperature.

Ti precursor	GPC (Å/cycle)	T_{dep} (°C)	Thickness (nm)	Stack	ρ_c ($\Omega \cdot cm^2$)	Remark	Ref.
TTIP	-	230	3.5 - 5.5	c-Si/TiO_x/Ca	0.005 - 0.027	Annealed, metalization has reduced TiO_x	[19]
TTIP	-	230	3.5	c-Si/TiO_2/Ca	0.005	Used in cell with $\eta \approx$21.8%	[19]
$TiCl_4$	0.7	75	2.5 - 5.5	c-Si/TiO_x/Al	0.02 - 0.1	Annealed, metalization has reduced TiO_x	[18]
$TiCl_4$	0.7	75	3	c-Si/TiO_x/Al	0.026	Used in cell with $\eta \approx$ 22.1%	[18]
TTIP	-	230	3.5	c-Si/TiO_x/Al	0.15	Annealed, metalization has reduced TiO_x	[19]
TTIP	0.16	200	4	c-Si/TiO_x/Al	0.3	Annealed	[33]
$TiCl_4$	0.7	75	2.5 - 5.5	c-Si/SiO_x/TiO_x/Al	0.025 - 0.25	Annealed, metalization has reduced TiO_x	[18]
TDMAT	-	215	2 - 5	c-Si/SiO_x/TiO_x/Al	0.74 - 0.78	-	[21]

Chapter 5

Titanium oxide

5.1 Introduction

The aim of this chapter is to contribute to the understanding of the important factors and mechanisms for the passivation and contact resistivity of TiO_x, by performing experimental work on the following research topics:

1) The role of the Si - TiO_x interface on the passivating qualities is explored. To be more specific, the effect of different pre-treatments (HF-cleaning, RCA cleaning and a NAOS treatment) of the c-Si surface on the passivating properties of TiO_x are investigated.

2) The effects of a post-deposition FGA of TiO_x on the contact resistivity and passivation of TiO_x.

3) The effect of the TiO_x material properties (e.g. stoichiometry, impurity content, density, electric properties) on the passivation and contact resistivity of TiO_x.

4) The effects of the TiO_x film thickness on the contact resistivity and passivation of TiO_x.

5) The role of field-effect passivation in the surface passivation of c-Si with TiO_x.

This chapter starts with a description of the experimental setup. This section explains how and with which measurement techniques the above mentioned research questions have been investigated. The second and third sections show the results of the TiO_x material and Si - TiO_x interface characterization respectively. The results of these two section are consequently used to understand and correlate results of the passivation and contact resistivity of TiO_x. The latter two are presented in the following two sections which also address the effects of a post-deposition FGA on the contact resisitivty and passivation. At the end of this chapter, the first research goal of this work is answered by discussing the most important findings of the experimental work on TiO_x and recommendations for further research are presented.

5.2 Experimental details

5.2.1 Overview of the experiments and methods

The strategy adopted to investigate and understand the factors that are important for the passivation and contact resistivity of TiO_x is as follows: the ALD temperature, TiO_x film thickness, and surface treatment of the silicon substrate are varied to create different TiO_x films and different interfaces between the silicon substrate and the TiO_x film. The material properties of the different TiO_x films and the properties of the interfaces with silicon substrate are investigated and correlated to the measured changes in the passivation and contact resistivity. The material properties that are investigated are listed below together with the associated measurement technique.

Table 5.1: The material properties that are investigated together with the associated measurement technique.

Property	**Measurement technique(s)**
Crystallinity	Raman spectroscopy,
	X-ray diffraction
Stoichiometry	X-ray photoelectron spectroscopy
Chemical impurity content	X-ray photoelectron spectroscopy
Electrical conductivity	four-point-probe,
	Hall measurements
Bandgap (optical)	spectroscopic ellipsometry
Refractive index	spectroscopic ellipsometry
Density	spectroscopic ellipsometry
Optical absorption	spectroscopic ellipsometry

Different Si - TiO_x interfaces are studied. For this purpose TiO_x is deposited on HF-cleaned silicon (i.e. H-terminated silicon surface; no silicon oxide present prior to TiO_x deposition) and on two differently grown silicon oxide layers. The first silicon oxide is grown by a RCA-clean (Radio Corporation of America) of the silicon. The second is silicon oxide is grown by nitric acid oxidation of silicon (NAOS). The interfaces are analyzed by looking at the silicon oxide layer thickness, stoichiometry of the silicon oxide interlayer and chemical bonds (what interface does TiO_x form on HF-cleaned silicon?). An overview of the Si - TiO_x interface properties that are investigated is listed in Table 5.2 together with the associated measurement technique.

Table 5.2: The Si - TiO_x interface properties that are investigated together with the associated measurement technique.

Property	**Measurement technique(s)**
SiO_x thickness	spectroscopic ellipsometry,
	X-ray photoelectron spectroscopy,
	transmission electron microscopy
SiO_x stoichiometry	X-ray photoelectron spectroscopy
Chemical bonds	X-ray photoelectron spectroscopy

The passivation of the Si - (SiO_x) - TiO_x stacks is determined by quasi-steady-state photoconductance (QSSPC). The effects of a post-deposition FGA on the passivation is investigated by varying the annealing atmosphere and by monitoring the minority carrier lifetime (measure of the passivation quality) with QSSPC as function of anneal time for different TiO_x films and interfaces. To investigate the role of field-effect passivation, surface photovoltage measurements are performed.

The contact resistivity of Si - TiO_x - Al stacks is determined for different TiO_x films by the Cox-Strack method [38]. The contact resistivity is further investigated by analysis of the current-voltage behavior for different TiO_x films and by addressing the effect of post-deposition annealing.

Some of the above mentioned measurement techniques are considered to require additional explanation because they are specific for solar cell research (contact resistivity and passivation characterization) or since the usage and interpretation of the technique is not evident or complicated. First, additional information is provided on the ALD process to deposit the TiO_x layers. Next, the structure and characterization of the passivation and contact resistivity structures is discussed. The last subsections will cover the experimental details of the spectroscopic ellipsometry and X-ray photoelectron spectroscopy experiments.

5.2.2 Atomic layer deposition of titanium oxide

The TiO_x films were deposited by a FlexAl ALD-system from Oxford Instruments using the commercial precursor tetrakis-dimethylamido titanium (TDMAT) and H_2O as oxidant (see Figure 5.2). The motivation for this precursor is its relatively high growth rate and wide temperature window compared to (non-halide) precursors like TTIP. For example at 200 °C, TTIP has a GPC of 0.15 Å/cycle [33], while TDMAT reaches 0.52 Å/cycle. An overview of the ALD recipe can be found in Figure 5.1.

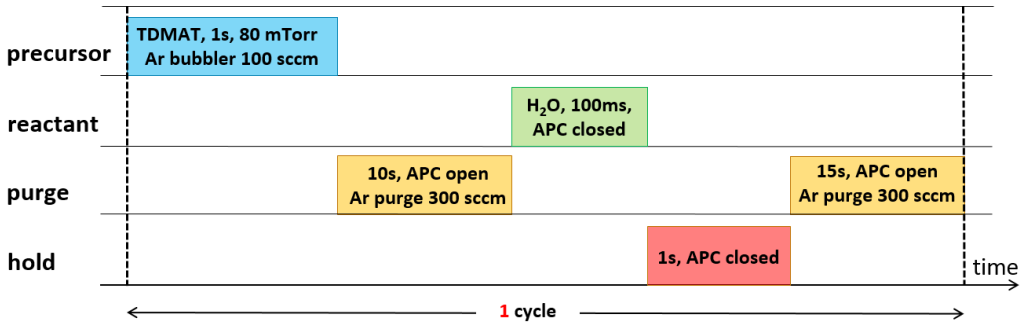

Figure 5.1: Schematic representation of the atomic-layer-deposition recipe of titanium oxide. APC stands for 'Automatic Pressure Controller'. The APC separates the reaction chamber from the pump; when the valve of the APC is completely open, the reaction chamber is pumped at maximal intensity.

During the experiment, the set substrate temperature is kept constant and will be referred to as deposition temperature (T_{dep}) in this report. Different deposition temperatures are investigated, ranging from 50 °C to 300 °C. The wall temperature of the reactor is kept at the same temperature as the substrate, but for substrate temperature of 150°C and higher, the wall temperature is kept at its maximum value of 150°C. At the start of recipe, there is a 15 minutes pre-heat step of the substrates at 200 mTorr. After depositions and between measurements, the samples are stored in air at room temperature in the dark.

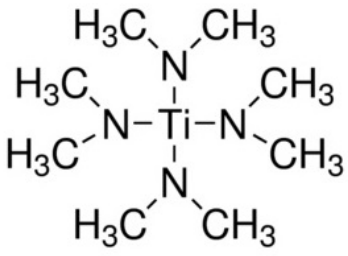

Figure 5.2: Tetrakis-dimethylamido titanium (TDMAT) precursor.

5.2.3 Fabrication and characterization of the passivation samples

Fabrication details

From the literature overview of the contact resistivity of TiO_x as presented in Table 4.2, it has become clear that acceptable contact resistivity values ($\leq 0.1\ \Omega{\cdot}cm^2$) can be obtained for relatively thin TiO_x films, around 3.5 nm. The literature overview for the c-Si surface passivation by TiO_x as reported in Table 4.1 shows that the best passivation results are generally obtained for slightly thicker film thickness (4-10 nm or even 60 nm). Since both contact resistivity and passivation are important for the contact quality, it has been decided to test TiO_x films with thicknesses between 1 and 5 nm, which covers thickness values in the reported optimal ranges of both contact resistivity and passivation.

The TiO_x films were deposited on both sides of 280±20 μm thick, double side polished, n-type FZ <100> wafers (see Figure 5.3 for a schematic representation). The FZ wafers are phosphorous-doped with a resistivity of 1-5 $\Omega{\cdot}$cm. To create different TiO_x film properties and to investigate the effect of the ALD temperature, the deposition temperature was varied over a wide range between 50°C and 300°C at a fixed film thickness of 5 nm. The 1 to 5 nm thickness variation of the TiO_x films for the passivation study were deposited at a temperature of 200°C, which is approximately in the middle of the investigated temperature window of TDMAT.

Before the TiO_x was deposited, three different surface pre-treatments were applied to vary the surface properties of the c-Si. The latter makes it possible to clarify the effect of the silicon TiO_x interface on the passivation level and to investigate the by Yang et al. [18] reported higher thermal stability of the TiO_x passivation in combination with a silicon oxide interlayer. One set of wafers underwent a full RCA (Radio Corporation of America) clean performed by the wafer supplier. The silicon wafers with RCA pre-treatment had an oxide layer of about 1.5 nm thick. This layer was formed in a solution of 6 H_2O : 1 H_2O_2 : 1 HCl for 10 minutes between 75 °C and 80 °C. This process is known as RCA standard clean 2. This process provides a very thorough cleaning and therefore a silicon oxide layer with very few impurities [42]. This set of wafers is referred to as 'RCA'. The second set of wafers was stripped from their SiO_x layer by etching the wafers with a 1% hydrofluoric acid (HF) solution for 1 min followed by 1 min rinsing in deionized water plus quick drying with a nitrogen blow gun. In this way a hydrogen terminated silicon surface is obtained. This set of wafers is referred to as 'HF'. The third set of wafers was stripped from their SiO_x layer by etching the wafers with a 1% hydrofluoric acid (HF) solution. Subsequently, a new SiO_x layer of 1-1.5 nm [43] is grown using a 60% HNO_3 acid solution at room temperature for 5 min followed by 1 min rinsing in deionized water plus quick drying with a nitrogen blow gun. This set of wafers is indicated with 'NAOS'. The result of the different pre-treatments is visualized in Figure 5.3. The number of ALD cycles required to deposit a specific TiO_x film thickness was determined from the growth per cycle of the ALD process which had been determined beforehand (see Figure 5.10).

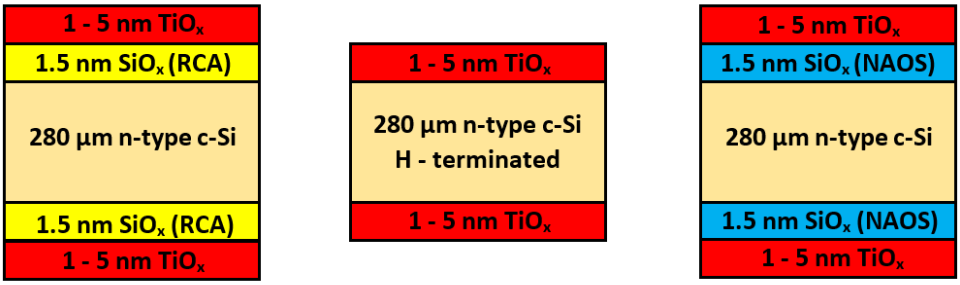

Figure 5.3: Schematic representation of the structures used to investigated the c-Si passivation of a few nm TiO_x with QSSPC. Left: c-Si wafer with RCA treatment which forms a SiO_x layer of approximately 1.5 nm thick (referred to as RCA). Middle: c-Si wafer with hydrogen terminated surface created by HF treatment (referred to as HF). Note that the ALD process may also form a SiO_x interlayer [33]. Right: c-Si wafer with HF treatment followed by NAOS treatment to create oxide layer of 1 - 1.5 nm thick (referred to as NAOS).

Characterization

The passivation quality of the c-Si surface is expressed by the effective lifetime of excess carriers in the c-Si. This is done with the quasi-steady-state photoconductance method using the Sinton Silicon Wafer Lifetime Tester (WCT-120TS) (see Figure 5.4 for the schematic setup of this apparatus). This lifetime tester produces light to generates excess carriers in a c-Si wafer. The excess carriers increase the conductance σ_L, hence permeability of the c-Si wafer. The changing permeability is sensed by a coil of a radio-frequency bridge. A reference solar cell measures the light intensity and the associated photogeneration rate J_{ph}. With the help of σ_L and J_{ph}, the effective lifetime τ_{eff} can be determined:

$$\tau_{eff} = \frac{\sigma_L}{J_{ph}(\mu_n + \mu_p)}, sinton \tag{5.1}$$

where μ_n and μ_p are the mobility of the electrons and holes respectively. The electron and hole mobility are functions of the photo-generated excess carrier concentration in the c-Si Δn, which can be found in literature. An iteration of the equation below (Equation 5.2) enables consequently to find both Δn and $(\mu_n + \mu_p)$ consistent with the measured photoconductance [44].

$$\sigma_L = q\Delta n(\mu_n + \mu_p)W.[44] \tag{5.2}$$

In this equation, W represents the c-Si wafer thickness and q the elementary charge.

The above equations are not only valid for a steady illumination (steady-state photoconductance), but also when the decay of the light intensity has a much longer timescale than the minority-carrier lifetime of the carriers in the c-Si (quasi-steady-state photoconductance). The latter allows to asses the effective lifetime as a function of light intensity, hence excess minority carrier density. In this work τ_{eff} is determined as function of the excess minority carrier density and then reported at the

commonly used excess minority carrier density of $1{\cdot}10^{15}$ cm^{-3}.

The maximum effective surface recombination velocity (S_{eff}) is independent from the c-Si wafer thickness and is calculated from the measured lifetime using the following equation [44]:

$$\frac{1}{\tau_{\text{eff}}} = \frac{1}{\tau_{\text{bulk}}} + \frac{2S_{\text{eff}}}{W}, \tag{5.3}$$

where τ_{bulk} is the c-Si bulk lifetime and W the wafer thickness. The value for τ_{bulk} is very high due to the high quality of the FZ c-Si wafers used in this passivation study. In this work the recombination velocity is approximated by assuming $\tau_{\text{bulk}} \approx \infty$. This approximation provides an upper limit for the effective recombination velocity: $S_{\text{eff,max}}$. Another measure for the passivation quality, the recombination current (J_0), is determined from a linear fit of the inverse lifetime as a function of the carrier density.

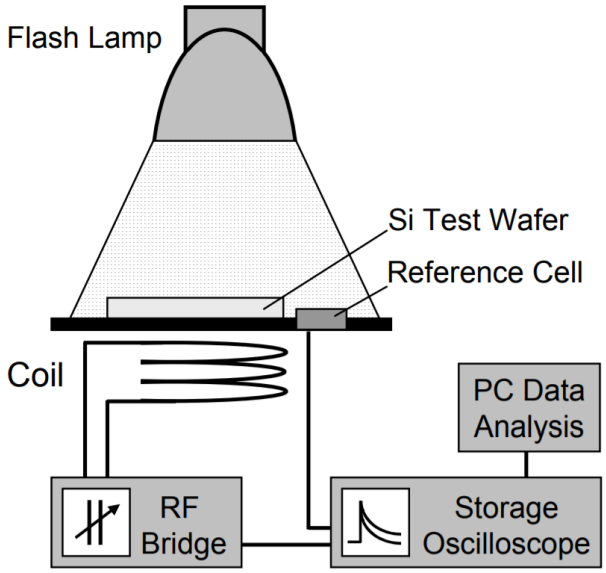

Figure 5.4: Schematic representation of a QSSPC apparatus. A c-Si wafer (with or without a passivating layer) is subjected to a light flash, which generates additional carriers in the c-Si. The light intensity of the flash is measured with a reference cell. A coil on which the c-Si wafer is positioned, measures the changing permeability of the c-Si wafer upon illumination. With the help of these two quantities the effective lifetime can be determined. [45]

Post-deposition annealing

In the previous chapter it has been discussed that post-deposition annealing in forming gas [18],[31], nitrogen or air at 250 °C have resulted in large improvements of the passivation. Part of this work is to investigate this effect. For this purpose the passivation samples are annealed in small time steps and after each step the effective minority carrier lifetime (τ_{eff}) is measured. This method makes

it possible to construct a plot of the lifetime versus the cumulative anneal time. Such a graph provides information about the passivation behavior, and the thermal stability and it becomes possible to find the optimum anneal time, in terms of lifetime, for each sample. The annealing of the TiO_x samples is performed with a Jipelec Rapid Thermal Annealing (RTA) system in an atmosphere of both pure nitrogen gas and in a mixture of nitrogen and hydrogen gas at ratio of N_2:H_2 = 9:1. The annealing is performed at a similar temperature as the above mentioned studies: 300 °C.

5.2.4 Fabrication and characterization of the contact resistivity samples

In this work, the contact resistivity of a Si-TiO_x-Al contact is investigated. The contact resistance of this contact configuration consists of the resistance arising from the Si-TiO_x interface, the TiO_x layer resistivity, and the TiO_x-Al interface. [1] When performing I-V measurements of this stack, the measured resistance has also contributions from the resistivity of the silicon substrate, the resistance that arises by contacting the silicon substrate with the measurement circuit and the resistance of the wires that are part of the measurement circuit. A suitable method to separate the contact resistivity from these other resistance contributions, is an analysis based on the Cox-Strack method [38].

The contact structure used to determine the contact resisitivty is presented in Figure 5.5. The contact structure consists of a 280±20 μm n-type c-Si CZ wafer with an n+ diffusion at the rear of the silicon substrate to create an Ohmic contact with the aluminum (sheet resistance $\approx 25\ \Omega/sq$). The front side of the CZ wafer contains a native oxide ($\approx$ 1.5 nm) formed during production of the rear n+ diffusion and metallization. This native oxide was stripped prior to TiO_x deposition by applying a 1% HF solution for 2 minutes, followed by 1 minute rinsing in deionized water and drying with a nitrogen blow gun. After ALD of the TiO_x films, 300 nm thick circular aluminum dots with diameters ranging from 0.2 to 10 mm were thermally evaporated through a shadow mask. The aluminum dots serve as a front contact of the structure and the diffusion with the aluminum rear as back contact. The effect of the TiO_x material properties and the TiO_x film thicknesses on the contact resistivity is investigated by preparing and measuring different TiO_x layers, as described in the previous subsections.

[1] Note that in this work, the term contact resistivity is used for the resistivity of the whole Si-TiO_x-Al stack. This definition of the contact resistivity is not uncommon in the field of solar cells [39], [18], [31] and MIS-contact studies [28], [40], but in other research fields the contact resistivity is often referred to as the resistance arising from only one interface.

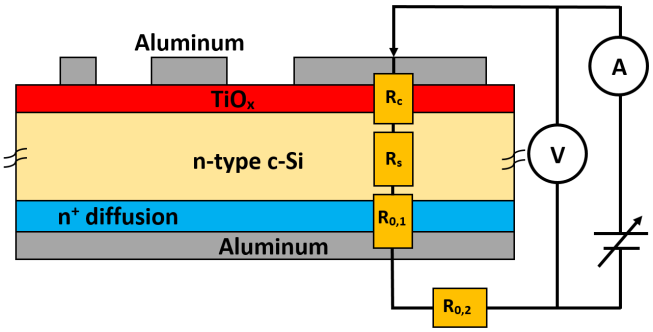

Figure 5.5: A schematic representation of the contact resistivity samples: a 280 μm thick n-type c-Si wafer with n+ diffusion on the rear to ensure an Ohmic contact with the aluminum back layer and a 1-5 nm thick TiO_x layer deposited on the front side of the substrate. The front contacts consist of 300 nm thick circular aluminum dots with diameters ranging from 0.2 to 10 mm.

The different resistance contributions that arise from the electronic circuit as presented in Figure 5.5 can be expressed using the work of Cox and Strack [38]. The resistance that arise from the silicon substrate R_s is determined by the resistivity of the silicon, the thickness of the silicon and spreading of the current through the silicon. According to Cox-Strack spreading through a semiconductor can be mathematically approximated by:

$$R_s = \frac{\rho}{d\pi} arctan(\frac{4t}{d}), \tag{5.4}$$

where ρ is the resistivity of the n-type c-Si wafer, t the thickness of the c-Si wafer and d the diameter of the aluminum front contact. The resistance that arises due to the contact resistivity R_c depends on the diameter of the Al front contact and is expressed by:

$$R_c = \frac{4\rho_c}{d^2\pi}, \tag{5.5}$$

where ρ_c is the contact resistivity. Note that no lateral spreading of the current throught the TiO_x layer is assumed. The reason for this is that the TiO_x layer thickness (nm) is much smaller than the width of the the Al diameters (mm). The resistance contribution due to the low Ohmic back contact of the Si substrate $R_{0,1}$ and the resistance of the wires and connections that make up the electrical circuit are accounted for by:

$$R_0 = R_{0,1} + R_{0,2}, \tag{5.6}$$

where R_0 is a constant; i.e. independent of the diameter. The total measured resistance R_t is consequently:

$$R_t = R_s + R_c + R_0 = \frac{\rho}{d\pi} arctan(\frac{4t}{d}) + \frac{4\rho_c}{d^2\pi} + R_0, \tag{5.7}$$

In this expression, the diameter d of the aluminum front contact is the experimental variable, while the contact resistivity ρ_c and R_0 are the fitting parameters. By measuring the resistance as a function of the diameter, expression 5.7 can be used to fit this data and find the contact resistivity. To determine R_t, a voltage sweep is applied over the contact structure of Figure 5.5 and the resulting current is measured. From slope of these curves at the origin, R_t is determined. These I-V measurements are performed in the dark at room temperature (293 K) under vacuum conditions (10^{-7} Bar).

5.2.5 Spectroscopic Ellipsometry (SE)

Spectroscopic ellipsometry (SE) is an optical measurement technique that is well suited to investigate very thin films since it can provide information down to the sub-nanometer level [46].

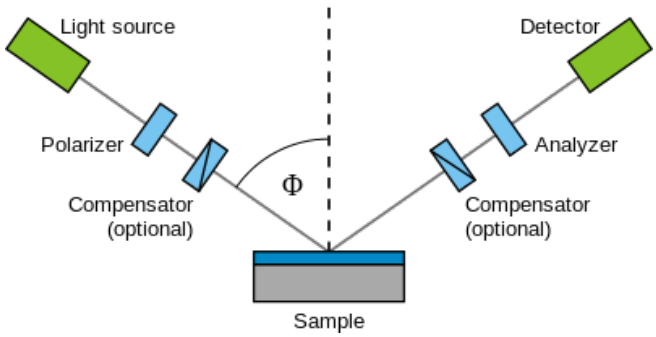

Figure 5.6: Schematic representation of an ellipsometry setup. Note that the optical elements can vary, since there are multiple ellipsometry setups possible. [47]

The spectroscopic ellipsometer creates light with a known polarization state and measures the changes of the polarization state upon reflection on the measured sample as a function of the wavelength. The two parameters that identify the change of the polarization state upon reflection are: Ψ and Δ [46]. The first one, Ψ, expresses the amplitude ratio of the light with polarization direction parallel to the plane of incident r_p and the light with polarization direction perpendicular to this planer_s. The phase difference between these two polarization directions is expressed by Δ. An optical model of the measured sample is used to calculate Ψ and Δ for different values of the models parameters (including the optical constants, layer thickness, and roughness of the film). The simulated Ψ and Δ are fitted with the measured data to find the best values for the models parameters [48] .

The thickness, refractive index, and absorption coefficient of the TiO_x films are determined by spectroscopic ellipsometry. The TiO_x films are modeled with a B-spline model [48]. The parameters of this model are the layer thickness, refractive index, and extinction coefficient. Since the thin TiO_x film is highly transparent, the underlying substrate will have a significant contribution to the measured signal, meaning that this substrate needs to be accounted for in the optical model as well. The substrate consists of a crystalline silicon wafer with a SiO_x layer, which are both

modeled by a combination of a general oscillator model and a Cody-Lorentz oscillator model [48]. The parameters of both layers are fixed during the fit, except for the thickness of the SiO_x interlayer. To reduce the uncertainty in modelling of the substrate, two different substrates are used (c-Si with 1.5 nm RCA SiO_x andc- Si with 450 nm SiO_x). The data of both substrates are used simultaneously in the analysis by the model, which enhances the accuracy. To further improve accuracy, the ellipsometry data (Ψ and Δ) of the TiO_x films are acquired at different angles of incidence (60° - 75°).

A measure for the uncertainty of the physical quantities provided by the model is estimated using a 'parameter uniqueness fit'. This fit is a measure for the sensitivity of the model on a specific parameter. The chosen parameter is varied while the other parameters are kept constant. The mean squared error (MSE) of the simulated data compared to the measured data is plotted as function of the chosen parameter. A clear minimum in the graph indicates a good sensitivity of the model on the chosen parameter, hence a low uncertainty in the provided value. In many cases, the minimum of the graph consists of a range of values rather than a single value (see Figure 5.7). The uncertainty in the parameter is therefore estimated using the 'width' of the minimum as indicated in Figure 5.7. For the 5 nm TiO_x films presented in this work, the error in thickness is estimated to be $\approx$ 1 nm. The error of the thinner layers is estimated to range between 1 and 2 nanometer.

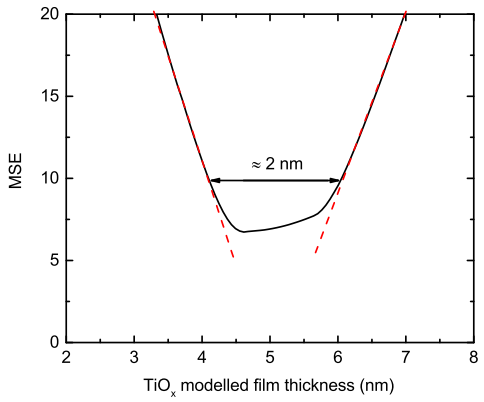

Figure 5.7: Parameter uniqueness fit. The mean squared error (MSE) of the simulated data compared to the measured data is plotted as a function of the TiO_x film thickness. The red arrow indicates the estimation of the uncertainty in the film thickness ($\approx$ 5 nm).

The optical bandgap of the material is determined with the help of Tauc's relation for a direct bandgap [6],[49]:

$$\alpha = \frac{\beta}{h\upsilon}(h\upsilon - E_g)^{1/2}, \tag{5.8}$$

where α is the absorption coefficient that can be determined from the spectroscopic ellipsometry, h is the Planck constant, υ the photon frequency, E_g the bandgap, and β a constant. By plotting $(\alpha h\upsilon)^{1/2}$ versus the photon energy ($h\upsilon$), a linear region appears. This region can be fitted with a linear line of which the intercept with the horizontal photon energy axis provides a numerical approximation of the bandgap.

5.2.6 X-ray photoelectron spectroscopy (XPS)

X-ray photoelectron spectroscopy (XPS) is a surface-sensitive spectroscopic measurement technique that is well suited to provide information about the elemental composition of a material. XPS uses X-rays to provide the electrons in the core levels of the atoms with enough energy to leave the material. The number of electrons emitted from the sample is measured by a spectrometer as a function of the electron binding energy to create a spectrum. Each element emits electrons at specific binding energies, creating a spectrum with peaks at characteristic energies, which make it possible to identify elements. The area of a peak of a specific element is a measure for the concentration of that element in the material. The peak area is multiplied with a sensitivity factor to correct for the sensitivity of the detector and loss features. This correction is however not perfect, which makes XPS more suited for a relative determination of the element concentration than an absolute one. Shifts in the peak position provides information about the chemical bonds of the element with its nearest neighbors. A peak in a XPS spectrum, for example the $Ti2p_{1/2}$ peak, is named after the element and the associated quantum numbers of the measured electrons: abbreviation of the element (Ti), principle quantum number (2), orbital angular momentum represented by a letter (p) and spin angular momentum (1/2) [50]. Figure 5.8 provides a schematic representation of the relation between the peaks in the measured XPS spectrum and the actual orbitals of the electrons of an atom. The XPS tool used in this work contains an ion beam to etch layers of the surface. This makes it possible to study the chemical composition of a film as function of film depth. The etch rate can however be significantly different for different elements, meaning that etching can alter the composition of the film (preferential sputtering) [50].

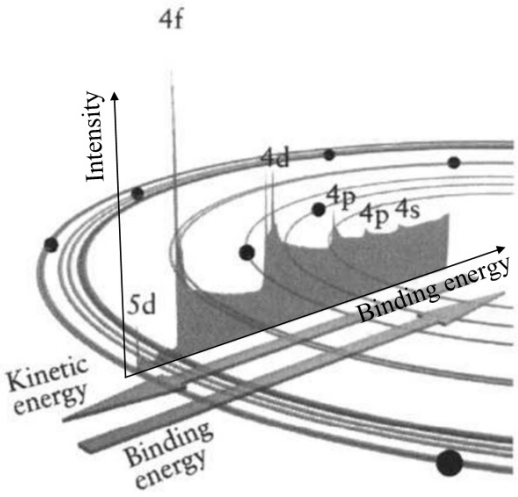

Figure 5.8: A schematic representation of the relation between the peaks in the measured XPS spectrum and the actual orbitals of the electrons. Adapted from [50].

For the TiO_x films, a quantification of the stoichiometry is performed by using the ratio between the normalized area of the titanium Ti2p doublet peaks and the oxygen O1s peak related to oxygen bonded to titanium. All measurements are performed at the surface of the TiO_x films to avoid differences in stoichiometry induced by preferential sputtering of oxygen [51]. The background subtraction method is a Shirley background with the additional constraint that the background should not be of greater intensity than the actual data at any point in the region. The uncertainty

in the oxygen-titanium ratio is based on the fitting error of the background.

To obtain information about the impurity content of the deposited TiO_x, a wide range energy scan is performed, covering the peak energies of all elements in the periodic table. This scan is performed after 30 seconds of sputtering with argon ions to remove absorbed contamination at the surface. In this way, the impurities in the TiO_x are measured and not those absorbed at the surface. The uncertainty in the impurity content is based on the fitting error of the background.

X-ray photoelectron spectroscopy measurements of the TiO_x films do not only provided information about the TiO_x film itself, but also about the silicon substrate and the silicon oxide layer between the TiO_x and the silicon. The latter is possible due to the fact that the TiO_x film thickness is in the same order as the electron escape depth of the XPS measurement, which is a few nanometers [50]. For information about the TiO_x/Si interface, we look at a the binding energies between 98 eV and 105 eV. In this range there are two peaks: the mean Si2p peak originating from the silicon substrate and a smaller Si2p peak coming from the silicon oxide interlayer (see Figure 5.9). The area of the latter peak (peak number 3 in Figure 5.9) is a measure of the number of silicon-oxygen bonds; i.e. the density and thickness of the silicon oxide interlayer. The area ratio of the silicon oxide peak (peak 3 in Figure 5.9) and the mean silicon substrate doublet peaks (peaks 1 and 2 in Figure 5.9) is used as qualitative measure of the density and thickness of the silicon oxide interlayer. This ratio is less sensitive to possible differences of the attenuation of the signal (induced by differences in for example the thickness and density of the overlaying TiO_x film) and is therefore preferred over the absolute area of the silicon oxide peak. With regard to the stoichiometry of the silicon oxide interlayer: the higher the oxygen to silicon ratio, the higher the binding energy of the silicon oxide peak. The binding energy of the silicon oxide peak is therefore a measure for the stoichiometry of the silicon oxide. To account for binding energy offsets between different measurements, the differences in binding energy between the silicon substrate peak (peak 2 in Figure 5.9) and silicon oxide peak (peak 3 in Figure 5.9) is used. In the results this difference will be referred to as ΔE_B.

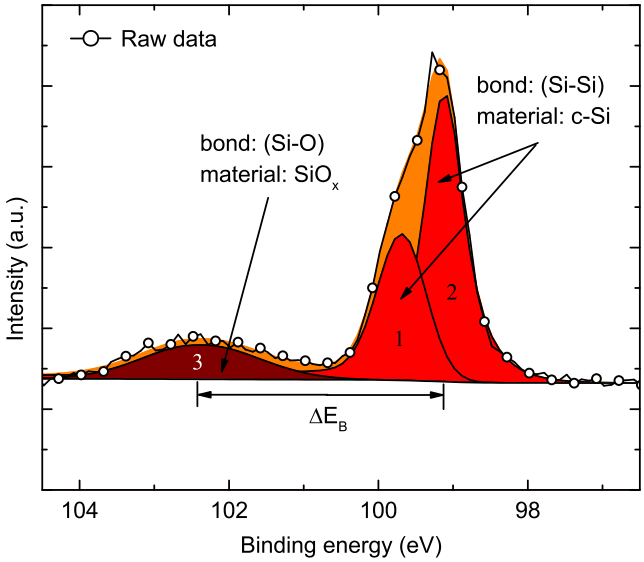

Figure 5.9: XPS signal for binding energies between 98 eV and 105 eV. The measured data are indicated by the black line with white dots. The data are fitted with the doublet peak for silicon (red colored peaks with numbers 1 and 2) and the silicon oxide peak (dark red colored peak with number 3). The orange color represents the sum of the fitted peaks.

5.3 Material properties

This chapter describes several material properties of the deposited TiO_x films in the as-deposited state and after a forming gas anneal at 300 °C. These material properties are helpful in explaining observed trends in the contact properties and can provide clues about the underlying physical mechanisms of the passivation and contact resistivity.

5.3.1 ALD growth

The growth per ALD cycle as a function of deposition temperature can be found in Figure 5.10. The growth per cycle (GPC) as presented in Figure 5.10 is determined by dividing the thickness of the film by the number of ALD cycles. The uncertainty in the GPC is determined from the uncertainty in the film thickness. There is a clear decreasing trend of the GPC as a function of deposition temperature. The latter might be attributed to an increased desorption of TDMAT at higher temperatures as reported by Xie et al. [52] or to a decreased number of adsorption site for the precursor.

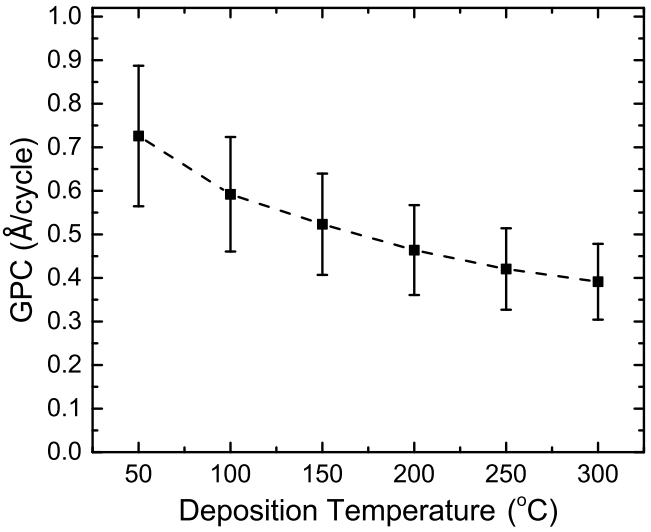

Figure 5.10: Growth per cycle of TiO_x with the TDMAT precursor as a function of deposition temperature.

5.3.2 Crystallinity

Crystalline TiO_x has been reported to be detrimental for passivation [17]. It is therefore important to check whether the TiO_x films are amorphous or not and whether they stay amorphous after annealing at 300 °C. To investigate this, both X-ray crystallography and Raman spectroscopy measurements have been performed on 5 nm thick TiO_x films deposited at temperatures ranging from 50 °C to 300 °C after they received a 2 hours forming gas anneal at 300 °C. Grazing incidence diffraction mode was used for the XRD measurement to make the measurement more surface sensitive.

From literature, the three crystal phases of TiO_x, anatase, rutile and brookite, have been reported to have characteristic XRD peaks at angles of respectively $2\theta = 25$ °[53], $2\theta = 27$ °[53] and $2\theta = 31$ °[54]. As Figure 5.11 shows, none of these peaks are visible in the XRD spectra, indicating an amorphous film. For Raman spectroscopy, it is reported that the anatase crystalline phase of TiO_x has a strong peak located at 143 cm^{-1} [55]. Strong peaks for rutile and brookite crystalline phase are reported at wavelengths of 445 cm^{-1} and 150 cm^{-1} [55] respectively. Figure 5.12 shows, besides the strong signal originating from the silicon spectrum of the substrate, none of these TiO_x peaks. The Raman measurements confirm therefore the amorphous character of the films.

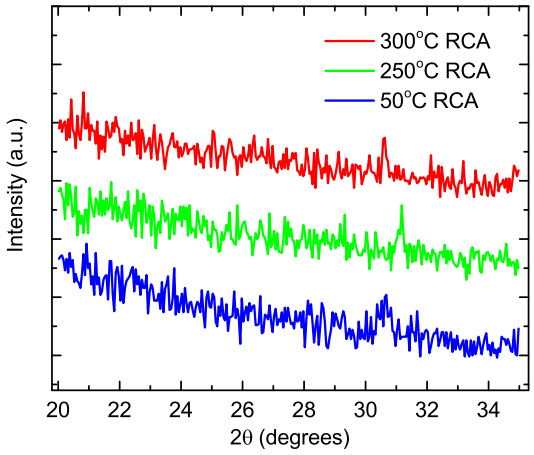

Figure 5.11: XRD scans of 5 nm TiO_x films deposited at different temperatures after 2 hours FGA. The absence of strong peaks indicates amorphous TiO_x.

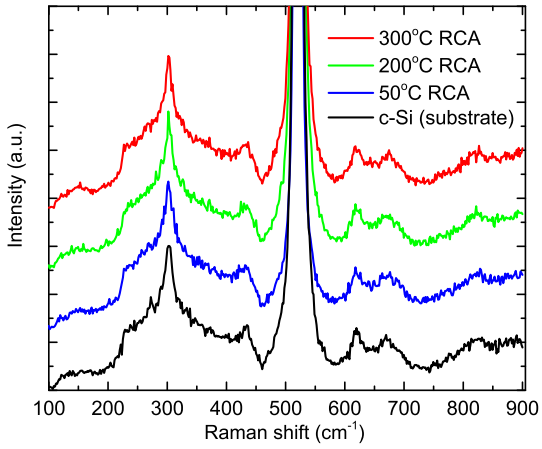

Figure 5.12: Raman spectra of 5 nm TiO_x films deposited at different temperatures after 2 hours FGA. Besides the strong silicon peaks, no peaks of crystalline TiO_x are present.

5.3.3 Stoichiometry

Figures 5.13 and 5.14 show the measured spectra and the deconvolution of the titanium Ti2p core level peaks and oxygen O1s core level peak for 5 nm TiO_x on HF-treated Si substrate obtained with XPS. The measured Ti spectra for different temperatures are nearly identical and indicate therefore no detectable differences in stoichiometry. A quantification of the stoichiometry is performed by using the ratio between the normalized area of the titanium Ti2p doublet peaks and the main

oxygen O1s peak at 529.9 eV. The oxygen peak as presented in Figure 5.14 consists of a main peak at 529.9 eV originating from oxygen bonded to titanium and a peak at 532 eV (forming a 'shoulder' on the higher binding energy side of the main oxygen peak) due to oxygen bonded to other elements. These other oxygen bonds could include OH-groups, C-O groups or oxygen bonded to silicon, the latter is then originating from a silicon oxide layer between the TiO_x and the silicon substrate. To determine whether these oxygen bonds are mainly OH- and C-O groups or whether it is oxygen originating from a silicon oxide layer, XPS is performed on a thicker (30 nm) TiO_x film. Since the penetration depth of XPS is only a few nanometers [50], a contribution from a silicon oxide layer to the oxygen spectrum is not possible for this film. No oxygen 'shoulder', so no peak at 532 eV is present for this thicker film, indicating that the peak at 532 eV in Figure 5.14 is originating from a silicon oxide interlayer and not from for example OH-groups. The results of stoichiometry determination is shown in graph 5.15. The graph shows, like the measured XPS spectra, no detectable difference in stoichiometry between different deposition temperature in the as-deposited state. Furthermore, the oxygen-to-titanium ratio is found to be about 1.9±0.1, while completely stoichiometric TiO_x has a ratio between oxygen and titanium of 2. It can thus be concluded that the films are almost stoichiometric films. The near stoichiometry of the films is further confirmed by the fact that the measured Ti2p peaks could be fitted well with only the Ti2p peaks with binding energies related to TiO_2.

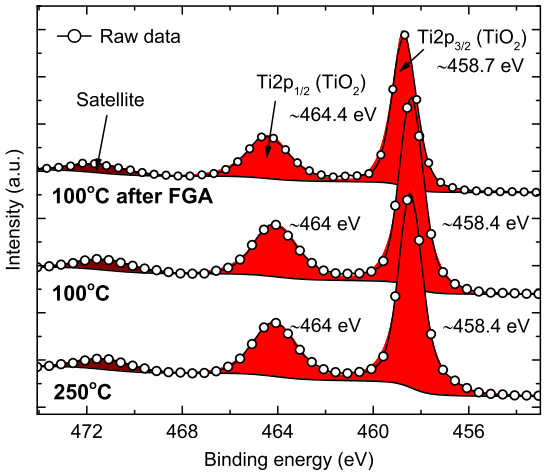

Figure 5.13: XPS scan of Titanium Ti2p doublet peaks of 5 nm TiO_x deposited at different ALD temperatures before and after FGA. A different ALD temperature or post-deposition FGA have no clear effect on the shape of the peaks.

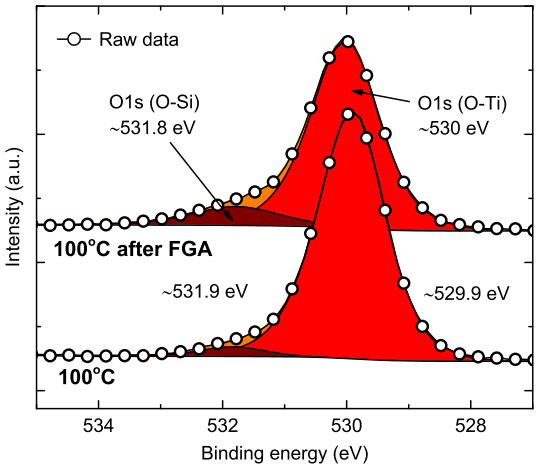

Figure 5.14: XPS scan of oxygen O1s peak of 5 nm TiO_x deposited at 100 °C before and after FGA. A post-deposition FGA results in more O-Si bonds: the SiO_x interlayer grows.

Figures 5.13 and 5.14 show also the titanium Ti2p core level peaks and oxygen O1s core level peak after 2 hours of forming gas anneal at 300 °C. The titanium peaks for the different deposition temperatures look still very similar. Concerning the oxygen spectrum, it can be seen that the shoulder on the higher binding energy side of the main oxygen O1s peak has grown upon annealing. The latter indicates more oxygen bound to silicon. Since the annealing takes place in a oxygen-depleted ambient, this suggests that the silicon reduces titanium oxide to form a silicon oxide interlayer (see Section 5.4 for more details). The reduction of TiO_x by Si can also be seen in the ratio of oxygen to titanium after annealing, which is slightly lower after annealing (see graph 5.15).

A second reason for the slightly lower ratio might be the reducing character of the hydrogen in the forming gas treatment.

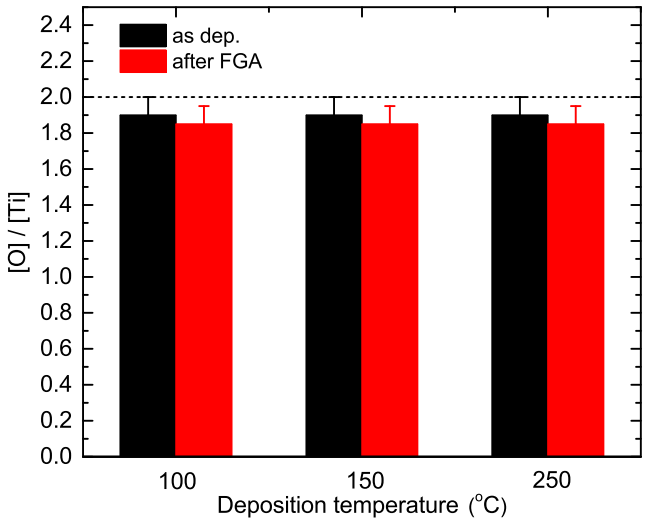

Figure 5.15: Ratio of oxygen (O) to titanium (Ti) of 5 nm TiO_x films deposited at various temperatures. No significant difference in stoichiometry is observed between different ALD growth temperatures. A slight oxygen reduction of the titanium is observed after a forming gas anneal at 300 °C of 2 hours.

5.3.4 Chemical impurities

X-ray photoelectron spectroscopy showed that the deposited TiO_x films contain besides elemental titanium and oxygen, very low levels of carbon and nitrogen. The carbon and nitrogen levels are below 2 and 1 atomic percentage respectively (see Figures C.1 and C.2 in Appendix C). These levels are close to the typical detection limit in an XPS measurement [56]. A forming gas anneal did not significantly change the content of nitrogen or carbon in the TiO_x films. It can be concluded that all the deposited TiO_x are very pure.

5.3.5 Electrical resistivity

The electrical resistivity is measured with a four-point-probe measurement. The measured resistance of the thin ($\leq$ 5 nm) TiO_x films proved to be similar to the internal resistance of the measuring device ($\approx$ 10 GΩ), indicating a resistivity that is too high to measure with the device. From these measurements only an order of magnitude can be given for the lower limit of the resistivity, which is in the order of 10^5 Ω·cm.

In an attempt to have a film resistance lower than the internal resistance of the four-point-probe, a thicker TiO_x film (30 nm) was investigated as well. This film was prepared by the same ALD recipe at a temperature of 200 °C. In the as-deposited state the film is found to be amorphous

with a similar stoichiometric and impurity content as the thinner films ($\leq$ 5 nm). Remarkably, the thicker layer resulted not only in a resistance lower than the internal resistance of the four-point-probe, but also in resitivity that is orders of magnitude lower in comparison to the thin ($\leq$ 5 nm) TiO_x films: 3.3 Ω·cm in the as-deposited state. This is an unexpected result since the thickness of the film only increased with a factor of six. The resitivity after 1 hour FGA reduced even to 0.12 Ω·cm. Note however that the thicker film becomes crystalline during the FGA and becomes therefore different from the amorphous thin films with regard to the crystal phase. About the reason for this remarkable discrepancy between the thick (30 nm) and the thin ($\leq$ 5 nm) films, only speculations can be made. One likely explanation would however be carrier depletion of the thin TiO_x films by absorbed species like oxygen or water. The latter phenomenon is for example used in resistance based gas sensors with TiO_x [57],[58],[59].

5.3.6 Optical properties

With the help of spectroscopic ellipsometry, the (optical) bandgap, refractive index and extinction coefficient of the TiO_x films have been deterimined. An overview of the bandgap and refractive index as a function of depostion temperature can be found in Figure 5.16. The bandgap is found to be about 3.3 eV, which is similar to other reported bandgaps of amorphous TiO_x: 3.36 eV reported by Abd El-Raheem et al. [60] (for TiO_x deposited by dc sputtering) and 3.26 eV to 3.29 eV reported by Zhang et al. [61] (for TiO_x deposited by pulsed bias arc ion plating). Furthermore, it is interesting to note that the bandgap show a slight but consistent decrease with ALD temperature.

The refractive index is found to increase slightly with the deposition temperature and has a value of about 2.3 at $\lambda = 600$ nm (see Figure 5.16). A large range of values for the refractive index of TiO_x is reported in literature ranging from 1.9 to 2.5 [61]. A reason for the variety of reported values for the refractive index of TiO_x is the well-established linear correlation between the refractive index and the density of TiO_x [62], [63], [64]. The difference in refractive index with ALD temperature as presented in this work is therefore likely to arise due to the preparation of denser films at higher ALD temperatures.

The extinction coefficient as a function of the photon energy is presented in Figure 5.17. A very low value for the extinction coefficient ($k < 0.1$) is found for photon energies lower than 3.5 eV, indicting the transparent character of TiO_x.

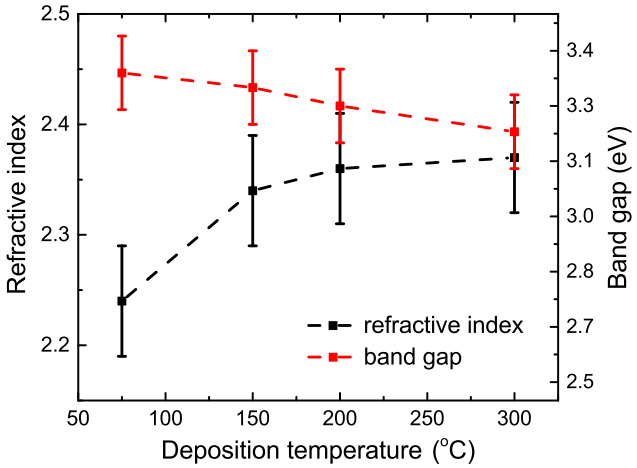

Figure 5.16: Refractive index and optical bandgap of TiO_x in the as-deposited state for various deposition temperatures.

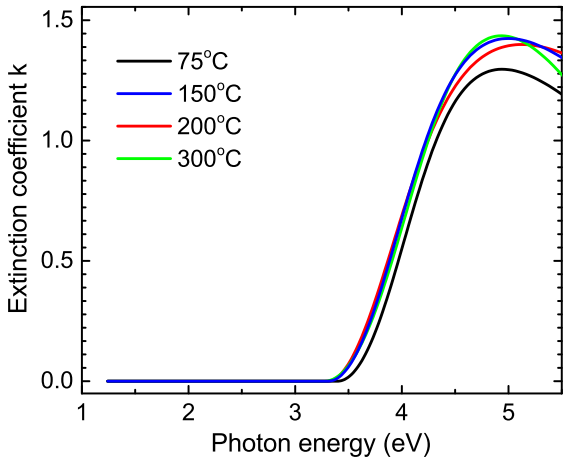

Figure 5.17: Extinction coefficient as a function of photon energy for different deposition temperatures of TiO_x. Only for high photon energies (> 3.3 eV) significant light absorption takes place.

With regard to the optical losses of a TiO_x layer in a solar cell application, the following can be concluded. When a transparent front contact configuration is considered consisting of a Si - TiO_x - TCO stack, a refractive index between the refractive index of silicon (n ≈3.9 [65]) and a typical TCO like indium tin oxide (n ≈ 1.8 [66]) is favorable. This condition results namely in low reflection losses at the TiO_x interfaces. The reported refractive index of 2.3 satisfies this conduction, which implies potentially low reflection losses at the TiO_x interfaces. Secondly, compared to other electron-selective contact materials like n-type amorphous silicon (a-Si:H(n)) or n-type polycrystalline silicon (n-poly-Si), the absorption coefficient α ($\alpha = \frac{4\pi k}{\lambda}$) of TiO_x is very low over nearly the whole photon energy range of the solar spectrum. This means that TiO_x has a relatively very low absorption of the incident sun light. It should be clear that with regard to optical losses in a solar cell application, TiO_x has excellent optical properties.

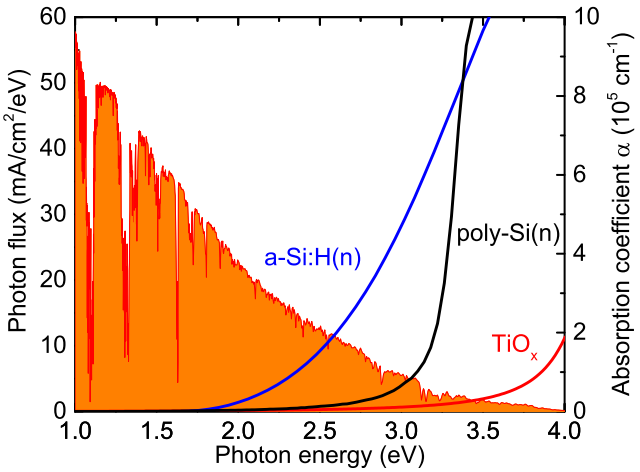

Figure 5.18: Absorption coefficients of n-type a-Si:H [67], n-type poly-Si [68] and TiO_x (deposited at 150 °C) as a function of photon energy. The orange area in the figure shows the AM 1.5G solar spectrum.

5.4 Si-TiO_x interface

As mentioned in the experimental setup, three different Si - TiO_x interfaces were prepared by applying three different surface treatments of the silicon substrate: HF-cleaning, RCA-cleaning and nitric acid oxidation (NAOS). The first treatment results in a H-terminated silicon surface and the latter two form a few nanometers of silicon oxide on top of the silicon substrate. This section investigates several properties of these interfaces: the presence of a SiO_x interlayer, the thickness of the SiO_x, the stoichiometry of the SiO_x layer and changes of these properties upon annealing.

5.4.1 Effect of the Si surface pre-treatment on the Si - TiO_x interface

Figure 5.19 shows an XPS scan of the binding energies between 97 eV and 104 eV for all three interfaces in the as-deposited state. In this energy range two peaks are visible. On the right ($\approx$ 98 - 100 eV) a large doublet peak is visible; this peak is originating from Si-Si bonds, hence from the c-Si substrate. The smaller peak on the left ($\approx$ 100 - 103 eV) is originating from Si-O bonds, hence from the silicon oxide interlayer. Both RCA and NAOS pretreated Si surfaces show clear peaks around 102.4 eV an 101.8 eV respectively, indicating the presence of a substantial SiO_x interlayer. Spectroscopic ellipsometry revealed for both SiO_x layers a thickness of about 1.5 nm. The ratio of the normalized area of the SiO_2 peak (dark red colored peak, indicated by the label 'Si2p (Si-O)' in Figure 5.19) and bulk Si peak (red colored doublet peaks, indicated by the labels '$Si2p_{1/2}$ (Si-Si)' and '$Si2p_{3/2}$ (Si-Si)' in Figure 5.19) can be seen as qualitative measure for both density and thickness of the silicon oxide layer (see Section 5.2.6). For both NAOS and RCA oxide this ratio is about 0.3. Together with the SE results it can therefore be concluded that both interlayers have a similar thickness and density. Although small, the HF-treated silicon shows a silicon oxide peak too. It can thus be concluded that the thermal ALD process of TiO_x grows a SiO_x interlayer, something that was earlier suggested by Scheerder et al. [33]. The ratio between the silicon oxide peak and the main Si2p peak is only 0.1, indicating a thin and/or sparse silicon oxide. Ellipsometry measurements estimate the silicon oxide layer to be about 0.7 nm thick.

The higher the oxidation degree of silicon, the higher the binding energy of the silicon oxide peak. The difference in binding energy between the Si2p silicon oxide peak and the main Si2p peak (indicated by 'ΔE_B' in Figure 5.19) is therefore a measure of the stoichiometry of the silicon oxide. With regard to the stoichiometry of the formed silicon oxide interlayers, the following is observed. For both RCA and NAOS ΔE_B is about 3.3 eV, indicating no significant differences in stoichiometry between both oxides. Completely stoichiometric silicon oxide has a ΔE_B of about 3.9 eV [69]. It can therefore be concluded that both the RCA and NAOS oxides are slightly sub-stoichiometric. For the HF-treated silicon, ΔE_B is about 2.8 eV. The silicon oxide is thus less stoichiometric than the RCA and NAOS oxides.

In addition to these findings, XPS revealed that the thickness of the TiO_x film influences on the properties of the SiO_x interlayer formed on HF-cleaned Si. Figure 5.21 suggests that the thinner the TiO_x film, the thicker and more stoichiometric the silicon oxide interlayer that is formed during the ALD deposition of the TiO_x. The reason for this behavior is not well understood, but might be attributed to post deposition oxidation of the silicon surface by oxygen or moisture diffusing from the atmosphere through the TiO_x to the silicon surface. Thinner films may form a smaller barrier for the oxygen and moisture diffusion, which therefore leads to a higher degree of silicon oxidation.

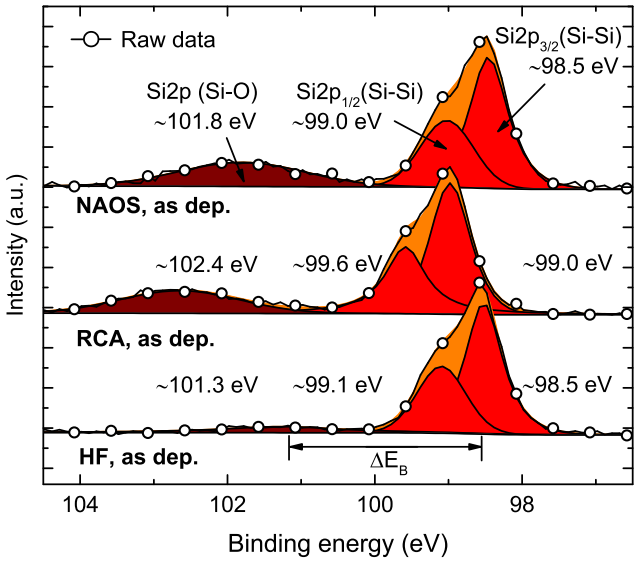

Figure 5.19: XPS scan of silicon Si2p peak for different pre-treatments of the silicon substrate in the as-deposited state after TiO_x deposition at 150 °C. Both RCA and NAOS treatments of the Si surface results in a substantial SiO_x interlayer, while in the case of HF-cleaned silicon only a very thin and/or sparse SiO_x layer appears to be present.

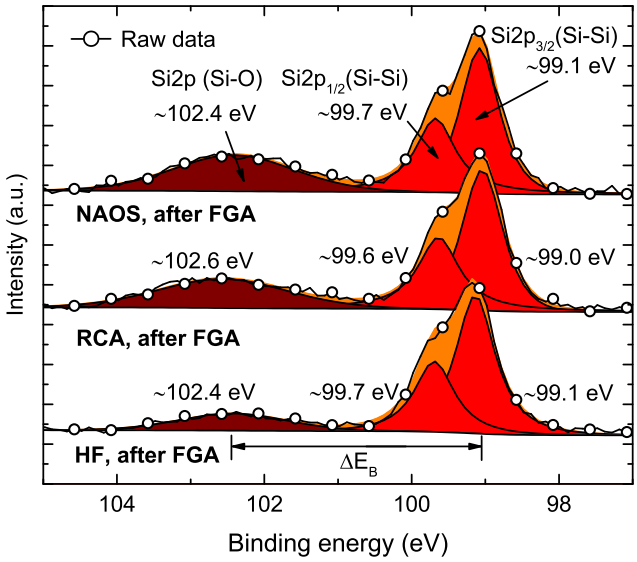

Figure 5.20: XPS scan of silicon Si2p peak for different pre-treatments of the silicon substrate after TiO_x deposition at 150 °C and 2 hours FGA at 300 °C. All SiO_x interlayers have become thicker and/or more dense, especially the SiO_x interlayer on HF-cleaned Si.

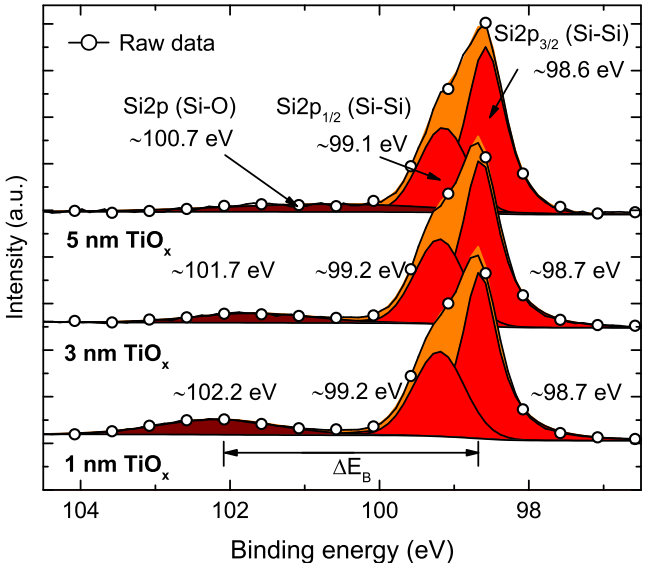

Figure 5.21: XPS scan of silicon Si2p peak for different TiO_x film thicknesses in the as-deposited state after TiO_x deposition at 200°C on bare silicon. The thicker the TiO_x film, the thinner and/or less dense the SiO_x interlayer.

5.4.2 Effect of forming gas anneal on the Si - TiO_x interface

For RCA and NAOS, annealing does not affect ΔE_B (see Figure 5.20), which means that the stoichiometry of the RCA and NAOS oxides remains unchanged. Both silicon oxide layers seem however to grow and/or become more dense upon annealing since both oxides show an increase in the area ratio of the silicon oxide peak and the bulk Si peak (from 0.3 to 0.42 and 0.37 for NAOS and RCA, respectively). The HF-treated silicon shows the largest increase of the silicon oxide peak. The ratio of the silicon oxide peak and Si bulk peak increases from 0.1 to 1.17, indicating a substantially thicker and/or more dense silicon oxide interlayer (see also Figure 5.22). Transmission electron microscopy (TEM) analysis of the interface formed between HF-cleaned silicon and TiO_x is shown in Figure 5.23. The TiO_x is deposited at 200 °C and the sample is consequently annealed at 200 °C. This figure confirms the presence of a substantial silicon oxide interlayer, which is visible as a dark gray region. Based on the TEM image, the silicon oxide interlayer is estimated to be 0.9±0.1 nm thick.

Another important change of the HF-cleaned silicon interface after annealing is the change of ΔE_B. The latter increases from 2.6 eV to 3.3 eV. This value of ΔE_B = 3.3 eV is similar to the RCA and NAOS oxide and means a more stoichiometric silicon oxide interlayer after annealing. The oxygen needed for the formation of this supposedly thicker and more stoichiometric silicon oxide interlayer is probably coming from the TiO_x since this is the only source of oxygen during the anneal treatment. The TiO_x shows a slight decrease in stoichiometry after annealing, which provides support for this assumption (see Figure 5.15). It can thus be stated that a post deposition anneal can significantly increase the silicon oxide interlayer thickness, density and stoichiometry, especially for HF-cleaned silicon. The oxygen needed for these changes is presumed to originate form the TiO_x layer, which is subsequently reduced.

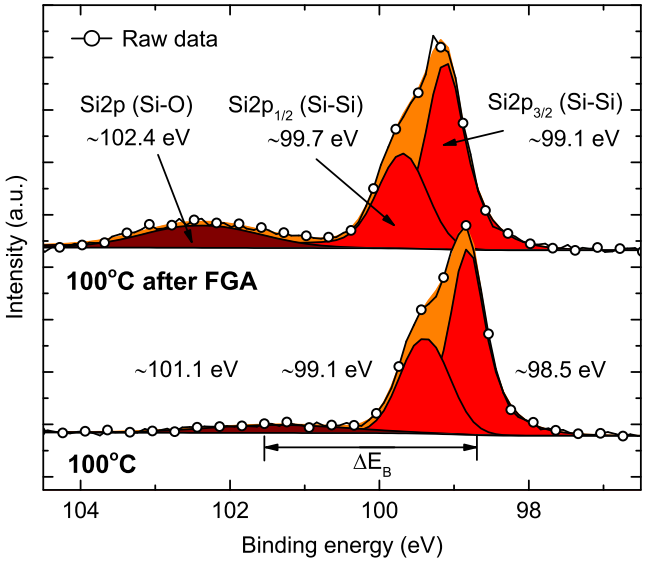

Figure 5.22: XPS scan of silicon Si2p peak after TiO_x deposition at 100°C on HF-cleaned silicon before and after a 2 hours forming gas anneal at 300°C. A clear increase of the thickness and density of the SiO_x interlayers observed.

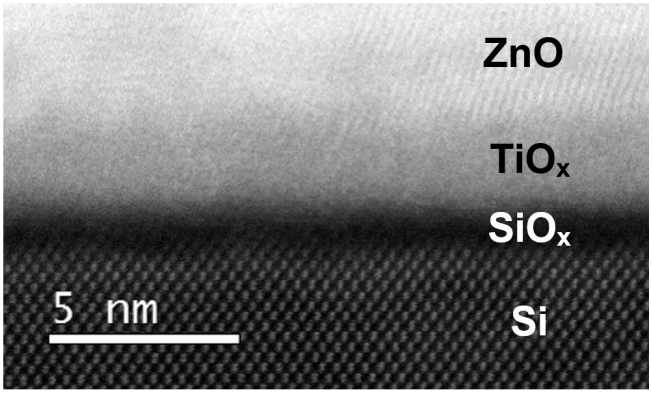

Figure 5.23: Transmission electron microscopy cross section (High Resolution Scanning TEM mode) of the Si-TiO_x interface for a TiO_x film deposited on bare silicon (HF-treated) at a temperature of 200°C after annealing at 200°C. The SiO_x layer thickness is estimated to be 0.9±0.1 nm and the TiO_x layer 2.5±0.1 nm. The substantial SiO_x interlayer observed in XPS after FGA (see Figure 5.22) is confirmed by this TEM cross section.

5.5 Passivation

In the previous two chapters, several material properties of TiO_x and the interface between Si and TiO_x have been investigated. This was done for different TiO_x thicknesses, different deposition temperatures of TiO_x and different surface treatments of the Si substrate. The current section discusses the passivation properties of these layers. Whenever possible, the passivation results are correlated to the observed material and interface properties of TiO_x. Furthermore, this section discusses the role of a post-deposition FGA on the passivation and the role of field-effect passivation is addressed.

5.5.1 Anneal treatment

Figure 5.24 demonstrates that post-deposition annealing at 300 °C of 5nm TiO_x deposited at 200 °C results in a large increase of the c-Si surface passivation: from $\tau_{eff} < 70$ μs to $\tau_{eff} > 600$ μs. The other TiO_x films which are investiagted in this work also show this increase: all as-deposited films show effective lifetimes of $\tau_{eff} < 80$ μs (see Figure A.1 in Appendix A), while a forming gas anneal at 300 °C increase this effective lifetime beyond $\tau_{eff} = 1$ ms (see Figure 5.25), which is a high level of passivation compared to the results in literature (see literature overview of Chapter 4). These results confirm that annealing is key to reach high passivation levels [17], [18], [19], [33]. The FGA (nitrogen-hydrogen atmosphere) is found to provide a larger improvement in passivation than pure nitrogen. One reason for this could be a reduced diffusion of hydrogen out of the film TiO_x by the higher hydrogen concentration in the annealing ambient. A second possibility may be additional hydrogen incorporation in the TiO_x from the FGA ambient. Annealing also influences the interfacial silicon oxide layer between the Si and TiO_x film. The consequences of these differences on the passivation quality are discussed in the next section.

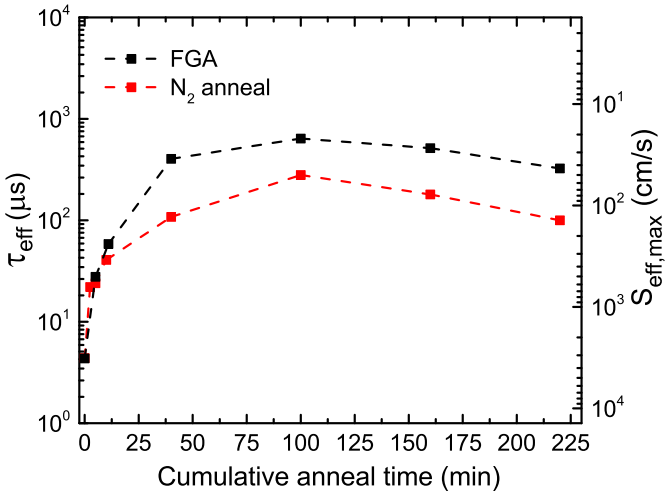

Figure 5.24: The effective minority carrier lifetime (left axis) and surface recombination velocity (right axis) of 5 nm TiO_x on HF-cleaned Si as a function of anneal time. The passivation quality improves upon annealing at 300 °C in both nitrogen and nitrogen-hydrogen ambient (FGA). FGA treatment shows a larger increase in lifetime.

5.5.2 Interfacial oxide and deposition temperature

The c-Si surface passivation as a function of TiO_x deposition temperature and silicon surface treatment can be seen in Figure 5.25. The figure presents the effective lifetime and effective surface recombination velocity after FGA. Two different silicon oxide interlayers are compared: a silicon oxide formed during a RCA clean and a silicon oxide formed by NAOS. From Figure 5.25 it is clear that the RCA oxide performs for all deposition temperatures better than the NAOS oxide. The RCA oxide reaches a maximum lifetime of $\tau_{\text{eff}} = 1.28$ ms (with $S_{\text{eff,max}} = 10.9$ cm/s and $J_0 = 25$ fA/cm^2). The NAOS oxide reaches a maximum of $\tau_{\text{eff}} = 450$ μs (with $S_{\text{eff,max}} = 31.1$ cm/s and $J_0 = 63.5$ fA/cm^2).

Figure 5.25 shows that TiO_x deposited on bare silicon (HF) can provide good surface passivation, when a relatively low deposition temperatures are used. TiO_x deposited on bare silicon yields lifetimes as high as $\tau_{\text{eff}} = 1.3$ ms. The surface recombination velocity and recombination current density are $S_{\text{eff,max}} = 10.7$ cm/s and $J_0 = 21.7$ fA/cm^2, respectively. The effective lifetime dependence on the deposition temperature is for this interface much larger than it is for the RCA and NAOS silicon oxide interlayers. Regarding the importance of the silicon interface for the passivation, it can be understood that an interface formed during the ALD growth has a much stronger dependence on the deposition process than an interface formed prior to deposition as is the case for the silicon oxide interface formed by RCA and NAOS (as illustrated in Section 5.4). Apparently, low deposition temperatures allow the ALD process to form a good passivating interface between the silicon and the titanium oxide. Furthermore, Figure 5.26 shows that this interface is fragile: annealing TiO_x films deposited at low temperatures (50 °C) leads to a large increase of the passivation at the start, but when the annealing is continued a strong decrease in lifetime is observed. Both RCA and NAOS interfaces show less deterioration of the passivation quality upon exposure to high temperatures for extended times (see Figure 5.27). Yang et al. [18] also found an increase in thermal stability of the passivation of TiO_x on a thermal silicon oxide interlayer compared to TiO_x on HF-cleaned silicon. The deterioration of the passivation of TiO_x on HF-cleaned Si might be attributed to the growth of the interfacial silicon oxide interlayer upon annealing (see Section 5.4). This interlayer formation involves a complete reconstruction of the silicon-titanium interface (i.e. formation of Si-O bonds and breakage of Ti-O bonds), which may lead to the formation of additional defects accompanied with hydrogen loss, when growing TiO_x at higher substrate temperatures.

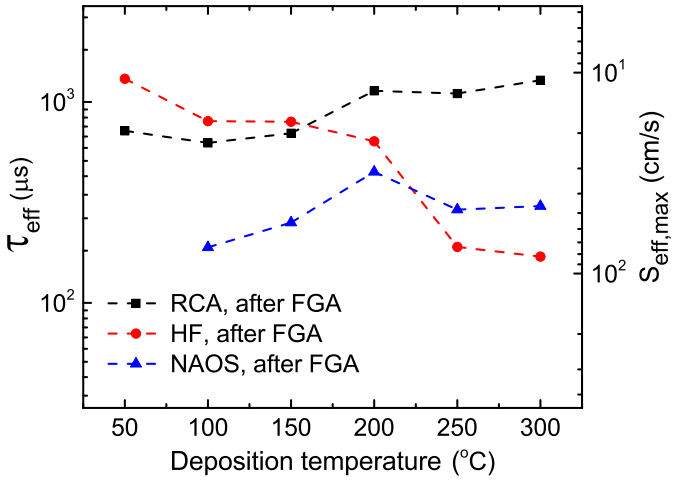

Figure 5.25: The effective minority carrier lifetime (left axis) and surface recombination velocity (right axis) for RCA, HF and NAOS pre-treated silicon wafers with 5 nm TiO_x deposited at temperatures ranging from 50 °C till 300 °C after forming gas annealing (see Appendix A for the used anneal times and for the effective lifetimes in the as-deposited state).

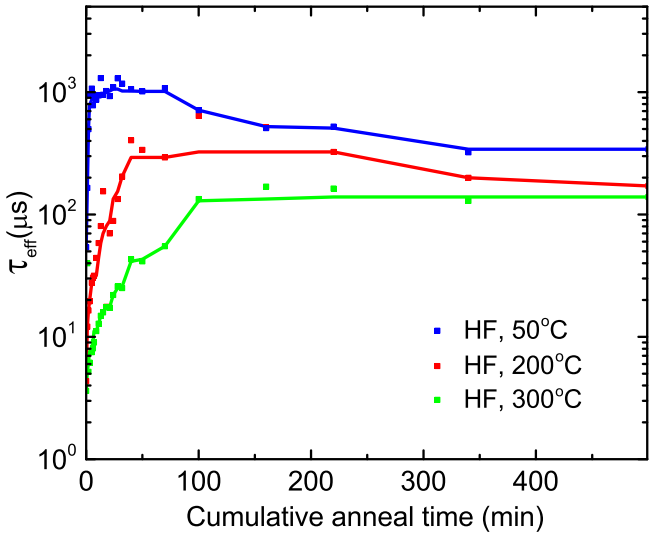

Figure 5.26: The effective minority carrier lifetime as a function of the ccumulative anneal time for different ALD temperatures of TiO_x on HF-cleaned silicon (FGA at 300 °C). The data are represented by the colored symbols, while the solid lines serve as guides to the eye.

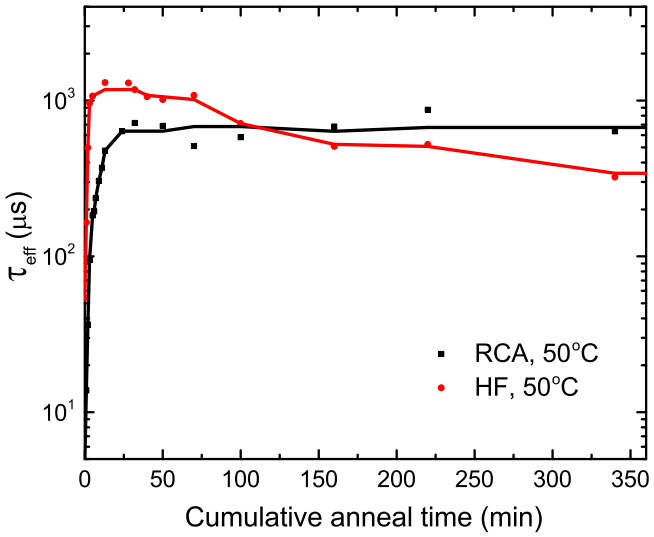

Figure 5.27: The effective minority carrier lifetime (left axis) and surface recombination velocity (right axis) as function of the cumulative anneal time for different ALD growth temperatures of TiO_x on HF-cleaned silicon and RCA-cleaned silicon (FGA at 300 °C). The data are represented by the colored dots, while the solid lines serve as guides to the eye.

TiO_x films in combination with and silicon oxide interlayer formed prior to ALD (RCA oxide or NAOS oxide) show an increase of the lifetime with deposition temperature. An explanation for this behavior could be the formation of denser TiO_x films as suggested in Section 5.2.5. A denser film can form a higher barrier for hydrogen, therefore denser films may keep more hydrogen in the NAOS or RCA silicon oxide interlayer and more dangling bonds can be hydrogenated, hence explaining the higher level of chemical passivation. For the TiO_x films deposited on bare silicon (HF), the ALD process does not only grow a TiO_x film, but also a silicon oxide interlayer (see Section 5.4). The latter distinguishes the HF-cleaned silicon from RCA and NAOS treated silicon and could explain the different trend with ALD temperature: a strong decrease of the passivation level with deposition temperature. For HF-cleaned Si, a low temperature seem to establish a better passivating Si - SiO_x - TiO_x interface than higher ALD temperatures.

5.5.3 Film thickness

The effective lifetime as a function of TiO_x thickness can be seen in Figure 5.28. The TiO_x films are deposited at 200°C on HF-cleaned silicon. An optimum in passivation is found for a 3 nm TiO_x capping layer. Such an optimum is in contrast with the monotone increase of the passivation reported by most papers for TiO_x on HF-cleaned Si [70],[19], [18],[31]. Although the differences of the SiO_x interlayer with TiO_x film thickness (see Section 5.4) are suspected to play a role in the thickness optimum, the physical mechanism that is responsible for the thickness optimum in lifetime remains unclear for now

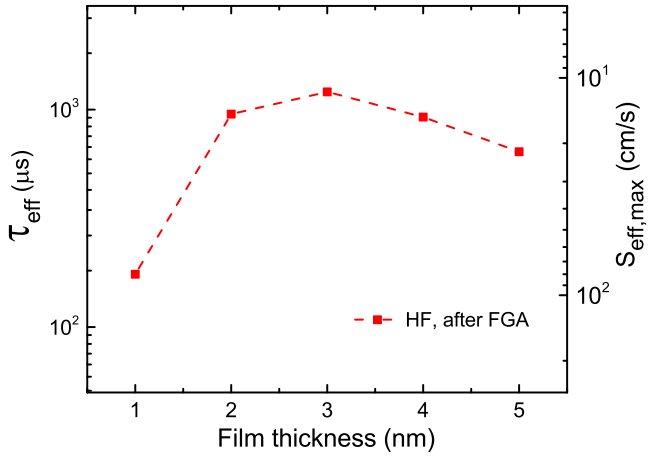

Figure 5.28: The effective minority carrier lifetime (left axis) and surface recombination velocity (right axis) as function of the TiO_x film thickness after annealing (see Appendix A for the used anneal times and for the effective lifetimes in the as-deposited state). A strong thickness dependence is found with an optimum of $\tau_{eff} = 1.2$ ms and $S_{eff,max} = 11.6$ cm/s around 3 nm.

5.5.4 c-Si band bending

To investigate the passivation mechanism of TiO_x, surface photo voltage (SPV) measurements have been carried out by dr. M. Bivour from the Fraunhofer Institute for Solar Energy Systems (Freiburg, Germany) on n- and p-type silicon substrates (ρ = 1-5 Ω·cm) with a TiO_x film deposited on one side. This technique makes it possible to measure the band bending in the silicon substrate near the Si-TiO_x interface induced by the TiO_x. An overview of the measured band bending in both n- and p-type silicon substrates in the as-deposited state is presented in Figure 5.29. A high degree of upward band bending in the n-type silicon (0.8 - 0.9 eV) is observed and a relatively small downward band bending (0.1 - 0.3 eV) in the p-type silicon. Although the values shows some differences, all tested conditions in Figure 5.29 show a large upward band bending in n-type silicon and relatively small bending in p-type silicon. After annealing, the differences in band bending decrease for different Si-TiO_x interfaces (HF or RCA), TiO_x film thicknesses (3 or 5 nm) and TiO_x deposition temperature (50 °C and 300 °C), as can be seen in Figure 5.29. The band bending is virtually independent of the type of Si-TiO_x interface or TiO_x film properties. After FGA an upward bending on n-type Si of about 0.86 eV is observed and a downward bending on p-type Si of about 0.13 eV.

The observed band bending is very similar to the 0.8-0.9 eV upward band bending on n-type Si observed for thermal ALD TiO_x by Matsui et al. [20]. Matsui et al. also reported upward band bending for plasma enhanced ALD TiO_x of about 0.4 eV. Another report that suggests upward band bending in the silicon is reported for light soaked thermal ALD TiO_x [17]. Regarding all these observations from literature together with the observations in this study, it seems that TiO_x induced upward band bending in n-type silicon is not uncommon. A possible explanation for the band bending could be net fixed negative charge in the TiO_x itself and/or at one of the interfaces (e.g. Si/SiO_x, SiO_x/TiO_x or TiO_x/air). The origin of the induced band bending is however not clear yet.

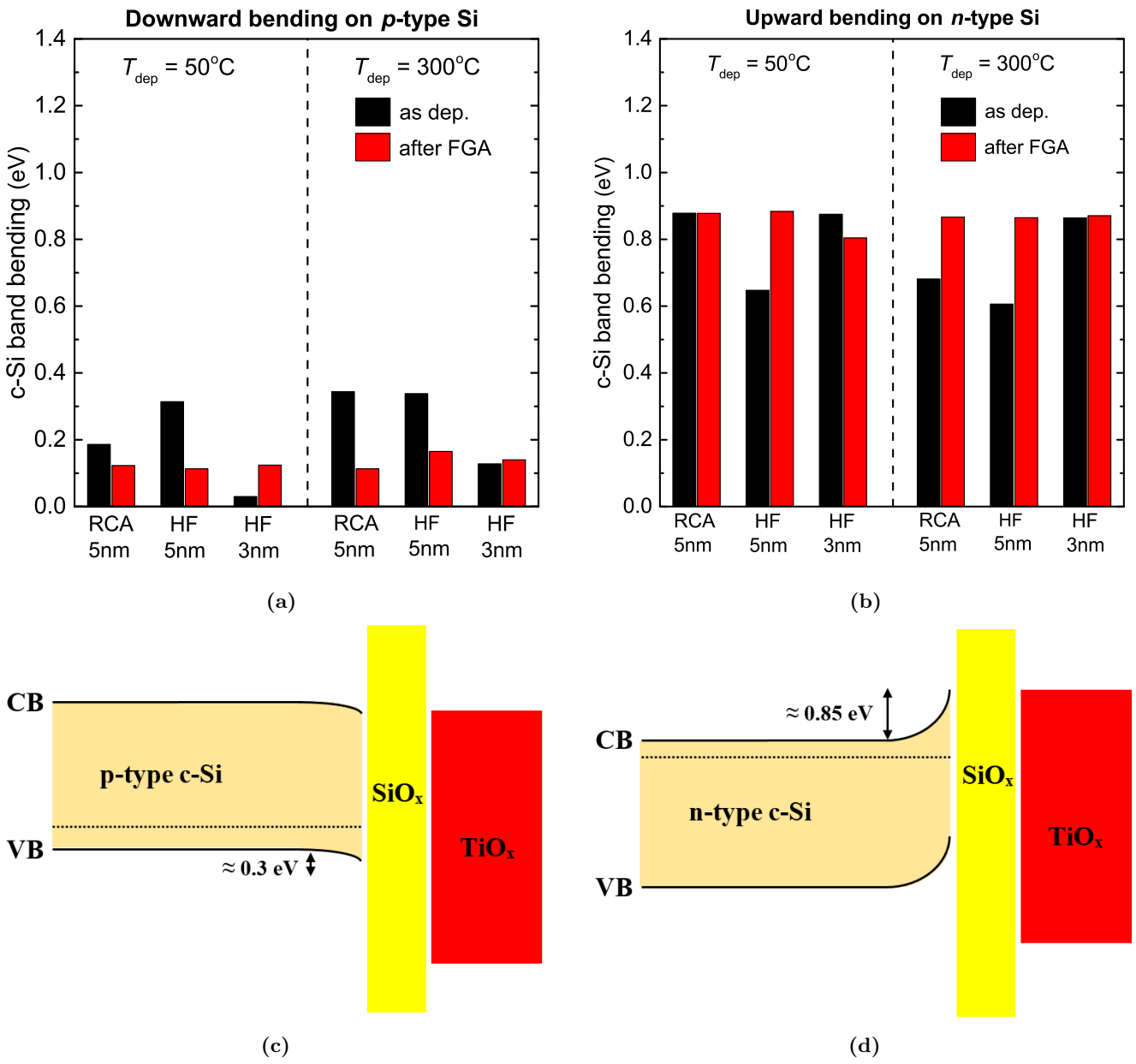

Figure 5.29: (a): Downward band bending in a p-type Si substrate induced by the TiO_x capping layer. Different TiO_x capping layers have been investigated: 3 and 5 nm thick TiO_x films, deposited at both 50 °C and 300 °C. Furthermore, the Si substrate is treated in two different ways prior to TiO_x deposition: a RCA clean or HF clean.
(b): Upward band bending in a n-type Si for the same mentioned TiO_x films and Si surface treatments.
(c,d): A schematic representation of the silicon band bending. The conduction and valence band of the silicon are indicated by CB and VB respectively. The dashed line represents the Fermi level in the silicon. Since the origin of the band bending is not clear yet, the conduction and valence band of the SiO_x and TiO_x layers are not shown.

5.5.5 Passivation mechanism

With regard to the passivation of the TiO_x films presented in this work, three conclusions can be drawn from the observed Si band bending after FGA (see 5.29). First off all, the large upward band bending of 0.86 eV means that there is a substatial depletion of the electrons near the c-Si(n) surface, from which it can be concluded that the surface passivation provided by TiO_x has a significant contribution from field-effect passivation. Secondly, after FGA, no significant differences are observed in Si band bending between different TiO_x film thicknesses, interfacial oxides or TiO_x deposition temperatures; i.e. the field-effect passivation is similar for all tested conditions. The observed differences in passivation quality of these conditions can therefore not be attributed to a different field-effect passivation. The differences in passivation quality after FGA have therefore to be mainly related to different chemical passivation. Thirdly, FGA does only induce a small difference in the Si band bending, suggesting that the large increase in passivation after FGA is not the result of an increasing field-effect passivation, but an improved chemical passivation.

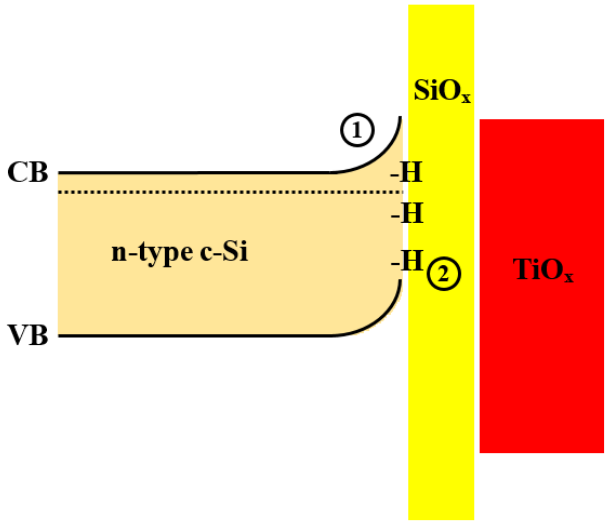

Figure 5.30: Schematic representation of the passivation of n-type c-Si by a few nm TiO_x after FGA. The conduction and valence band of the Si are indicated by CB and VB, respectively. The dashed line represents the Fermi level in the Si. The passivation has a contribution from field-effect passivation (1) and chemical passivation (2). Since the origin of the band bending is not clear yet, the conduction and valence band of the SiO_x (always present) and TiO_x layers are not displayed.

With regard to the chemical passivation of TiO_x, two interesting suggestions can be made. In Section 5.4 it is shown that there is always a SiO_x layer present between the c-Si and the TiO_x. Furthermore, large differences in passivation quality are shown as function of this SiO_x interlayer (see Figure 5.25), which could not be attributed to differences in field-effect passivation (see Figure 5.29). The SiO_x is thus believed to play an important role in the chemical passivation of c-Si by means of establishing an interface with low defect density. Secondly, an important mechanism for the improved chemical passivation is assumed to be the neutralization of Si dangling bonds by hydrogenation [22] (see Section 2.3). A sufficiently high hydrogen content near the Si interface is important for effective hydrogenation. A denser TiO_x film may keep more hydrogen near the

Si interface during annealing, which could explain the higher passivation level of the denser TiO_x films prepared by higher deposition temperatures. Decreasing the hydrogen diffusion out of the TiO_x in the atmosphere by increasing the hydrogen content of the atmosphere is another way of keeping more hydrogen near the interface during annealing. The latter could explain the higher passivation levels that are obtained when adding hydrogen to the annealing atmosphere (see Figure 5.24). A schematic overview of the assumed passivation mechanism of c-Si by TiO_x is shown by Figure 5.30.

5.6 Contact resistivity

This section discusses the contact resistivity (ρ_c) of TiO_x for different film thickness, ALD growth temperature and post-deposition FGA. The results are correlated to the observed material and interface properties of TiO_x.

5.6.1 ALD deposition temperature

The contact resistivity of 5 nm thick TiO_x films deposited at different ALD temperatures is summarized in Figure 5.31. The contact resistivity for the TiO_x films in the as-deposited state is presented by the black data points. The lowest contact resistivity in as-deposited state is found to be 0.027 $\Omega{\cdot}cm^2$ for a deposition temperature of 75 °C , which is low compared to the critical value of 0.1 $\Omega{\cdot}cm^2$, but also when compared to the values reported for other 5 nm thick films combined with aluminum as contact material (see literature overview in Table 4.2). For the higher deposition temperatures, the contact resistivity is well above the critical value of 0.1 $\Omega{\cdot}cm^2$ (see Section 2) and the values for deposition temperatures higher than 150 °C become unacceptably high (up to 10 $\Omega{\cdot}cm^2$) for solar cell application (see Figure 2.2). From Figure 5.32a, it becomes clear that in the as-deposited state, higher deposition temperatures show more rectifying behavior. This indicates the presence of a carrier depletion region in the silicon (see Section 2.4) causing a highly resistive contact.

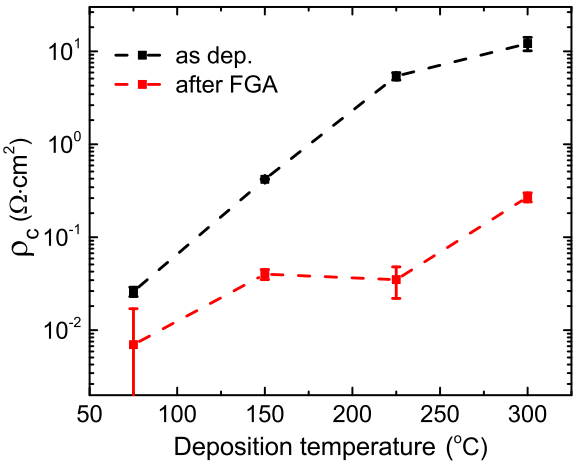

Figure 5.31: Contact resistivity versus the TiO_x deposition temperature for 5 nm thick TiO_x films.

The contact resistivity after annealing is presented by the red data points in Figure 5.31. Each sample has received a forming gas anneal treatment for a duration that is optimum for the passivation of that layer. This means that the anneal time of each sample is different (see Appendix B for the anneal times). The contact resistivity after annealing decreases for all deposition temperatures and especially for the high deposition temperatures: nearly two orders of magnitude. The large improvements upon annealing are also reported in literature by Yang et al. [18] and Allen et al. [19]. From Figure 5.32b, it seems that the large improvements can be attributed to the transition

from rectifying to Ohmic contact behavior (see Figure 5.32b). This indicates the reduction of a carrier depletion region in the silicon. A more elaborated discussion will follow in Section 5.6.3.

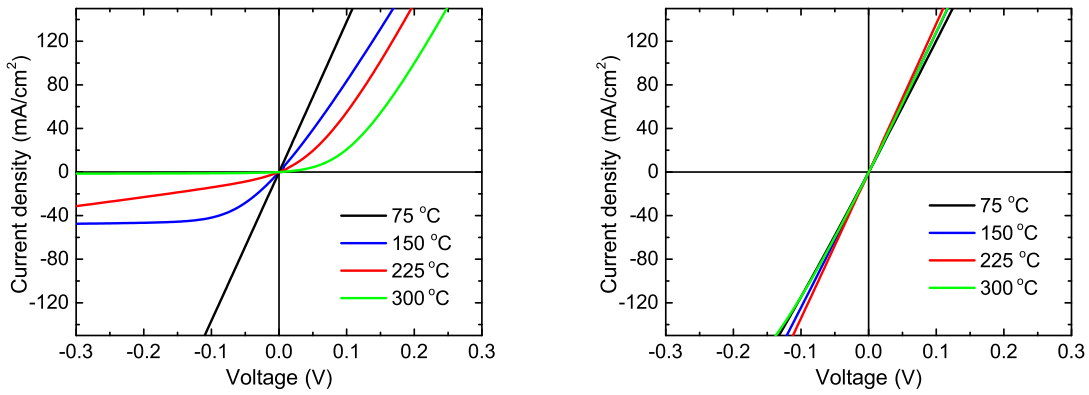

Figure 5.32: Left: The measured J-V characteristics plotted for different deposition temperatures of TiO_x in the as-deposited state (deposition temperature is 200 °C). Higher deposition temperatures show more rectifying behavior, indicating the presence of a depletion region in the TiO_x and/or Si. Right: The measured J-V characteristics plotted for different deposition temperatures of TiO_x after FGA, all ALD temperatures show Ohmic behaviour.

5.6.2 Film thickness

The contact resistivity as a function of the TiO_x film thickness for an intermediate ALD growth temperature of 200 °C is presented in Figure 5.33. The associated J-V curves can be found in Figures 5.34a and 5.34b. A 1 nm thick TiO_x layer between the silicon and aluminum leads to a contact resistivity value that is in the order of 10^{-5} $\Omega \cdot cm^2$, which is extremely low. For increasing TiO_x film thickness, the contact resistivity increases with orders of magnitude, which is also seen by Yang et al. [18]

An explanation for the increase of the contact resistivity with thickness can be derived from the J-V curves of Figure 5.34a. The J-V curves presented in Figure 5.34a show a relatively small decrease in forward bias current densities (the slope of the J-V curve in the linear regime for Voltage > 0 V) for different TiO_x thicknesses, indicating that the resistance of the TiO_x interlayer is not limiting. In contrast to the forward bias current density, the reverse bias current densities (Voltage < 0 V) changes substantially with thickness, indicating a larger potential barrier at the Si - TiO_x interface. From these two observation it can be concluded that the increase in contact resistivity with TiO_x thicknesses is mainly caused by an increase in the potential barrier at the Si - TiO_x interface; i.e. a stronger carrier depletion of the Si at the interface. A forming gas anneal (see Appendix B for the anneal times) leads to a reduction of the contact resistivity, especially for the thicker layers. The latter shows a decrease of more than two orders of magnitude. This decrease in contact resistivity is accompanied by a transition from rectifying to Ohmic contact behavior (see Figure 5.34b). This indicates a decrease of the carrier depletion region in the Si, which will be discussed in more detail in the next section.

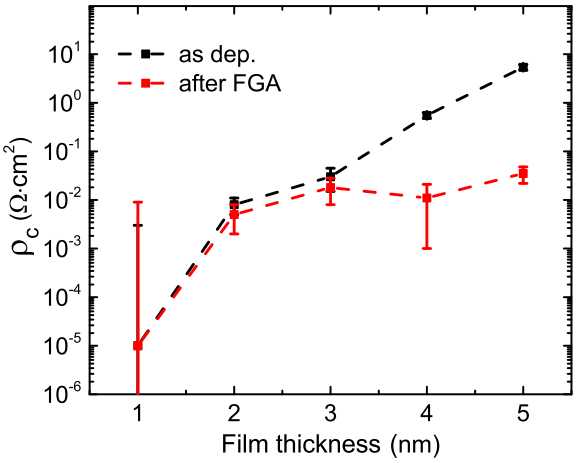

Figure 5.33: Contact resistivity vs the TiO_x film thickness for the ALD temperature of 200 °C.

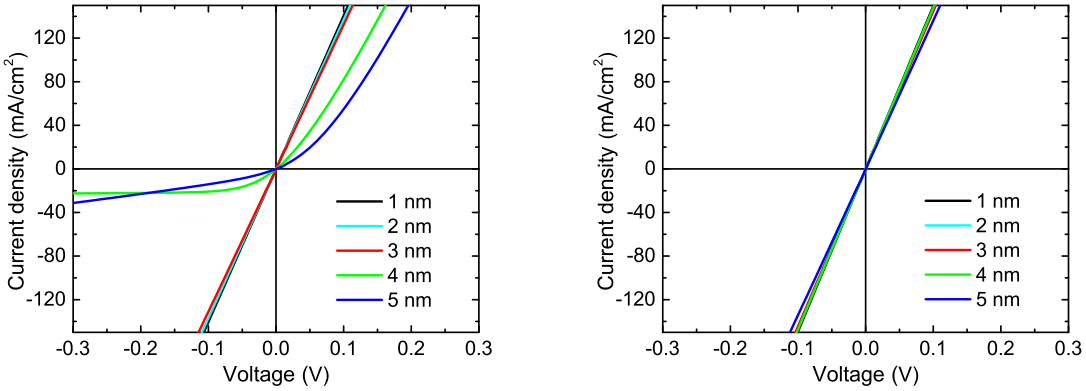

(a) **(b)**

Figure 5.34: Left: The measured J-V characteristics plotted for different TiO_x film thicknesses in the as-deposited state (deposition temperature is 200 °C). Higher deposition temperatures show more rectifying behavior, indicating the presence of a depletion region in the TiO_x and/or Si. Right: The measured J-V characteristics plotted for different TiO_x film thicknesses after FGA, all TiO_x thicknesses show Ohmic behaviour.

5.6.3 Discussion

The contact resistivity of semiconductor/metal and semiconductor/interlayer/metal stacks concerns many semiconductor devices and is therefore an important field of research. The topic proves however to be very complicated. Multiple studies have been performed to unravel the underlying physics of these contact structures [28], [40], [26], [71], [27], [25]. Yet there are many things still unknown and uncertain. In this section an attempt is made to explain some of the contact behavior observed in this work. Considering the difficulty of this topic it is not the intention to

make firm claims. Instead, this section is only intended as a contribution to the discussion about the contact resistivity of a c-Si/ TiO_x/Al stack for solar cell applications [18], [19], [20].

Band diagrams of contact structures provide a good way to explain the contact J-V behavior. An example of a possible band diagram for the Si - TiO_x - Al contacts used in this work is presented in Figure 5.35. For the contact resistivity, there are two important factors: the potential barrier at the Si - TiO_x interface (R_{Si}, characterized by Φ_{Si-TiO_x} and W in Figure 5.35. Note that R_{Si} is not a simple Ohmic resistance, it only indicates resistance.), and the resistance of the SiO_x and TiO_x interlayer (R_{Ins} in Figure 5.35).

In Section 5.6.2 it is explained that, in the as-deposited state, the potential barrier at the Si - TiO_x interface (Φ_{Si-TiO_x}) seems to be more important for the contact resistivity than the resistance of the SiO_x and TiO_x interlayers (R_{Ins}). In the ideal case (without the effects of interface states), Φ_{Si-TiO_x} is predicted by the Schottky-Mott rule (see Section 2.4). In reality however, the interface states at the Si - SiO_x - TiO_x and TiO_x - Al interfaces induce dipoles that give rise to additional potential barriers (indicated by the + and - signs at the interface in Figure 5.35). An expression for Φ_{Si-TiO_x} that takes these interface effects into account is presented by Gupta et al. [28]. This expression is a complex function. For the current explanation a compact notation of this expression suffices:

$$\Phi_{Si-TiO_x} = A + B(\Phi_{Al} - \Phi_{Si}) + \Phi_{Si-TiO_x dipole} [28], \tag{5.9}$$

where A is a variable depending on the work function and electron affinity of the Si, B a variable depending on the capacitance of the TiO_x and c-Si (which in turn depends on the induced bending in the c-Si; i.e. equation 5.9 is an implicit function), Φ_{Si} is the work function of the Si, Φ_{Al} the work function of the aluminum, and $\Phi_{Si-TiO_x dipole}$ a contribution to the barrier height originating from a dipole at the Si - TiO_x interface.

From Equation 5.9 it becomes clear that a low work function metal ($\Phi_{Al} < \Phi_{Si}$) can reduce the barrier Φ_{Si-TiO_x}. The influence of the work function on the contact resistivity of a Si - TiO_x - metal stack is experimentally confirmed by several studies [40], [19], [20], [35]. The impact of the work function on the contact resistivity is mediated by the variable B. An increase of the TiO_x thickness decreases the capacitance of the TiO_x and therefore the value of B. For a low work function metal like Al (≈ 4 eV [16]), a decrease of B means an increase of the barrier height. TiO_x thickness influences also the Si - TiO_x interface as shown in Figure 5.22 of Section 5.4. This can have an effect on the magnitude of the dipole at this interface ($\Phi_{Si-TiO_x dipole}$). The rectifying behavior for thicker TiO_x films as presented in Figure 5.33 can be explained by the above two mentioned mechanisms.

The ALD growth temperature of the TiO_x can influence the interface properties ($\Phi_{Si-TiO_x dipole}$) and material properties like the capacitance of TiO_x, which could alter B, leading to a higher potential barrier.

Next to the TiO_x thickness and ALD temperature, post-deposition annealing proved to substantially change the contact resistivity (see Figures 5.31 and 5.33). From the J-V curves of Figures 5.32a, 5.32b, 5.34a, and 5.34b it becomes clear that annealing changes the rectifying contact behavior to Ohmic behavior; i.e. the barrier at the Si - TiO_x interface (Φ_{Si-TiO_x}) decrease significantly upon annealing. The reason for this change is assumed to be the changing Si - SiO_x - TiO_x and TiO_x - Al interfaces. For the Si - SiO_x - TiO_x interface, Figure 5.35B from Section 5.4 shows

substantial growth of the SiO_x layer upon annealing. For the second interface (TiO_x - Al), Yang et al. [18] reported the formation of a AlO_x layer and a reduction of the TiO_x layer, see Figure 5.35C. These changing interfaces could impact the interface dipoles and thereby reduce the potential barrier at the Si - TiO_x interface [19], [28].

For the depletion region in the Si, it is finally interesting to note that the width of this depletion region (W) and thus R_{Si} can be reduced by increasing the carrier concentration of the Si near its interface with TiO_x; i.e. n-type doping of the Si surface could prove to be beneficial for ρ_c.

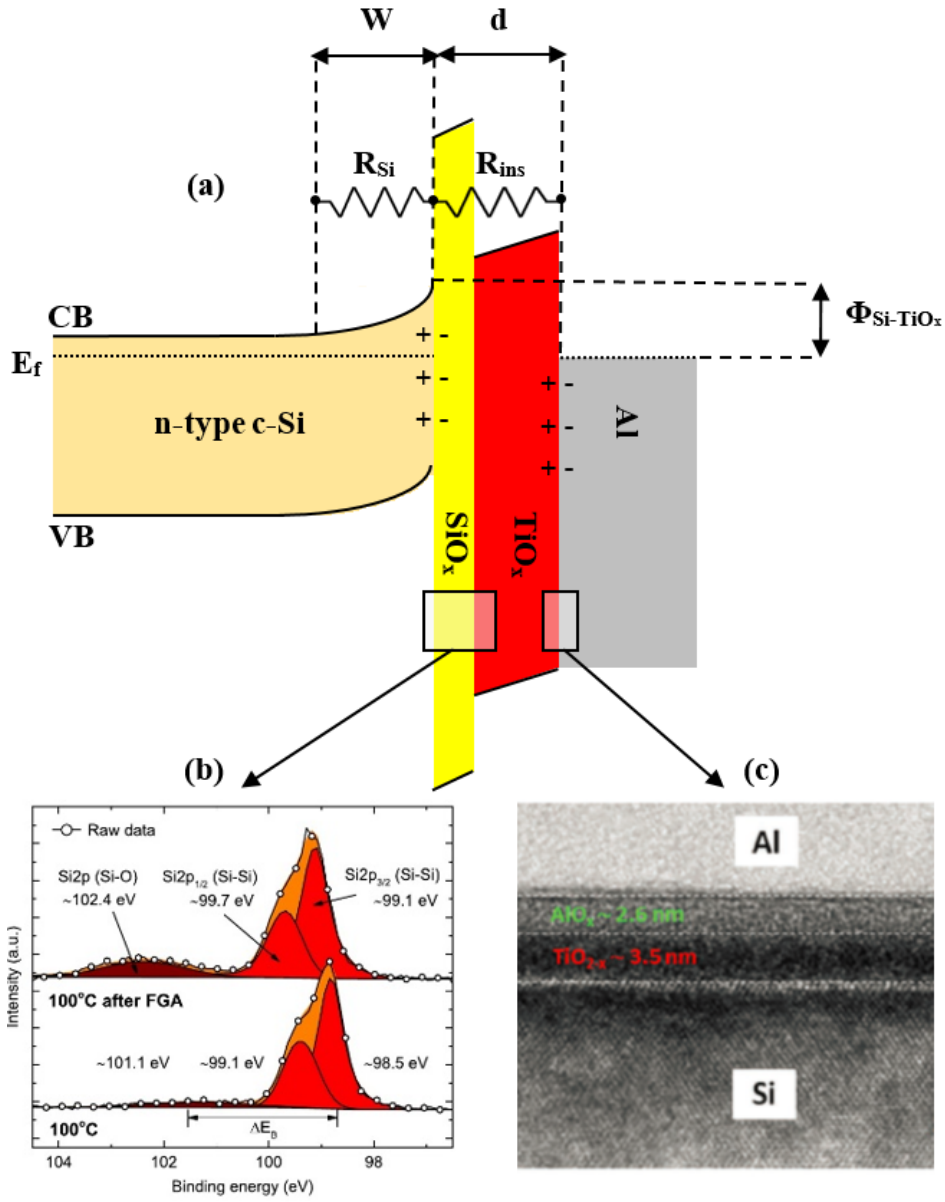

Figure 5.35: (a): An example of a possible band diagram for the Si - TiO_x - Al contacts used in this work. Note that R_{Si} and R_{ins} are not simple Ohmic resistances, they only indicate resistance. (b): XPS spectrum that shows an increase of the SiO_x interlayer upon annealing. Figure b originates from Section 5.4 (c): TEM image from the TiO_x - metal interface after annealing: a clear AlO_x interlayer has formed. Figure c originates from the work of Yang et al. [18].

With regard to the contribution of resistance of R_{Ins} to the contact resistance, it has already been mentioned that, in the as-deposited state, this contribution is less important to the contact resistivity than the effect of the depletion region in the Si (R_{Si}). After annealing, however, the contact behavior of all Si-TiO_x-Al stacks becomes Ohmic, and R_{Ins} becomes the limiting factor. Like the depletion region in the Si, the resistance of the SiO_x and TiO_x interlayers is mainly determined by the width (d in Figure 5.35) and the distance between the conduction band and Fermi-level (in Figure 5.35A). A qualitative conclusion about R_{Ins} can be drawn from the forward bias current: the steeper the slope of the J-V curve, the lower the series resistance due to SiO_x and TiO_x (R_{Ins}). Two factors that influence R_{Ins} are found to be the TiO_x thickness and post-deposition annealing. Yang et al. [18] and Allen et al. [19] link the latter to the formation of oxygen vacancies in the TiO_x created by the oxygen reducing reaction between the metal and the TiO_x upon annealing.

5.7 Conclusions and recommendations

The goal of this work was to identify the important factors and mechanisms for the passivation and contact resistivity of ALD TiO_x. This chapter presents the most important results together with suggestions for future work.

A good level of c-Si surface passivation can be obtained by depositing a 3 to 5 nm thick ALD TiO_x film on the c-Si. Recombination velocities as low as $S_{eff,max} = 10.7$ cm/s have been obtained, which are comparable with the best results from other passivation studies of TiO_x ($S_{eff,max} = 2.8$ - 15 cm/s [17], [18], [19], [33], [21]). The c-Si surface passivation by TiO_x is found to be a combination of chemical passivation and field-effect passivation. The latter is established through an induced upward band bending of 0.86 eV in c-Si(n). A post-deposition forming gas anneal proved key to activate the chemical passivation and achieve the high level of passivation. The Si surface treatment prior to ALD proves to be another important factor for the passivation. TiO_x on RCA-cleaned c-Si provides significantly better passivation ($S_{eff,max} = 10.9$ cm/s) than on NAOS-treated c-Si ($S_{eff,max} = 31.1$ cm/s), while the passivation level of TiO_x on HF-cleaned Si depends strongly on the ALD temperature ($S_{eff,max} = 10.7$ - 82 cm/s for $T_{dep} = 50$ - 300 °C). While the RCA and NAOS treatment cover the Si surface with a SiO_x layer of about 1.5 nm, the HF cleaning results in H-terminated c-Si and a substoichiometric SiO_x interlayer forms during the ALD process. The latter could explain the stronger dependence on the ALD process.

Next to good c-Si surface passivation, a c-Si/TiO_x/Al contact configuration has shown to result in low Ohmic contact behavior, with contact resistivity values well below $\rho_c \leq 10^{-1}$ Ω·cm^2. The contact resistivity increases with both TiO_x thickness and ALD temperature. A post-deposition forming gas anneal turned out to be key in decreasing the contact resistivity to values as low as $\rho_c \leq 10^{-2}$ Ω·cm^2 for TiO_x thicknesses and ALD temperatures of $d \leq 4$ nm and $T_{dep} \leq 200$ °C, respectively. The beneficial effect of the FGA is supposed to be a result of both a decrease of the series resistance of the TiO_x interlayer and a reduction of the induced upward band bending in the c-Si. The latter is found to be the primary reason for the high ρ_c before annealing and is thought to originate from c-Si/TiO_x and TiO_x/Al interface induced dipoles. Next to post-deposition annealing, theory and literature showed that a low work function contact material is essential for a low Ohmic c-Si/TiO_x/contact material stack.

For a low Ohmic electron-selective contact, a downward band bending in the c-Si is required. This work showed that the c-Si surface passivation by TiO_x has an important field-effect component that is not established by downward, but upward band bending in the c-Si. Fabrication of an electron contact with good c-Si surface passivation and low ρ_c is therefore not necessarily evident. For future work it is important to investigate the origin of the c-Si band bending by TiO_x and try to establish substantial downward band bending in the c-Si by either tailoring the TiO_x properties (e.g. stoichiometry, doping) and interfaces (e.g. SiO_x interlayer) or by using a (very) low work function material in combination with TiO_x. Since TiO_x has the highest potential when applied in a transparent front contact, it is furthermore recommended to focus on transparent configurations like c-Si/TiO_x/TCO/metal-grid stacks. For the TiO_x layer, a 3 to 5 nm thick layer deposited on HF-cleaned c-Si at a low ALD temperature (50 °C) in combination with a post-deposition FGA seems most promising. To establish a low Ohmic contact with substantial field-effect passivation, a low work function TCO ($\Phi_{TCO} \leq 4$ eV) is a requisite.

Chapter 6

Niobium-doped titanium oxide

6.1 Introduction

Until now, only undoped TiO_x has been used as electron-selective passivating contact for c-Si solar cells. In the field of semiconductors and solar cells, it is however well known that controlled doping of a material enables a certain degree of control over the material's work function and thereby control and improvement over several of its electrical properties [6]. For a passivating contact, the latter could possibly lead to enhanced field-effect passivation, electron selectivity and lower contact resistivity. Controlled extrinsic n-type doping of TiO_x could lead to downward band bending in the c-Si and thereby to an improved and tunable electron-selective contact with TiO_x; i.e. n-type doping of TiO_x is a completely new and promising option to investigate.

For the purpose of extrinsic doping, an ALD recipe is developed that enables the deposition of n-type doped titanium oxide. The chosen dopant for the extrinsic doping is niobium (Nb) and for the ALD doping a similar approach is used as in earlier ALD doping studies e.g. ALD ZnO:Al [72]. Although extrinsically Nb-doped ALD TiO_x has never been explored in the context of passivating contacts, for other applications, like TCOs, TiO_x:Nb has been investigated. For TCOs and for other applications that require high electrical conductivity, the crystalline anatase phase of TiO_x(:Nb) is used [73], [74]. The lattice structure of the anatase phase supports namely electrical conductivity (also the rutile crystal phase support electrical conductivity, but to a lesser extent) [73]. Several different techniques have been used to deposit TiO_x:Nb films including pulsed laser deposition [75], sputter deposition [76], and ALD [73], [74]. A post-deposition annealing treatment is often used to improve the material properties, but especially to crystallize the as-deposited films to anatase TiO_x:Nb. The resistivity (ρ) of these annealed films is reported to decrease with increasing Nb content, reaching values as low as $\rho = 10^{-4}$ - 10^{-3} Ω·cm [75],[76], [73], [74]. Niobium has thus been demonstrated to be a suitable dopant for TiO_x.

This chapter will start with a description of the experimental details, including the newly developed ALD process of niobium-doped titanium oxide. A second section will discuss the niobium-doped TiO_x bulk material properties. A third part presents the first experimental results of the passivating properties and the contact resistivity. The chapter will end with a conclusion and recommendations for further research.

6.2 Experimental details

The used measurement techniques and the fabrication and characterization of lifetime and contact resistivity samples is completely similar to those of the TiO_x material study presented in Chapter 5. Details can therefore be found in Section 5.2. This section will only discuss the newly developed ALD process of TiO_x:Nb.

6.2.1 Atomic layer deposition of niobium-doped titanium oxide

The Nb-doped TiO_x films are deposited by atomic layer deposition in a similar fashion as existing ALD doping recipes from for example the work of Wu et al. [72] on ALD ZnO:Al and Niemelä et al. [73] also on ALD TiO_x:Nb. The TiO_x:Nb ALD recipe uses n ALD cycles TiO_x followed by 1 ALD cycle NbO_x. By varying the value of n, the dopant concentration can be changed. The combination of n ALD cycles TiO_x followed by 1 ALD cycle NbO_x is defined as 1 ALD supercycle. A supercycle is repeated several times until the desired film thickness is reached. A simplified and schematic representation of such a supercycle recipe is shown in Figure 6.1. The ALD recipe for the TiO_x is a thermal recipe using TDMAT as Ti-precursor and H_2O as oxidant. The TiO_x ALD recipe is the same recipe used for the TiO_x material study, as described in Section 5.2.2 of Chapter 5. Like TiO_x, the niobium oxide recipe is also a thermal ALD recipe, which was developed by S.B. Basuvalingam from Eindhoven University of Technology [77]. The niobium oxide ALD process uses (tert-butylimido)-tris (diethylamino)- niobium (TBTDEN) as niobium precursor (see Figure 6.3) and H_2O as oxidant. A detailed description of this process can be found in Figure 6.2. The substrate holder is kept at a temperature of 200°C during the whole recipe. The reactor walls are kept at their maximum value of 150 °C. At the start of the recipe, there is a 15 minutes pre-heat step at 200 mTorr.

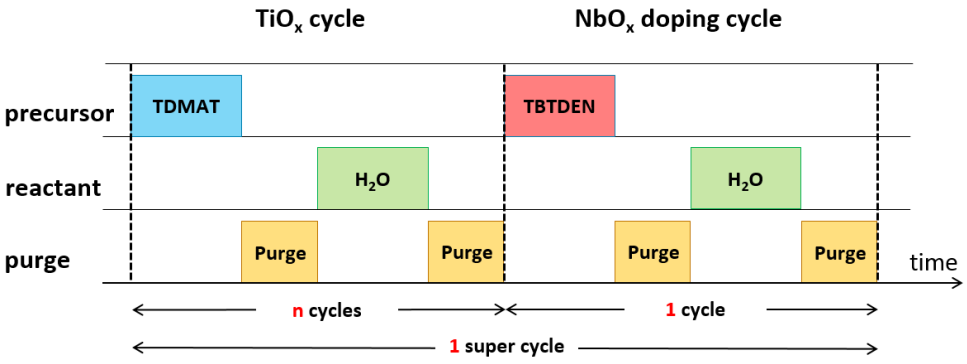

Figure 6.1: Simplified schematic representation of the ALD super cycle recipe for Nb-doped TiO_x.

Depth-profiling XPS is used to determine the atomic percentages of Nb and Ti in the TiO_x:Nb films. Throughout this work, the measured fraction of Nb atoms in the TiO_x:Nb film (NbF_{XPS}) will be used as a measure for the doping concentration:

$$NbF_{XPS} = \frac{Nb_{at.}\%}{Nb_{at.}\% + Ti_{at.}\%},$$

where $Nb_{at.}\%$ is the atomic percentage of Nb atoms, and Ti is the atomic percentage of Ti atoms.

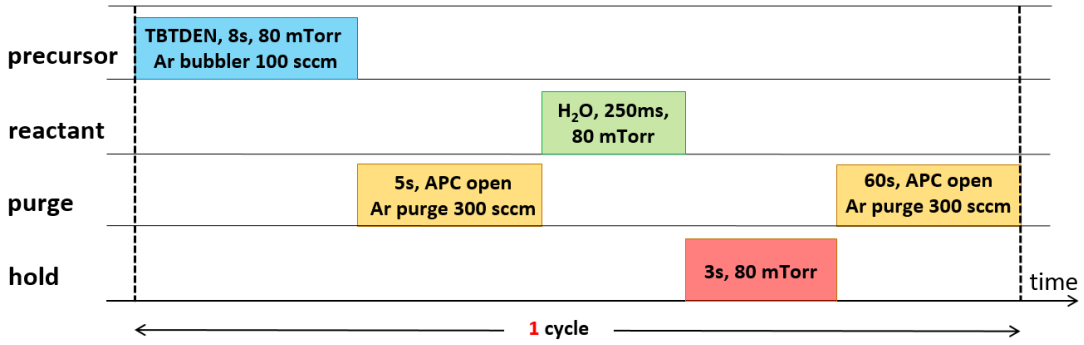

Figure 6.2: Atomic layer deposition recipe of niobium oxide. The recipe was developed by S.B. Basuvalingam from Eindhoven University of Technology [77].

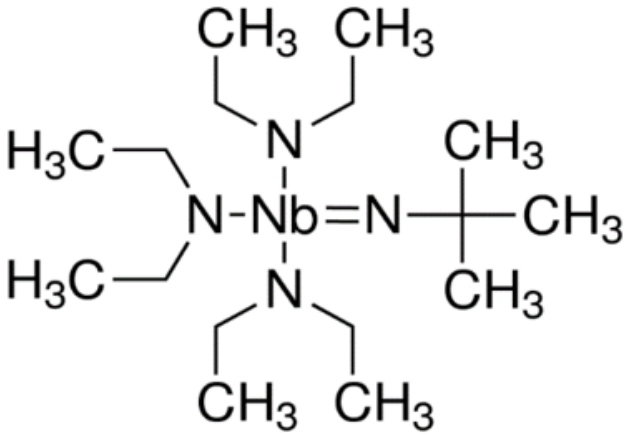

Figure 6.3: The (tert-butylimido)-tris (diethylamino)- niobium (TBTDEN) Nb-precursor.

6.3 Material properties

6.3.1 ALD growth

The growth of the TiO_x:Nb layers was monitored using in-situ spectroscopic ellipsometry. From Figure 6.4, it turns out that the ALD process of this supercycle recipe is linear for $NbF_{\mathrm{XPS}} \leq 0.13$ with approximately the same GPC (0.40±0.01) as for the TiO_x recipe (0.43±0.01) (see Figure 6.2). This indicates that the addition of a niobium oxide cycle has only a very small effect on the growth of TiO_x. The niobium content of the film is determined by X-ray photoelectron spectroscopy. Figure 6.5 represents the atomic Nb fraction (Nb/(Nb+Ti)) as determined by XPS (NbF_{XPS}) versus the fraction of NbO_x ALD cycles (NbO_x/(NbO_x+TiO_x)) in the ALD recipe (NbF_{ALD}). The figures shows that the measured atomic ratio is linear with the ALD cycle ratio (slope 1.4±0.04 (a.u.)), which means that the ALD doping recipe allows for good control over the doping concentration.

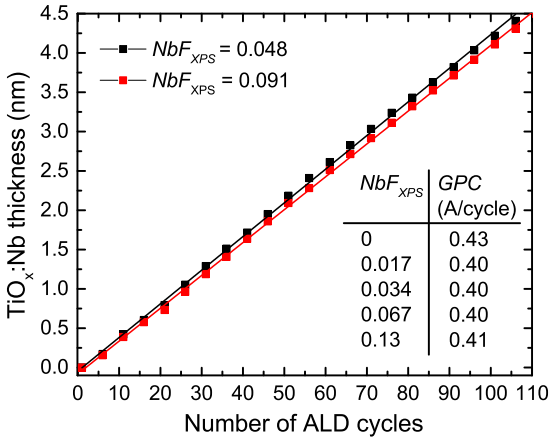

Figure 6.4: Measured film thickness of TiO_x:Nb as function of number of ALD cycles.

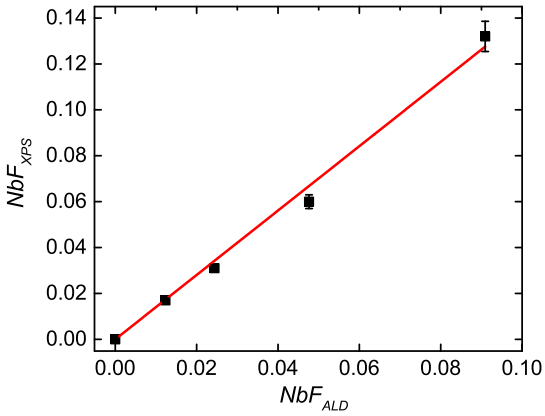

Figure 6.5: The Nb/(Nb+Ti) atomic ratio as determined by XPS (NbF_{XPS}) versus the NbO_x/(NbO_x+TiO_x) ALD cycle ratio (NbF_{ALD}). The slope of the fit equals 1.4±0.04 (a.u.).

6.3.2 Crystallinity

Raman spectroscopy revealed that the 30 nm as-deposited TiO_x:Nb films are amorphous for all the investigated doping concentrations. A post-deposition forming gas anneal at 300 °C leads to the crystallization of the films. This crystallization is shown for a 30 nm film with $NbF_{\mathrm{XPS}} = 0.034$ in Figure 6.6. The Raman spectra for increasing anneal time show a growing peak at 148 cm^{-1}, which indicates a growing fraction of anatase crystalline TiO_x in the film[55].

A first exception to this transformation from amorphous to anatase TiO_x are thinner TiO_x:Nb films ($\leq$ 5 nm). Raman spectroscopy of a thinner TiO_x:Nb films (5 nm) with $NbF_{XPS} = 0$ and 0.034 showed no peak at 148 cm^{-1} upon annealing at 300 °C (for 5 nm $NbF_{XPS} = 0.034$ see Figure 6.6 and for 5 nm $NbF_{XPS} = 0.0$ see Figures 5.11 and 5.12 in Section 5.3.2). These thin film remained thus amorphous, also after annealing as long as 1 hour. This is an important observation that implies that the findings of the 30 nm thick doped films may not apply to thinner doped films ($\leq$ 5 nm). A possible reason for the difference in crystallization behavior can be found in the work of Kužel et al. [78]. They report a strong decrease in both crystallization speed and onset time with decreasing TiO_x film thickness; i.e. thinner TiO_x films are harder to crystallize. They attribute this observation to a rapid increase in tensile stresses with decreasing film thickness. A second exception to the crystallization is the 30 nm film with highest doping concentration ($NbF_{XPS} = 0.13$). Even after 1 hour of annealing no peak around 148 cm^{-1} was visible. It could be that the number of NbO_x layers in this TiO_x:Nb film has reach a level at which it starts to hinder the crystallization of the film.

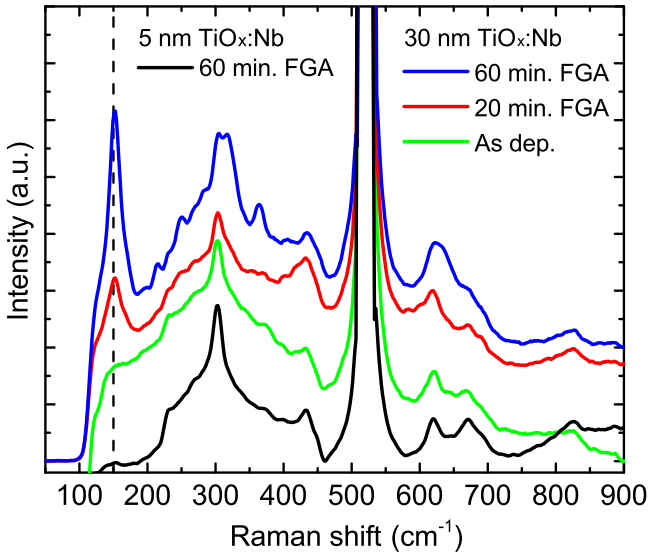

Figure 6.6: Raman spectra of a 5 nm and 30 nm TiO_x:Nb film with $NbF_{XPS} = 0.034$ deposited at 200 °C. In the as-deposited state (green) there is no peak related to any of the crystal phases of TiO_x. After 20 minutes of forming gas annealing, a clear peak starts to appear at 148 cm^{-1} for the 30 nm film, indicating anatase TiO_x (see dashed line). The 5 nm film with $NbF_{XPS} = 0.034$ remains amorphous upon annealing.

Transmission electron microscope (TEM) imaging before and after 1 hour forming gas annealing support the Raman spectroscopy findings for the 30 nm TiO_x:Nb films with $NbF_{XPS} \leq 0.13$ (see Figures 6.7a - 6.7d). The TEM image before annealing show an amorphous film, while after annealing crystalline structures are visible. It appears however that there are numerous different crystal orientations and/or defects in the lattice. A higher anneal temperature of 500 °C as used by Niemelä et al. [73], may result in a larger crystal size and a more ordered crystal structure.

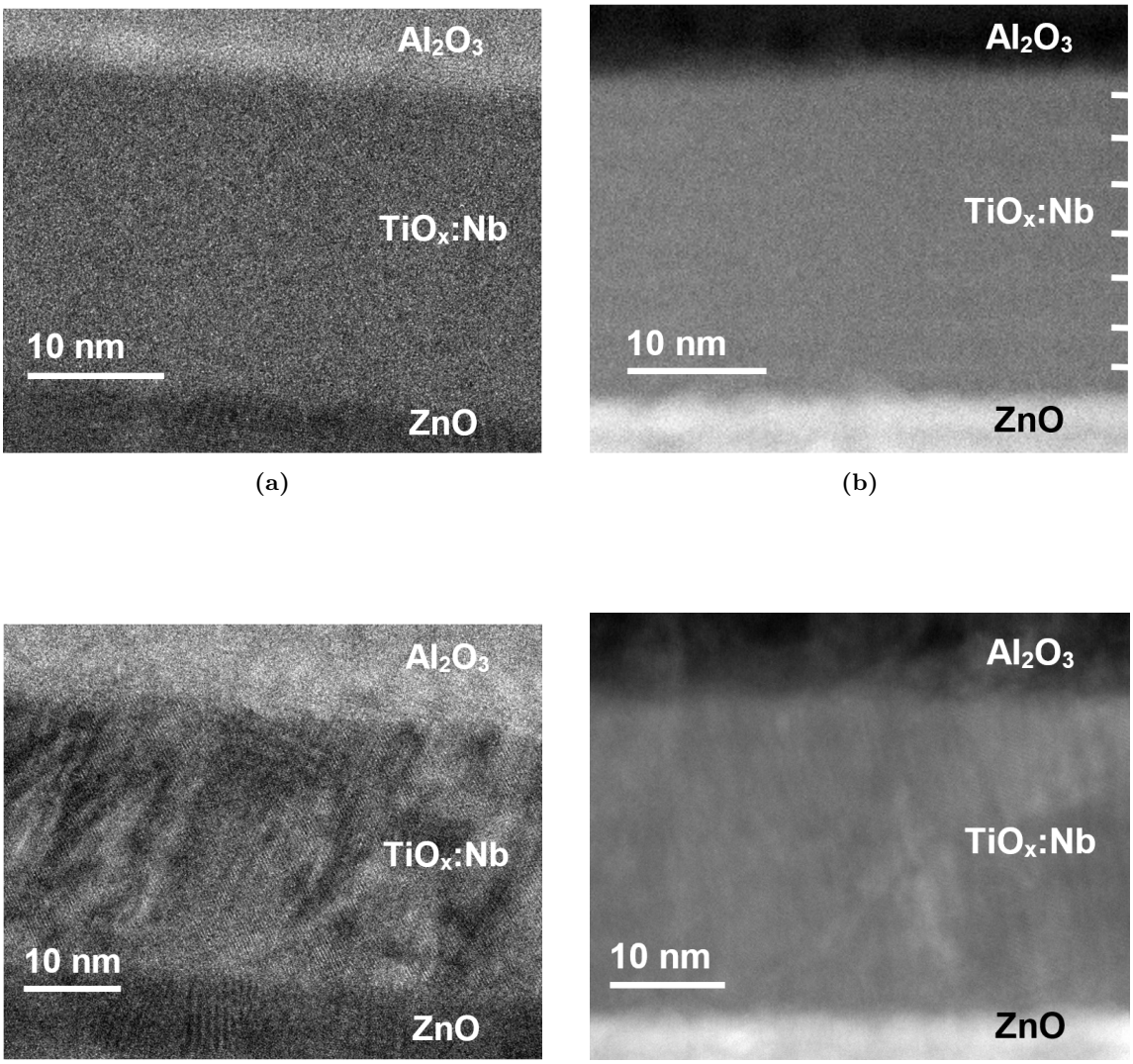

Figure 6.7: Transmission electron microscopy (TEM) cross sections of a 30 nm thick TiO_x:Nb film deposited at 200 °C with doping concentration $NbF_{\mathrm{XPS}} = 0.014$. The film is deposited on ZnO and capped with Al_2O_3 for protection. (a): Bright field TEM of the TiO_x:Nb film in the as-deposited state. No crystal features are present, indicating the amorphous character of the film. (b): High Angle Annular Dark Field (HAADF) TEM of the Nb-doped TiO_x film in the as-deposited state. The small white bars on the right indicate the NbO_x interlayers, which are very weakly visible as horizontal lines. In the Nb profile extracted from EDX the interlayers are more evident (see Appendix D). (c): Bright field TEM of the TiO_x:Nb film after 1 hour FGA at 300 °C. Clear features are present, indicating the crystalline character of the film after annealing. Note that the crystal structure is somewhat disordered. (d): High Angle Annular Dark Field (HAADF) TEM of the Nb-doped TiO_x film after 1 hour of forming gas anneal at 300 °C. Also here, there are clear crystalline features, with a somewhat disordered crystal structure. The NbO_x interlayers are no longer visible. The Nb profile extracted from EDX shows however that they still exist (see Appendix D).

6.3.3 Stoichiometry

The XPS spectra of the titanium Ti2p peak, the niobium Nb3d peak, and the oxygen O1s peak are shown in Figures 6.8, 6.9 and 6.10 respectively. All films are determined to be nearly stoichiometric with an oxygen to titanium and niobium ratio of $\frac{O}{Nb+Ti} = 1.9 \pm 0.1$ (see Table 6.1). The nearly stoichiometric character of the films is confirmed by the fact that the Ti2p peak (Figure 6.8) could be well modeled with TiO_2.

Note that the niobium that is incorporated in the film is present as fully oxidized niobium oxide (Nb_2O_5). The oxygen peak shows no clear shoulders, meaning that the oxygen in the film is all bonded to titanium or niobium. The film with the highest doping concentration has a slightly higher oxygen to titanium and niobium ratio of 2.0 ± 0.1. The oxygen to niobium ratio for stoichiometric Nb_2O_5 is 2.5, which is higher than the oxygen-to-titanium ratio for stoichiometric TiO_2. A relatively high Nb-fraction ($NbF_{\mathrm{XPS}} = 0.013$) can therefore raise the effective stoichiometry of the film (NbF_{XPS}).

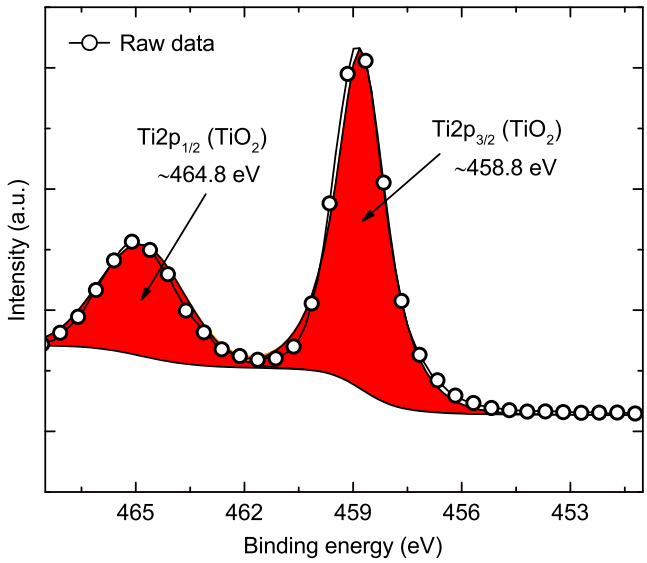

Figure 6.8: XPS spectrum of the titanium Ti2p peak for a 30 nm TiO_x:Nb film deposited at 200 °C with $NbF_{\mathrm{XPS}} = 0.034$ in the as-deposited state.

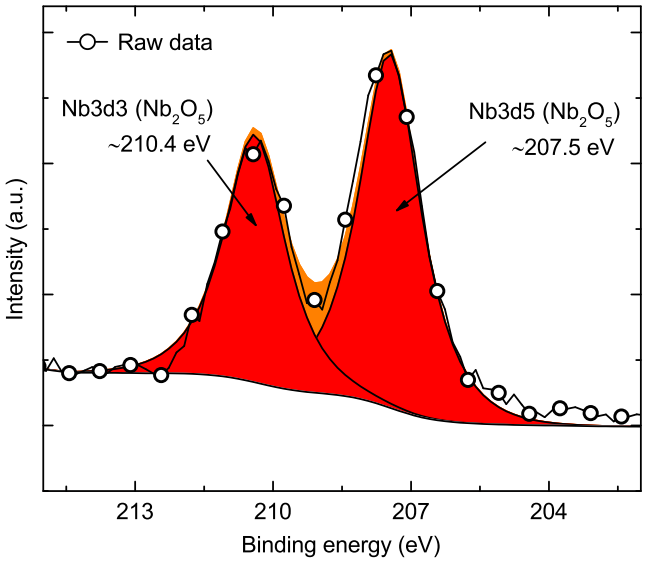

Figure 6.9: XPS spectrum of the niobium Nb3d peak for a 30 nm TiO_x:Nb film deposited at 200 °C with $NbF_{\mathrm{XPS}} = 0.034$ in the as-deposited state.

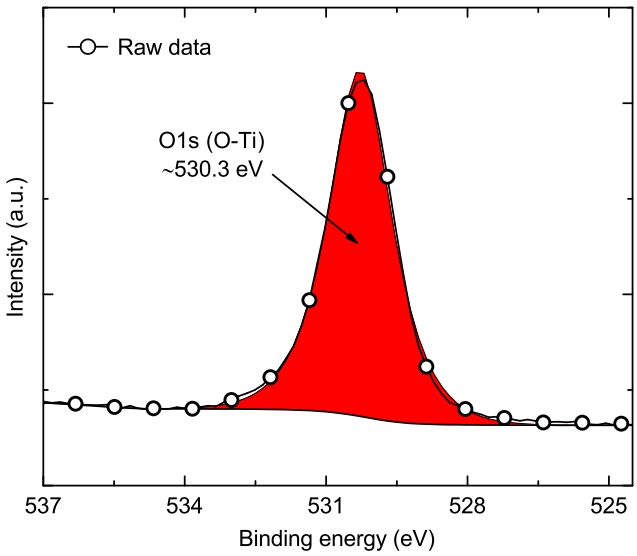

Figure 6.10: XPS spectrum of the oxygen O1s peak for a 30 nm TiO_x:Nb film deposited at 200 °C with $NbF_{\mathrm{XPS}} = 0.034$ in the as-deposited state.

Table 6.1: Oxygen to titanium and niobium ratio ($\frac{O}{Nb+Ti}$) for 30 nm thick films deposited at 200 °C in the as-deposited state as function of doping concentration. The stoichiometry is determined at the surface of the film to avoid effects of preferential oxygen sputtering on the stochiometry determination (see Section 5.2.6).

NbF_{XPS}	O/(Ti+Nb)
0	1.9±0.1
0.017	1.9±0.1
0.034	1.9±0.1
0.067	1.9±0.1
0.13	2.0±0.1

6.3.4 Chemical impurities

X-ray photoelectron spectroscopy showed that the deposited TiO_x:Nb films contain besides titanium, niobium and oxygen, very low levels of carbon and nitrogen. The carbon and nitrogen levels are below 2at.% and 1at.%, respectively (see Figures C.3 and C.4 in Appendix C). This demonstrates that the films have a high purity.

6.3.5 Electrical conductivity

Four-point probe measurements revealed that the electrical resistivity of all 30 nm thick TiO_x:Nb films is around $\rho \approx 3$ Ω·cm in the as-deposited state (see Figure 6.11). After a forming gas anneal the resistivity drops with three orders of magnitude to values as low as $\rho = 9\pm2 \cdot 10^{-3}$Ω·cm (see Figure 6.11), which is similar to the values found by Pore et al. [74] and Niemelä et al. [73]. The film with the highest doping concentration ($NbF_{\mathrm{XPS}} = 0.13$) did show an increase in resistivity instead of a decrease. This behavior correlates with the fact that this film did not crystallize upon annealing (see 6.3.2). Using a post-deposition anneal to crystallize the TiO_x:Nb to anatase phase is therefore crucial to obtain a low resistivity; something that well known in literature Pore et al. [74] and Niemelä et al. [73]. Not only the doped TiO_x films show good conductivity, but also the undoped film. The oxygen-to-titanium ratio as determined by XPS is approximately 1.9±0.1. This ratio suggests that the films are slightly substoichiometric (see 6.3.3) and substoichiometric TiO_x is known to be conductive [40], [41], [79].

Alternating current Hall measurements (after annealing) revealed that the decrease in resistivity with doping concentration is related to a higher free electron concentration (see Figure 6.18a). The electron mobility of the films appears to be rather independent of the doping concentration and has a relatively low value of $\mu_e = 0.7$ cm^2/Vs (see Figure 6.18b) compared to earlier reported values of μ_e = 4.2-22 cm^2/Vs for ALD TiO_x:Nb in the work of Niemelä et al. [73]. The lower mobility may be explained by higher degree of grain boundary scattering due to smaller crystal grains [74], [80], resulting from a lower post-deposition anneal temperature [81] (300 °C in this work and 500 °C in the work of Niemelä et al. [73]).

While the resistivity of the 30 nm TiO_x:Nb films could be easily measured with a four-point probe, thinner TiO_x:Nb films ($\leq$ 5 nm) could not be measured with a four-point probe, indicating a very high resistivity. The observation that the thin films did not crystallize upon annealing (see Section 6.3.2) is assumed to be the main reason for the high resistivity of the thinner films. Another effect that could contribute to the high resistivity of the thin TiO_x(:Nb) films, could be a carrier depletion of the thin films by absorbed species like oxygen or water. The latter phenomenon is for example used in resistance based gas sensors with TiO_x [57],[58],[59]. A schematic representation of the carrier depletion by adsorbed molecules is presented in Figure 6.13. Films with a thickness $d \leq d_{dep}$ can become largely depleted by adsorbed molecules, leading to a high resistivity. Films with $d \geq d_{dep}$ are only partially depleted and can therefore exhibit a low resistivity. For future work, it would be interesting to investigate to which extent this effect is important.

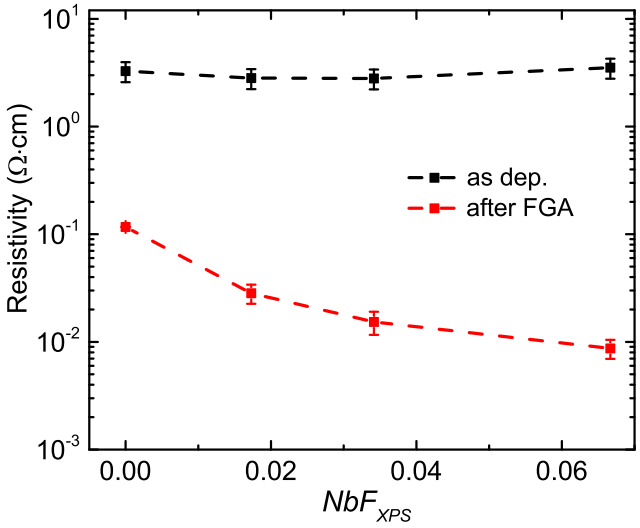

Figure 6.11: Electrical resistivity of 30 nm thick TiO_x:Nb films deposited at 200 °C as a function of doping concentration. A large drop in resistivity is observed after 1 hour forming gas annealing at 300 °C (red) compared to the as-deposited state (black). The presented resistivity values are obtained with a four-point probe measurement, the resistivity measured with the Hall setup gave similar results. Uncertainty in the presented values is determined from the standard deviation of several measurements and samples.

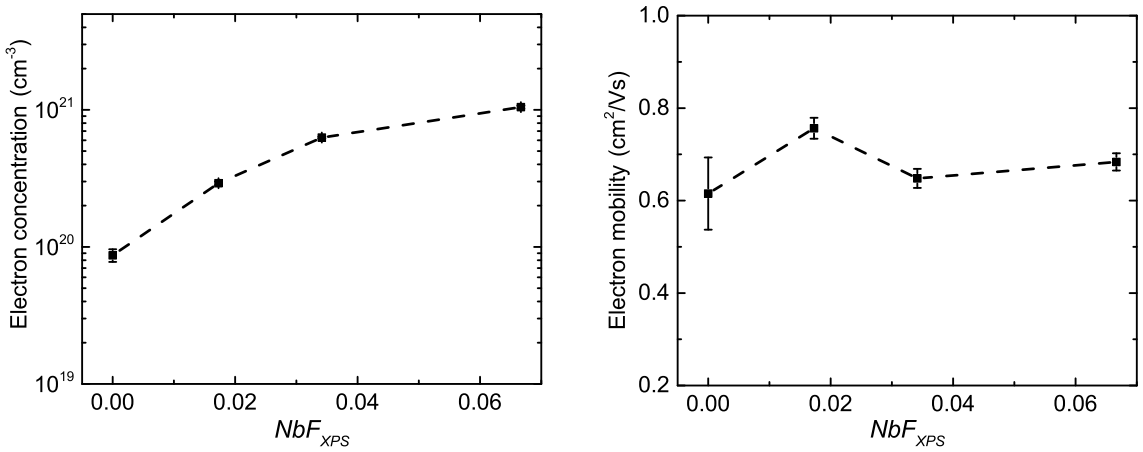

Figure 6.12: The electron concentration (a) and electron mobility (b) of 30 nm thick TiO_x:Nb films deposited at 200 °C as a function of the doping concentration. The electron concentration and mobility are obtained with AC Hall measurements after 1 hour forming gas annealing at 300 °C. Uncertainty in the presented values is estimated from the standard deviation in the values obtained from an AC and a DC Hall measurement.

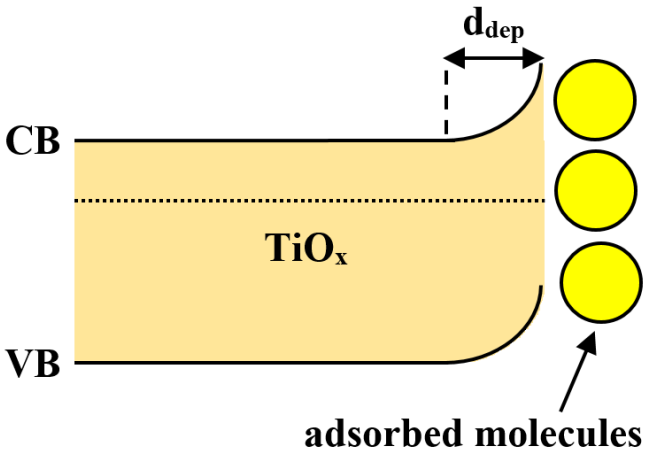

Figure 6.13: A schematic representation of the carrier depletion in TiO_x(:Nb) by adsorbed molecules (depicted in yellow). The carrier depletion region is indicated in the band diagram of TiO_x(:Nb) with d_{dep}.

6.4 Passivation

The effective lifetime for both 3 and 5 nm thick TiO_x:Nb films on HF-cleaned silicon as a function of doping concentration is presented in Figure 6.14. The Figure shows that the c-Si surface passivation shows almost no change as a function of doping concentration. To further investigate the effect of doping, the surface passivation is also investigated for a fixed doping concentration of $NbF_{\mathrm{XPS}} = 0.13$ as a function TiO_x:Nb film thickness. Figure 6.15 shows this data togther with the surface passivation provided by 1-5 nm undoped TiO_x. Like in figure 6.14, the surface passivation is virtually the same for doped and undoped TiO_x.

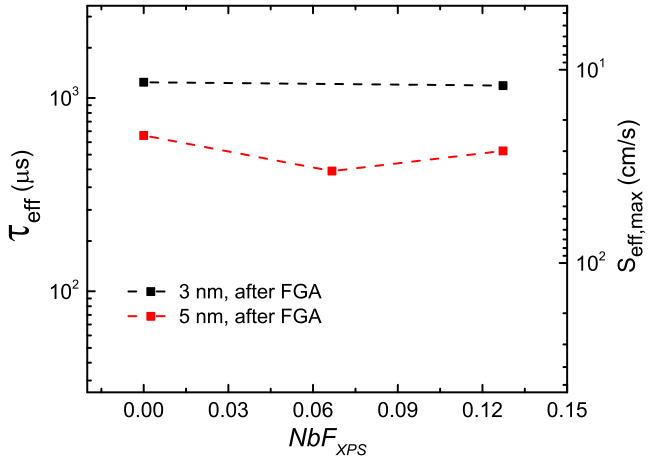

Figure 6.14: The effective minority carrier lifetime (left axis) and surface recombination velocity (right axis) as a function of Nb doping concentration. The lifetime for both 3 and 5 nm films deposited at 200 °C on HF-cleaned Si are presented after forming gas annealing (see Appendix A for the used anneal times).

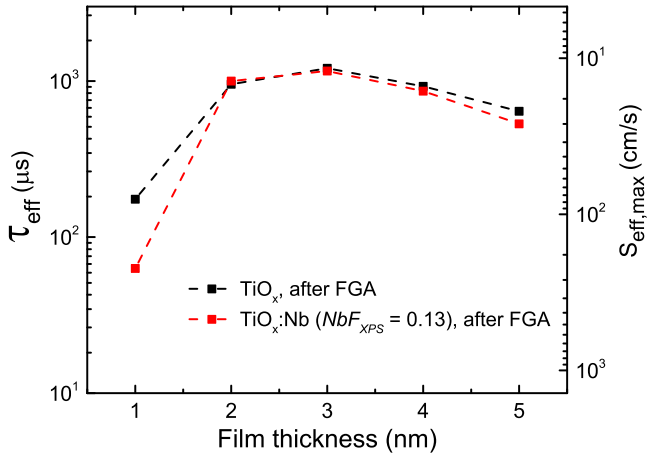

Figure 6.15: The effective minority carrier lifetime (left axis) and surface recombination velocity (right axis) as a function of thickness for undoped TiO_x and doped TiO_x ($NbF_{\mathrm{XPS}} = 0.13$). The films are deposited at 200 °C on HF-cleaned Si and received a forming gas annealing (see Appendix A for the anneal times).

For c-Si surface passivation, both the chemical passivation and field-effect passivation are important. The chemical passivation depends on the defect density of the Si/TiO_x(:Nb) interface and the hydrogenation of this interface (see Section 2.3). Since the first cycles of the ALD doping recipe consists always of $n/2$ TiO_x cycles, the first few atomic layers of deposited material on the c-Si is always TiO_x (see Section 6.2.1). The Si/TiO_x:Nb interface is therefore hardly different from a Si/TiO_x interface, and it is therefore not expected to change with doping concentration. The small amount of Nb in the TiO_x:Nb film is also not expected to change properties that are important for the hydrogenation (e.g. hydrogen content). In short, the chemical passivation of TiO_x:Nb is not expected to change with doping concentration. A factor that is considered important for the chemical passivation is whether the TiO_x:Nb film is crystalline or amorphous [17].

For field-effect passivation fixed charge and/or a difference in the Fermi-level of the c-Si and the TiO_x:Nb is important. When a layer of c-Si and TiO_x:Nb are contacted, the Fermi-levels of both materials will align to reach electro-chemical equilibrium. The latter is accomplished by charge exchange, which leads to band bending in the c-Si (and TiO_x:Nb), hence field-effect passivation. A good example of field-effect passivation that is established in this way is by crystalline ZnO:Al on c-Si(n)[34]. The degree of c-Si band depends on the difference in the Fermi-levels of c-Si and TiO_x:Nb (Δ_{E_f}). Nb-doping increases the electron concentration (see Figure 6.18a), which indicates a shift of the Fermi-level upwards [6]; i.e. towards the conduction band of TiO_x:Nb. This shift results in a different Δ_{E_f}, which leads to more downward c-Si band bending. Wether this downward band bending results in a net downward band bending in the c-Si depends on the absolute positions of the Fermi-levels of c-Si and TiO_x:Nb, and on the presence and extent of fixed charge at for example the c-Si/TiO_x:Nb interface. It can however be stated that Nb doping is expected to change the induced field-effect passivation of TiO_x:Nb by contributing downward band bending in the c-Si.

Considering the expectations described above, the unchanged surface passivation presented in Figures 6.14 and 6.15 seems contradictory at first glance. Considering the material properties of the thin films ($\leq$ 5 nm), the results seem however less contradictory. The thin films TiO_x:Nb ($\leq$ 5 nm) have an amorphous character (Figure 6.6) and the resistivity turned out to high to be measured (Section 6.3.5). These material properties are in sharp contrast to the 30 nm TiO_x:Nb films, which are crystalline (Figure 6.6) and exhibit a very low resistivity (Figure 6.11). It seem clear that Nb doping is not or significantly less active in thin amorphous TiO_x:Nb films used in this passivation study. To exploit the Nb-doping in these thin films ($\leq$ 5 nm), crystallization of the thin films is essential. A possible route to achieve this is the use of higher temperatures during the post-deposition annealing. Alternatively, thicker TiO_x:Nb films can be used. Both option are interesting for future work.

6.5 Contact resistivity

The effect of Nb doping as a function of the doping concentration for 3 and 5 nm thick TiO_x:Nb films is presented in Figures 6.16 and 6.17 respectively. Both Figures 6.18a and 6.18b show a clear increase of the contact resistivity with the doping concentration. Some insight in the reason behind the higher ρ_c for the doped films is given by the J-V curves in Figures 6.18a and 6.18b. The J-V curves show a strongly reduced reverse bias current (Voltage < 0 V) for the doped TiO_x, which indicates a depletion region in the c-Si (see Section 5.6.3).

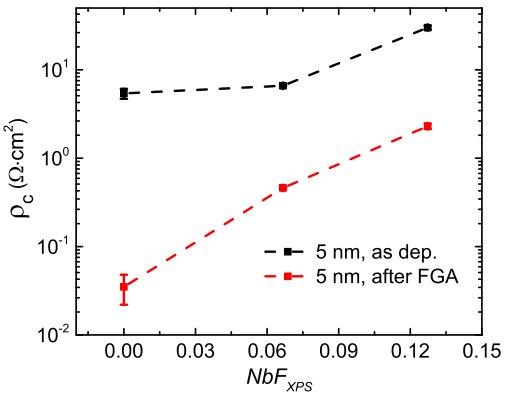

Figure 6.16: Contact resistivity of 5 nm thick films as function of doping concentration before and after forming gas anneal at 300 °C. (see Appendix B for the used anneal times) The films are deposited at a temperature of 200 °C.

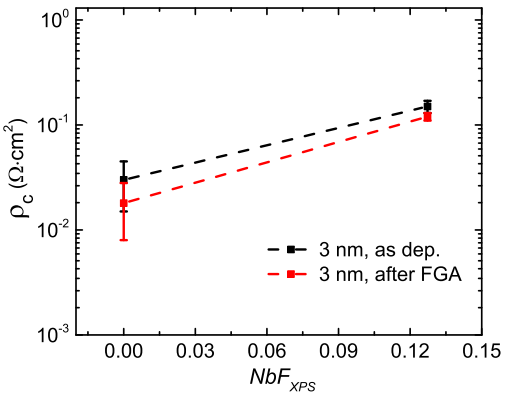

Figure 6.17: Contact resistivity of 3 nm thick films as function of doping concentration before and after forming gas anneal at 300 °C. (see Appendix B for the used anneal times) The films are deposited at a temperature of 200 °C.

As already explained in the previous section (Section 6.4), the net established band bending in the c-Si depends on the exact positions of the Fermi-levels in the c-Si and TiO_x:Nb, but also on the on the presence and extent of fixed charge (dipoles) at the interfaces (c-Si/TiO_x:Nb and TiO_x:Nb/Al interface). An increased Nb doping concentration shifts the Fermi-level of TiO_x:Nb upwards; towards the conduction band of TiO_x:Nb. The latter contributes to downward band bending in the in the c-Si. It is thus expected that an increasing doping concentration leads to a more Ohmic contact with a lower contact resistivity. From the previous section (Section 6.4) and from the material study of TiO_x:Nb it has however become clear that thin amorphous TiO_x:Nb films ($\leq$ 5 nm) show completely different electrical properties as thicker crystalline TiO_x:Nb films. The above described hypothesis may only apply for conductive anatase crystalline TiO_x(:Nb) and not for the thin high resistive and amorphous TiO_x:Nb films ($\leq$ 5 nm) used for this contact resistivity study. When Nb atoms are not or less active as dopants, the presence of the NbO_x interlayers may only influence the interface dipoles [82] or material properties of the TiO_x:Nb layer. Differences in for example the capacitance of the TiO_x:Nb layer can decrease the beneficial influence of the low Al work function on the band bending in the c-Si(n) (see Section 5.6.3), which could lead to the observed stronger rectifying behavior (Figure 6.18) and the higher ρ_c.

With regard to the very high carrier concentration obtained for 30 nm films, it would be interesting to investigated the contact resistivity of these thicker films, since they may behave quite

differently from the thin films investigated here. Also the crystallization of thinner TiO_x:Nb is an interesting topic for future work.

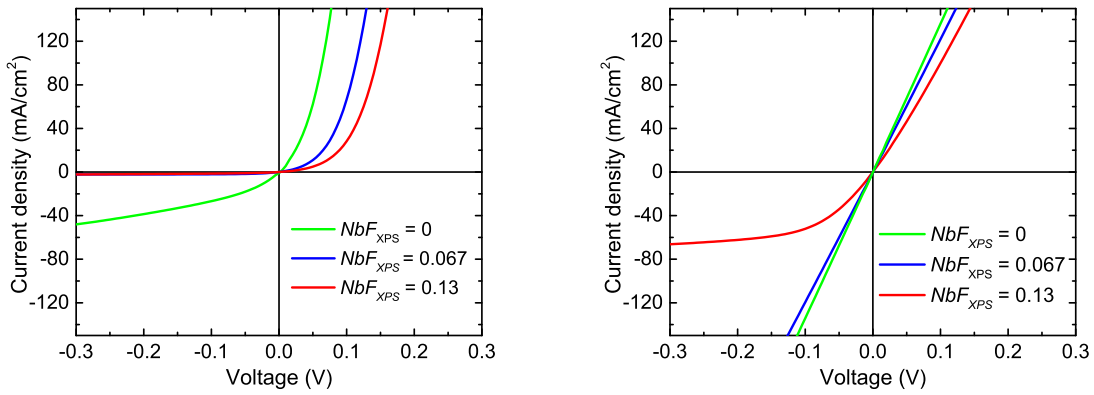

Figure 6.18: J-V characteristics plotted for different doping concentrations (NbF_{XPS}) of 5 nm thick TiO_x:Nb films in the as-deposited state (a) and after FGA (b) (see Appendix B for anneal times).

6.6 Conclusions and recommendations

The aim of this work was to develop and investigate TiO_x:Nb as a tunable electron-selective passivating contact material. The most important findings are summarized in this section accompanied by suggestions for future work.

TiO_x:Nb films have been successfully been deposited with the help of a newly developed ALD doping recipe. The deposited TiO_x:Nb films have a thickness of 30 nm and are found to be nearly stoichiometric (O/(Nb+Ti) = 1.9 ± 0.1) with a very low impurity content ($\leq$ 2 at. %). In the as-deposited state, the films are amorphous with a resistivity of about $\rho \approx 3$ Ω·cm. The resistivity of the TiO_x:Nb is greatly reduced by a post-deposition forming gas anneal at 300 °C. Resistivity values as low as $9{\cdot}10^{-3}$ Ω·cm have been obtained, which are similar to the values reported by others on ALD TiO_x:Nb [73], [74]. The decrease in resistivity upon annealing is attributed to the crystallization of TiO_x:Nb to anatase phase, a crystal phase well known for its conductive properties. By increasing the Nb-fraction from $NbF_{XPS} = 0$ to $NbF_{XPS} = 0.067$, a change in resistivity (ρ) and electron concentration (n_e) of $\rho \approx 1{\cdot}10^{-1}$ to $9{\cdot}10^{-3}$ Ω·cm and $n_e = 9{\cdot}10^{19}$ to $1.0{\cdot}10^{21}$ cm^{-3} is achieved, respectively. Both thinner (1-5 nm) TiO_x:Nb and TiO_x films, and the 30 nm film with the highest Nb-fraction of $NbF_{XPS} = 0.13$ showed no crystallization upon annealing at 300 °C. While the amorphous 30 nm film still exhibited a resistivity between 4.4 and 825 Ω·cm, the resistivity of the thin amorphous films was too high to be measured.

The observation that all 1-5 nm TiO_x:Nb films are amorphous and very resistive relates probably to the observation that the c-Si(n) surface passivation provided by 3 to 5 nm thick films TiO_x:Nb is nearly unaffected by the Nb doping concentration ($S_{eff,max}$ = 11.6 - 21.9 cm/s for undoped TiO_x and $S_{eff,max}$ = 12 - 26.3 cm/s for doped TiO_x with $NbF_{XPS} = 0.13$). The contact resistivity of a c-Si/TiO_x:Nb/Al contact configuration featuring 1-5 nm TiO_x:Nb has shown to increase substantially with doping concentration (from $\rho_c = 0.035$ Ω·cm^2 for $NbF_{XPS} = 0$ to $\rho_c = 2.3$ Ω·cm^2 for $NbF_{XPS} = 0.13$). The reason for this behavior is not yet clear, but since the Nb-doping did not yield a reduction in electrical conductivity, the presence of the NbO_x interlayers may only increase the screening of the Al metal work function, leading to this higher contact resistivity with doping concentration.

For future work, thicker crystalline TiO_x:Nb films are worth further investigation since the high electron concentration that is observed for these films is expected to give rise to downward band bending in the c-Si, which could lead to an enhanced field-effect passivation, lower contact resistivity and enhanced electron selectivity. Although Liao et al. [17] report deterioration of passivation upon crystallization of TiO_x, these detrimental effects could be overcome by applying similar strategies as for crystalline ZnO:Al applying a interfacial SiO_x layer prior to ALD, and a sacrificial capping layer of ALD aluminum oxide [34]. A second route to exploit the benefits of Nb doping is to attempt crystallizing thinner (1-5 nm) TiO_x:Nb films by using higher anneal temperatures. When this option proves to be possible, it may be preferred over thicker TiO_x:Nb films with regard to industrial feasibility.

Chapter 7

General conclusions and recommendations

In this work the important factors and mechanisms for the c-Si surface passivation and contact resistivity have been investigated for ALD TiO_x. Furthermore, an ALD recipe for TiO_x:Nb was developed to explore TiO_x:Nb as new tunable electron-selective passivating contact material.

It is found that important factors for the passivation of a few nanometer ALD TiO_x include a post-deposition forming gas anneal , the c-Si surface treatment prior to ALD, and, mainly for HF-cleaned c-Si, the ALD temperature. The c-Si surface passivation mechanisms of TiO_x turns out to be a combination of chemical passivation and field-effect passivation. The latter is originating from a large induced upward band bending in the c-Si and is rather independent from the above mentioned factors. From these findings it was concluded that differences in the c-Si passivation of TiO_x are mainly due to differences in chemical passivation, which can be strongly improved by choosing the right c-Si surface treatment and applying a post-deposition forming gas anneal.

Factors that are important for the contact resistivity of a c-Si/TiO_x/Al contact configuration include the TiO_x film thickness, ALD temperature and a post-deposition forming gas anneal. Rectifying I-V behavior of the contact structure is a very important reason for a high contact resistivity. A post-deposition forming gas anneal is the key for transforming this rectifying I-V behavior to low Ohmic behavior. While the physics of these contact structures is very complicated, an attempt have been made to explain some of the experimental observations, with one of the outcomes being that the origin of the rectifying behavior is upward band bending in the c-Si(n).

For a low Ohmic electron-selective contact, a downward band bending in the c-Si is required. This work shows that the c-Si surface passivation by TiO_x has an important field-effect component that is not established by downward, but upward band bending in the c-Si. From this work it has therefore become clear that an electron contact with good c-Si surface passivation and low ρ_c featuring TiO_x is not necessarily evident. For future work it is important to investigate this c-Si band bending by TiO_x and try to establish substantial downward band bending in the c-Si by either tailoring the TiO_x properties and interfaces or by using a (very) low work function material in combination with TiO_x.

For the exploration of TiO_x:Nb as new tunable electron-selective passivating contact material, a new ALD doping recipe is developed that is capable of depositing high purity TiO_x:Nb films. After crystallization of the films to anatase phase by a post-deposition anneal, very lowly resistive

films are obtained with an electrical conductivity and electron concentration that can be tuned over a large range. In contrast to the crystalline nature and high conductivity of 30 nm thick TiO_x:Nb films, thin TiO_x:Nb films (1-5 nm) keep their amorphous character upon annealing and exhibited a resistivity that is too high to be obtained with 4-point probe measurements. Consequently, prelimary results of the passivation and contact resistivity of these 1-5 nm films show no effect of Nb-doping on the c-Si surface passivation, while the contact resistivity of a c-Si/TiO_x:Nb/Al contact configuration increases with doping concentration. With regard to the promising material properties of the 30 nm thick anatase TiO_x:Nb films, it is interesting to investigate either the passivation and contact resistivity of these thicker crystalline films or to attempt crystallizing thinner films (1-5 nm). With the successful development of TiO_x:Nb an important first step is made, however further research is required to clarify the effect of extrinsic doping of TiO_x on the passivating contact properties.

Chapter 8

Acknowlegdements

I would like to thank all the members of the PMP-group for the nice time I had during my master graduation project. In particular, I would like to thank the following persons for their kind help in my master project:

Prof.dr.ir. W.M.M. (Erwin) Kessels (TUe),
Dr.ir. J (Jimmy) Melskens (TUe),
Dr.ir. B. (Bart) Macco (TUe),
Dr.ir. B.W.H. (Bas) van de Loo (TUe),
Dr.ir. L.E. (Lachlan) Black (TUe),
Ir. S.B. (Saravana) Basuvalingam (TUe) for the niobium oxide ALD recipe,
Dr. M.A. (Marcel) Verheijen (Philips) for the TEM imaging,
Dr. M. (Martin) Bivour (Fraunhofer Institute for Solar Energy Systems) for the SPV measurements

Chapter 9

Bibliography

[1] Sawin, J. L., Seyboth, K., and Sverrisson, F. *Renewables 2016: Global Status Report*. REN21 Secretariat, Paris, (2016).

[2] International Renewable Energy Agency. *Renewable Energy Statistics 2017*. IRENA, Abu Dhabi, (2017).

[3] McCrone, A., Moslener, U., D'Estais, F., and Grünig, C. *Global Trends in Renewable Energy Investment 2017*. Frankfurt School UNEP Collaborating Centre for Climate and Sustainable Energy Finance, (2017).

[4] Energysage. *What are the most efficient solar panels on the market?* available at: http://news.energysage.com/what-are-the-most-efficient-solar-panels-on-the-market/, (2017).

[5] Richter, A., Hermle, M., and Glunz, S. W. *IEEE Journal of Photovoltaics* **3**(4), 1184–1191 (2013).

[6] Wurfel, P. *Physics of Solar Cells, From Principles to New Concepts*. Wiley, Weinheim, (2005).

[7] Zhao, J., Wang, A., Green, M. A. *Solar Energy Materials and Solar Cells* **65**(1-4), 429–435 (2001).

[8] Reichel, C., Müller, R., Feldmann, F., Richter, A., Hermle, M., and Glunz, S. W. *Journal of Applied Physics* **122**(18) (2017).

[9] Yoshikawa, K., Yoshida, W., Irie, T., Kawasaki, H., Konishi, K., Ishibashi, H., Asatani, T., Adachi, D., Kanematsu, M., Uzu, H., and Yamamoto, K. *Solar Energy Materials and Solar Cells* **173**(April), 37–42 (2017).

[10] Melskens, J., Loo, B. W. H. V. D., Macco, B., Vos, M. F. J., Palmans, J., Smit, S., and Kessels, W. M. M. E. *Accepted for publication in: IEEE Journal of Photovoltaics (DOI:10.1109/JPHOTOV.2018.2797106)* (2018).

[11] Geissbühler, J., Werner, J., Nicolas, S. M. D., Barraud, L., Hessler-wyser, A., Nicolay, S., Tomasi, A., Niesen, B., Wolf, S. D., Ballif, C., Niesen, B., Wolf, S. D., and Ballif, C. *Appl. Phys. Lett.* **107**, 081601 (2015).

[12] Yang, X., Weber, K., Hameiri, Z., and De Wolf, S. *Progress in Photovoltaics: Research and Applications* **25**(11), 896–904 (2017).

[13] Vandalon, V. *Sum-frequency generation study of surface chemistry during atomic layer deposition*. PhD thesis, Eindhoven University of Technology, (2017).

[14] Knoops, H. C. M., Potts S. E., Bol A. A., Kessels, W. M. M. In *Handbook of Crystal Growth (Second Edition) Thin Films and Epitaxy: Materials, Processes, and Technology*, chapter 27, 1101–1134. Elsevier (2015).

[15] Hoex, B., Schmidt, J., Pohl, P., van de Sanden, M. C. M., and Kessels, W. M. M. *Journal of Applied Physics* **104**(4), 044903 (2008).

[16] Avasthi, S., McClain, W. E., Man, G., Kahn, A., Schwartz, J., and Sturm, J. C. *Applied Physics Letters* **102**(20) (2013).

[17] Liao, B., Hoex, B., Aberle, A. G., Chi, D., and Bhatia, C. S. *Applied Physics Letters* **104**(25), 3–7 (2014).

[18] Yang, X., Bi, Q., Ali, H., Davis, K., Schoenfeld, W. V., and Weber, K. *Advanced Materials* **28**(28), 5891–5897 (2016).

[19] Allen, T. G., Bullock, J., Jeangros, Q., Samundsett, C., Wan, Y., Cui, J., Hessler-Wyser, A., De Wolf, S., Javey, A., and Cuevas, A. *Advanced Energy Materials* **7**(12), 1–7 (2017).

[20] Matsui, T., Bivour, M., Ndione, P., Hettich, P., and Hermle, M. *Energy Procedia* **124**, 628–634 (2017).

[21] Titova, V., Veith-Wolf, B., Startsev, D., and Schmidt, J. *Energy Procedia* **124**, 441–447 (2017).

[22] Dingemans, G., Beyer, W., van de Sanden, M. C. M., Kessels, W. M. M. *Applied Physics Letters* **97**(15), 152106 (2010).

[23] Luth, H. *Solid Surfaces, Interfaces, and Films*. Springer-Verlag Berlin Heidelberg, Heidelberg, (2001).

[24] Zekentes, K., Vassilievski, K. *Patent (US 6599644 B1)* (2003).

[25] Mead, C. In *Ohmic contacts to semiconductors*, 3–16. Electrochem. Soc, New York (1969).

[26] Schroder, D. K., Meier, D. L. *IEEE Transactions on electron devices* **31**(5) (1984).

[27] Volker, H. *Phys. Rev.* **138**(6a), A1689–A1696 (1965).

[28] Gutpa, S., Paramahans Manik, P., Kesh Mishra, R., Nainani, A., Abraham, M.C., and Lodha, S. *Journal of Applied Physics* **113**, 234505 (2013).

[29] Anderson, R. *IBM Journal of Research and Development* **4**(3), 283–287 (1960).

[30] Bersch, E. *Energy level allignment in metal/oxide/semiconductor and organic dye/oxide systems*. Phd thesis, The State University of New Jersey, (2008).

[31] Yang, X., Zheng, P., Bi, Q., and Weber, K. *Solar Energy Materials and Solar Cells* **150**(June), 32–38 (2016).

[32] Plakhotnyuk, M. In *26th International Photovoltaic Science and Engineering Conference*, (2016).

[33] Scheerder, R. *ALD Metal Oxides for Passivating Contacts in c-Si Solar Cells*. Master thesis, Eindhoven University of Technology, (2017).

[34] Van de Loo, B. W. H. *Atomic layer-deposited surface passivation schemes for silicon solar cells*. PhD thesis, Eindhoven University of Technology, (2017).

[35] Holman, M. B., Yang, X., Weber, K., and C., Z. In *2016 IEEE 43rd Photovoltaic Specialists Conference (PVSC)*, 2403–2407, (2016).

[36] Strahm, B., Andrault, Y., Baetzner, D., Guérin, C.., Holmes, N., Kobas, M., Lachenal, D., Mendes, B., Tesfai, M., Wahli, G., Wuensch, F., Buechel, A., Mai, J., Schulze, T., Vogt, M. In *5th World Conf. Photovolt. Energy Conversion Spain*, 1286–1289, (2010).

[37] Methaapanon, R. and Bent, S. F. *The Journal of Physical Chemistry C* **114**(23), 10498–10504 (2010).

[38] Strack, R. C. and H. *Solid-State Electronics* **10**(12), 1213–1214 (1967).

[39] Thomas, A., Zheng, P., Vaughan, B., Barr, M., Wan, Y., Samundsett, C., Bullock, J., Cuevas, A. In *2016 IEEE 43rd Photovoltaic Specialists Conference (PVSC)*, 0230–0233, (2016).

[40] Agrawal, A., Lin, J., Barth, M., White, R., Zheng, B., Chopra, S., Gupta, S., Wang, K., Gelatos, J., Mohney, S. E., and Datta, S. *Applied Physics Letters* **104**(11), 8–12 (2014).

[41] Zakrzewska, K. *Advanced Materials Science* **5**, 972 (2012).

[42] Kern, W. *Journal of the Electrochemical Society* **137**(6), 1887–1892 (1990).

[43] Palmans, J. M., Melskens, J., Karwal, S., Kessels, W. M. M., Creatore, M. *(Insights into ultrathin silicon oxides for passivating contact based crystalline silicon solar cells) Submitted for publication* (2017).

[44] Sinton, R.A., Cuevas, A., Stuckings, M. In *Proceedings of the 25th IEEE Photovoltaic Specialist Conference*, 457–460, (1996).

[45] Rein, S. *Lifetime Spectroscopy A Method of Defect Characterization in Silicon for Photovoltaic Applications*. Springer, Berlin, Heidelberg, (2005).

[46] Fujiwara, H. *Spectroscopic Ellipsometry Principles and Applications*. John Wiley and Sons Ltd, Chichester, (2007).

[47] Unkown Author. *https://www.revolvy.com/main/index.php?s=Ellipsometry\&item_type=topic* (2017).

[48] Woollam Co., J. *CompleteEASE Data Acquisition and Analysis Software for J.A. Woollam Co. Spectroscopic Ellipsometers Software*. Woollam Co., (2014).

[49] Tauc, J. *Materials Research Bulletin* **3**, 37–46 (1968).

[50] Watts, J.H., Wolstenholme, J. *An Introduction to Surface Analysis by XPS and AES*. Wiley and Sons, Chichester, (2003).

[51] Thermo Fisher Scientific. *XPS knowlegde view of the Thermo Advantage software v5.967*. Thermo Fisher Scientific, (2016).

[52] Xie, Q., Jiang, Y.-L., Detavernier, C., Deduytsche, D., Van Meirhaeghe, R. L., Ru, G.-P., Li, B.-Z., and Qu, X.-P. *Journal of Applied Physics* **102**(8), 083521 (2007).

[53] Thamaphat, K., Limsuwan, P., and Ngotawornchai, B. *Nature Science* **42**, 357–361 (2008).

[54] Agatino Di Paola, M. B. and Palmisano, L. *Catalysts* **3**, 36–73 (2013).

[55] Liu, G., Yang, H. G., Sun, C., Cheng, L., Wang, L., Lu, G. Q. M., and Cheng, H.-M. *CrystEngComm* **11**(12), 2677 (2009).

[56] Shard, A. G. *Surface and Interface Analysis* **46**, 175–185 (2014).

[57] Gu, H., Wang, Z., Hu, Y. *Sensors* **12**, 5517–5550 (2012).

[58] A. Rothschild, A. Levakov, Y. Shapira, N. Ashkenasy, Y. K. *Surface Science* , 532–535, 456–460 (2013).

[59] Haidry, A.A.., Schlosser, P., Durina, P., Mikula, M., Tomasek, M., Plecenik, T., Roch, T., Pidik, A., Stefecka, M., Noskovic, J., Zahoran, M., Kus, P., Plecenik, A. *Central European Journal of Physics* **9**(5), 1351–1356 (2011).

[60] Al-Baradi, M. M. A. E.-R. and M., A. *International Journal of Physical Sciences* **8**(31), 1570–1580 (2013).

[61] Zhang, M., Lin, G., Dong, C., Wen, L. *Surface and Coatings Technology* **201**(16-17), 7252–7258 (2007).

[62] Bendavid, A. , Martin, P. J., Takikawa, H. *Thin Solid Films* **360**, 241–249 (2000).

[63] Ottermann, C.R., Bange, K. *Thin Solid Films* **286**, 32–34 (1996).

[64] Kinosita, K., Nishibori, M. *Journal of Vacuum Science and Technology* **6**, 730 (1969).

[65] Schinke, C., Peest, P.C, Schmidt, J., Brendel, R., Bothe, K., Vogt, M.R., Kröger, I., Winter, S., Schirmacher, A., Lim, S. *American Institute of Physics Advances* **5**, 067168 (2015).

[66] König, T. A. F., Ledin, P. A., Kerszulis, J., Mahmoud, M. A., El-Sayed, M. A., Reynolds, J. R., Tsukruk, V. V. *American Chemical Society Nano* **8**, 6182–6192 (2014).

[67] Holman, Z., Descoeudres, A., Barraud, L., Fernandez, F., Seif, J., De Wolf, S., Ballif, C. *IEEE Journal of Photovoltaics* **2**(1), 7–15 (2012).

[68] Santbergen, R. *Optical Absorption Factor of Solar Cells for PVT Systems.* PhD thesis, Eindhoven University of technology, (2008).

[69] Himpsel, F. J., Feely, F. R. Mc., Taleb-Ibrahimi, A., Yarmoff, J. A. *Physical Review B* **38**(9), 6084–6095 (1988).

[70] Cui, J., Allen, T., Wan, Y., Mckeon, J., Samundsett, C., Yan, D., Zhang, X., Cui, Y., Chen, Y., Verlinden, P., and Cuevas, A. *Solar Energy Materials and Solar Cells* **158**, 115–121 (2016).

[71] Tung, R. T. *Applied Physics Reviews* **1**, 011204 (2014).

[72] Wu, Y., Hermkens, P. M., van de Loo, B. W. H., Knoops, H. C. M., Potts, S. E., Verheijen, M. A., Roozeboom, F., and Kessels, W. M. M. *Journal of Applied Physics* **114**(2), 024308 (2013).

[73] Niemelä, J. P., Yamauchi, H., and Karppinen, M. *Thin Solid Films* **551**, 19–22 (2014).

[74] Pore, V., Ritala, M., Leskel, M. *Crystal Growth & Design* **9**, 2974 (2009).

[75] Hitosugi, T., Ueda, A., Nakao, S., Yamada, N., Furubayashi, Y., Hirose, Y., Shimada, T., Hasegawa, T. *Applied Physics Letters* **90**, 212106 (2007).

[76] Yamada, N., Hitosugi, T., Ngoc Lam Huong Hoang, Furubayashi, Y., Hirose, Y., Shimada, T., Hasegawa, T. *Japanese Journal of Applied Physics* **46**, 5275 (2007).

[77] Basuvalingam, S. B. *Thermal ALD recipe for niobium oxide, developed at Eindhoven University of technology.* (2017).

[78] Kužel, R., Nichtová, L., Matěj, Z., and Musil, J. *Thin Solid Films* **519**(5), 1649–1654 (2010).

[79] Tang, H., Prasad, K., Sanjines, R., Schmid, P. E., Levy, F. *Journal of Applied Physics* **75**, 2042 (1994).

[80] Niemelä, J. P., Hirose, Y., Hasegawa, T., and Karppinen, M. *Applied Physics Letters* **106**(4), 1–6 (2015).

[81] Bakri, A. S., Sahdan, M. Z., Adriyanto, F., Raship, N. A., Said, N. D. M., Abdullah, S. A., and Rahim, M. S. In *AIP Conference Proceedings*, volume 1788, 030030, (2017).

[82] Jiao, Y., Hellman, A., Fang, Y., Gao, S., Kall, M. *Science Reports* **5**, 11374 (2015).

Appendix A

Passivation

Table A.1: Used anneal times for TiO_x films as function of TiO_x film thickness for HF-cleaned silicon. The anneal times as presented in this table are found to be the optimal with regard to passivation.

T_{Dep} (°C)	Tickness (nm)	Si pre-treatment -	Anneal time (minutes)
200	1	HF	10
200	2	HF	20
200	3	HF	20
200	4	HF	40
200	5	HF	100

Table A.2: Used anneal times for Nb-doped TiO_x films as function of doping concentration and film thickness. The anneal times as presented in this table are found to be the optimal with regard to passivation.

T_{Dep} (°C)	Tickness (nm)	NbF_{XPS} (a.u.)	Anneal time (minutes)
200	1	0.13	10
200	2	0.13	20
200	3	0.13	20
200	4	0.13	40
200	5	0.13	100
200	5	0.067	100

Table A.3: Used anneal times for TiO_x films as function of ALD deposition temperature and silicon surface pre-treatment (RCA-cleaned, HF-cleaned, NAOS) for 5nm thick TiO_x films. The anneal times as presented in this table are found to be the optimal with regard to passivation.

T_{Dep} (°C)	Tickness (nm)	Si pre-treatment -	Anneal time (minutes)
50	5	HF	13
100	5	HF	40
150	5	HF	40
200	5	HF	100
250	5	HF	120
300	5	HF	160
50	5	RCA	32
100	5	RCA	60
150	5	RCA	60
200	5	RCA	60
250	5	RCA	80
300	5	RCA	100
50	5	NAOS	-
100	5	NAOS	180
150	5	NAOS	180
200	5	NAOS	180
250	5	NAOS	160
300	5	NAOS	100

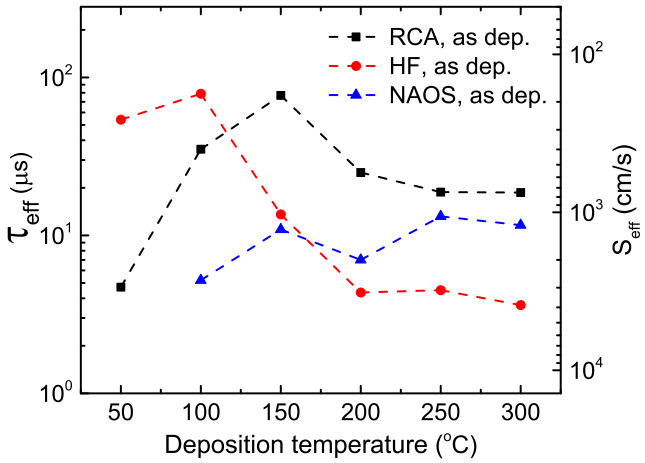

Figure A.1: Best lifetimes obtained for RCA, HF and NAOS pre-treated silicon wafers with 5 nm TiO_x deposited at temperatures ranging from 50°C till 300°C in the as-deposited state. The data point for NAOS at 50°C is not available.

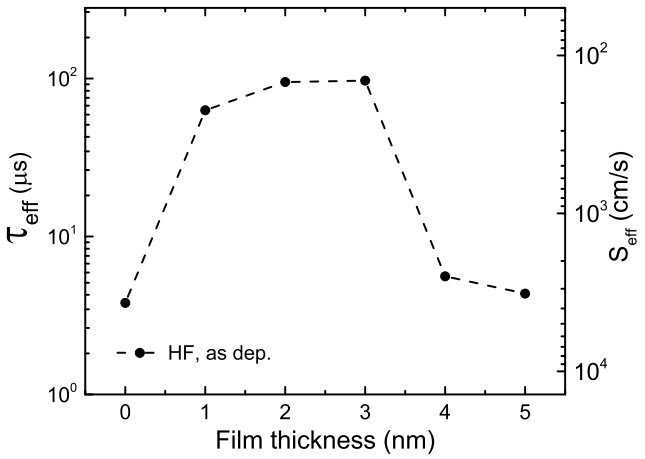

Figure A.2: Effective lifetime as function of the TiO_x film thickness before annealing. A strong temperature dependence is found with a optimum of τ_{eff}= 1.2 ms and $S_{eff,max}$= 11.6 cm/s around 3 nm.

Appendix B

Contact resistivity

Table B.1: Used anneal times for TiO_x films as function of ALD deposition temperature and film thickness. The anneal times as presented in this table are found to be the optimal with regard to passivation.

T_{Dep} (°C)	Tickness (nm)	Anneal time (minutes)
75	5	20
150	5	40
225	5	100
300	5	160
200	1	10
200	2	20
200	3	20
200	4	40
200	5	100

Table B.2: Used anneal times for Nb-doped TiO_x films as function of doping concentration and film thickness. The anneal times as presented in this table are found to be the optimal with regard to passivation.

T_{Dep} (°C)	Tickness (nm)	NbF_{XPS} (a.u.)	Anneal time (minutes)
200	1	0.13	10
200	2	0.13	20
200	3	0.13	20
200	4	0.13	40
200	5	0.13	100
200	5	0.067	100

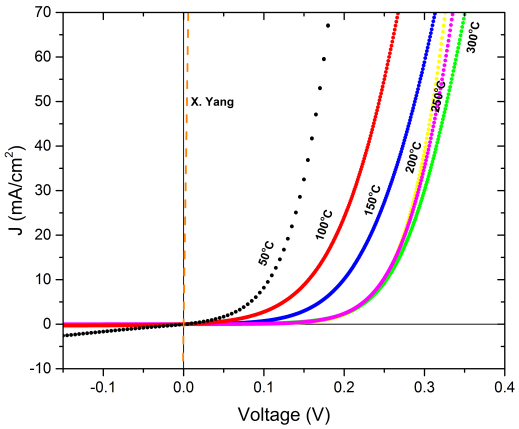

Figure B.1: Rectifying behaviour for contact resistivity samples without stripping the native oxide and by applying the aluminium front contacts with electron beam evaporation. The TiO_x thickness is 5 nm.

Appendix C

XPS

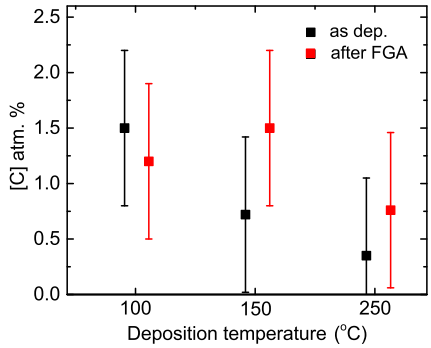

Figure C.1: Calculated arbon content of the TiO_x films before and after 2 hours forming gas anneal at 300°C for various deposition temperatures.

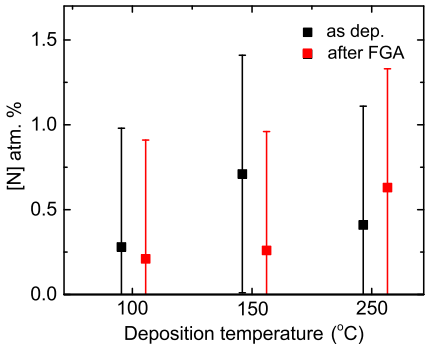

Figure C.2: Calculated nitrogen content of the TiO_x films before and after 2 hours forming gas anneal at 300°C for various deposition temperatures.

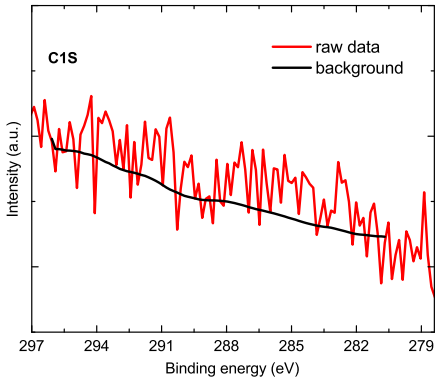

Figure C.3: XPS spectrum of the carbon C1s peak for a 30 nm TiO_x:Nb film deposited at 200°C with $NbF_{XPS} = 0.034$ at in the as-deposited state after 30 seconds of argon sputtering.

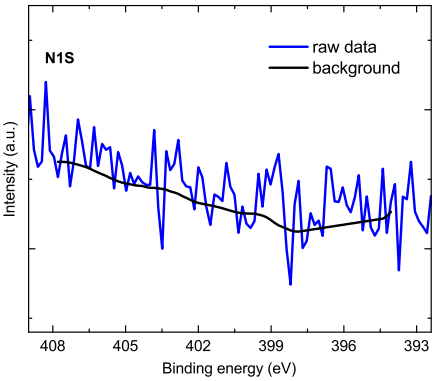

Figure C.4: XPS spectrum of the nitrogen N1s peak for a 30 nm TiO_x:Nb film deposited at 200°C with $NbF_{XPS} = 0.034$ at in the as-deposited state after 30 seconds of argon sputtering.

Appendix D

TEM TiO_x:Nb

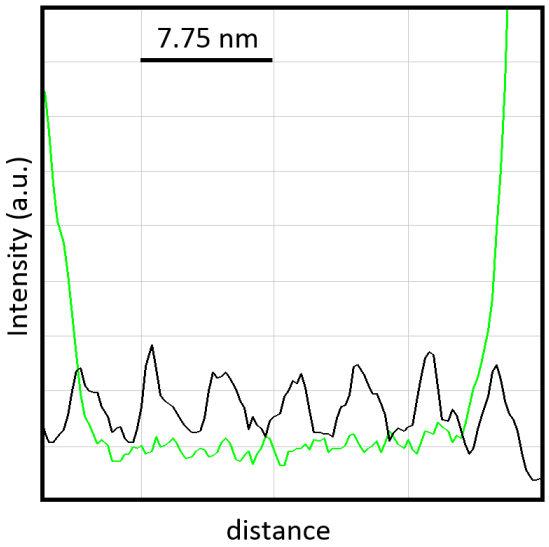

Figure D.1: Nb profile (black line) throughout a ≈30 nm TiO_x:Nb film (indicated by the red box) deposited at 200°C with $NbF_{\mathrm{XPS}} = 0.014$ in as-deposited state. The Nb profile is extracted from Energy-dispersive X-ray spectroscopy. The horizontal axis indicates the position in the 30 nm TiO_x:Nb film, while the vertical axis is a measure for the detected amount atoms. Clear peaks are visible in the black line, indicating the presence of NbO_x interlayers, which are a result of the supercycle fashion of the ALD doping recipe.

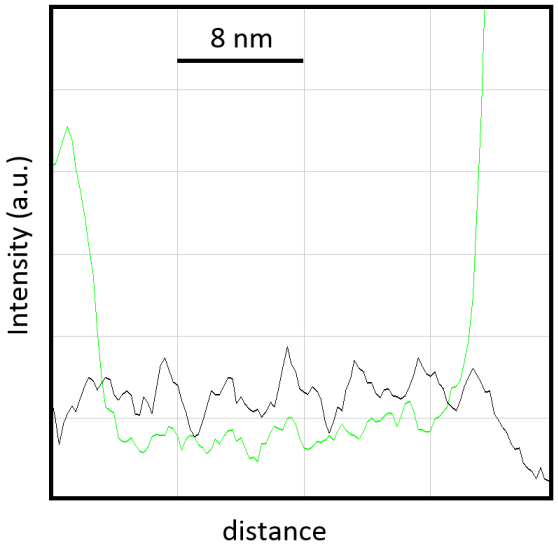

Figure D.2: Nb profile (black line) throughout a ≈30 nm TiO_x:Nb film (indicated by the red box) deposited at 200°C with $NbF_{\mathrm{XPS}} = 0.014$ after 1 hour forming gas annealing at 300°C. The Nb profile is extracted from Energy-dispersive X-ray spectroscopy. The horizontal axis indicates the position in the 30 nm TiO_x:Nb film, while the vertical axis is a measure for the detected amount of atoms. Clear peaks are visible in the black line, indicating the presence of NbO_x interlayers. The Nb peaks seem somewhat less sharp as before annealing, which could indicate more distributed Nb content through the film. According to Dr. M.A. (Marcel) Verheijen (Philips), who did the TEM analysis, this could however also be due to broading of the EDX signal due to a slightly thicker TEM sample. Note also that the intensity can not be compared directly to Figure D.1, since it is not normalized.